CERAMIC PROCESSING AND ELECTROCHEMICAL ANALYSIS OF PROTON CONDUCTIVE SOLID OXIDE FUEL CELL

by

Chih-Long Tsai

A dissertation submitted in partial fulfillment
of the requirements for the degree

of

Doctor of Philosophy

in

Physics

MONTANA STATE UNIVERSITY
Bozeman, Montana

May 2010

APPROVAL

of a dissertation submitted by

Chih-Long Tsai

This dissertation has been read by each member of the dissertation committee and has been found to be satisfactory regarding content, English usage, format, citation, bibliographic style, and consistency and is ready for submission to the Division of Graduate Education.

Dr. V. Hugo Schmidt
Committee Chair

Approved for the Department of Physics

Dr. Richard J. Smith
Department Head

Approved for the Division of Graduate Education

Dr. Carl A. Fox
Vice Provost

STATEMENT OF PERMISSION TO USE

In presenting this dissertation in partial fulfillment of the requirements for a doctoral degree at Montana State University, I agree that the Library shall make it available to borrowers under rules of the Library. I further agree that copying of this dissertation is allowable only for scholarly purposes, consistent with "fair use" as prescribed in the U.S. Copyright Law. Requests for extensive copying or reproduction of this dissertation should be referred to ProQuest Information and Learning, 300 North Zeeb Road, Ann Arbor, Michigan 48106, to whom I have granted "the exclusive right to reproduce and distribute my dissertation in and from microform along with the non-exclusive right to reproduce and distribute my abstract in any format in whole or in part."

Chih-Long Tsai

May, 2010

ACKNOWLEDGEMENTS

This dissertation would not be possible without the help of many individuals. Among them, I would like to express my greatest appreciation to my advisor, Prof. V. Hugo Schmidt, for his support, great patience, encouragement and inspiring discussions so that I could complete this work. It was an enjoyable and precious experience to work with him. I also want to thank Dr. Richard J. Smith for his support and helpful conversations in solving experimental problems. My thanks also go to Dr. Stephen Sofie for providing key equipment and helpful discussions and comments regarding my research. I also want to thank my committee members for their helpful advice in my research direction.

I would like to thank Dr. Alexandre Lussier for assistance in using the SOFC testing system and help in solving problems. Forthermore, I would like to thank members of Dr. Smith's group, Michael Kopczyk, Martin Finsterbusch, Hui Chen, Priyantha Weerasinghe, Kayani Asghar, members of Dr. Sofie's group, Cameron Law, John McCrummen, Adam Weisenstein, Paul Gentile and also my classmates for their invaluable friendship and enrichment of my life.

I would also like to thank Margaret Jarrett, Sarah Barutha, Sherry Heis, Jeannie Gunderson, Jeremy Gay and Norm Williams for taking care of my administrative and technical matters. Finally, I am grateful to my family members for their endless support and love throughout my life.

This work was supported by the United States Department of Energy under Award No. DE-AC06-76RL01830

TABLE OF CONTENTS

TABLE OF CONTENTS – CONTINUED

LIST OF TABLES

LIST OF FIGURES

LIST OF FIGURES – CONTINUED

LIST OF FIGURES – CONTINUED

LIST OF FIGURES – CONTINUED

ABSTRACT

$Ba(Zr_{0.8-x}Ce_xY_{0.2})O_{3-\delta}$ ($0 \leq x \leq 0.4$) (BZCYs) powders were successfully fabricated by both solid state reaction and glycine-nitrate process. Lithium fluoride (LiF) was selected as a liquid phase sintering additive to lower the sintering temperature of BZCYs. Using LiF as an additive, high density BZCYs ceramics can be obtained at sintering temperatures 200~300 ^oC lower than the usual 1700 ^oC with much shorter soaking time. Nuclear reaction investigations showed no lithium and a small amount of fluorine reside in the sample which indicates the non-concomitant evaporation of lithium and fluorine during the sintering process. Scanning electron microscopic investigations showed the bimodal structure of BZCY ceramics and grain growth as Ce content increases. In a water saturated hydrogen containing atmosphere, BZCY ceramics have higher conductivity when LiF is used in the sintering process.

LiF-added BZCY electrolyte-supported fuel cells with different cathodes were tested at temperatures from 500 ~ 850 ^oC. Results show that Pt cathode gives much higher power output than ceramic cathodes, indicating much larger polarization from ceramic cathodes than Pt. $Ba(Zr_{0.6}Ce_{0.2}Y_{0.2})O_{3-\delta}$ anode supported proton conductive solid oxide fuel cells (H-SOFCs) show low power output due to its low proton conductivity. $Ba(Ce_{0.8}Y_{0.2})O_{3-\delta}$ anode supported H-SOFCs show excellent power output. Different H_2 and O_2 partial pressures were used for fuel and oxidative gas, respectively, to obtain information for $V(i)$ modeling.

Different thicknesses of supporting anode were used to obtain saturation current densities of H-SOFC. Using the dusty-gas model which includes Stefan-Maxwell equation and Knudsen terms, the calculation gave tortuosity of our supporting anode 1.95 ± 0.1. The gas concentrations across the anode were also calculated by knowing the tortuosity of the supporting anode.

An electrochemical model of H-SOFC was developed. The excellent agreement between model and experimental data implies that our model is close to the true physical picture of H-SOFC. The more accurate prediction of our model, based on a physical picture of electrochemical processes, also provides a replacement for using the Butler-Volmer equation in SOFC modeling. In the parametric analysis, our model shows that ohmic polarization and cathodic polarization limit the performance of H-SOFC. Research for improving H-SOFC performance should be focused on reducing electrolyte thickness, increasing proton conductivity of electrolyte and finding a compatible cathode material.

CHAPTER 1

INTRODUCTION

The worldwide energy demand is expected to continue growing at an annual rate of 1.8% through 2030 in response to population growth and worldwide industrialization. Nowadays, fossil fuels, which include petroleum, coal and natural gas, supply 86% of the world's energy. However, the fossil fuel reserves are concentrated in a few regions of the world while the demand is worldwide. The Energy Watch Group (EWG) 2007 report shows total world proved plus probable reserves of petroleum to be between 854 and 1,255 G-barrel, which only provides 30 to 40 years of supply even if demand growth were to stop immediately. To minimize the danger of disruption or future large price increases, alternate fuel sources are needed to maintain energy security and prosperity.

Electricity and hydrogen in combination provide a promising route to avoid this danger, because both of them can be made domestically. Furthermore, with the concern about global warming, greenhouse gas emissions can be mitigated by using hydrogen as an alternative energy source. Solid oxide fuel cell (SOFC) systems, which are being developed on various scales, from large centralized power stations to small portable power generation for small electronics, are promising candidates for the next generation energy conversion.

A SOFC is an electrochemical device, which can convert chemical energy directly into electrical energy with an efficiency as high as 60%, much higher than internal combustion engine, which gives 25% efficiency. In addition, SOFC also produces

thermal energy, which can be used for other energy conversion devices to further increase the system efficiency to 75% or for hot water supply and space heating. SOFCs can be made in different sizes without sacrificing efficiency. The high modularity characteristic means it can be placed at different locations with minimum restrictions. Without any moving parts, SOFC also can be placed at urban residential areas.

Compared to oxygen ion conducting SOFC (O-SOFC) for which yttria stabilized zirconia is used for the electrolyte, the development of proton conducting SOFC (H-SOFC) is in its infancy. Theoretical calculations show the benefits of having exhaust gas on the cathode side, which make H-SOFC potentially superior to O-SOFC. Among the high temperature proton conductors, Y-doped barium cerate (BCY) shows the highest proton conductivity but it tends to decompose into protonic insulating barium carbonate ($BaCO_3$) or barium hydroxide ($Ba(OH)_2$) and cerium oxide (CeO_2) when exposed to a CO_2 or high H_2O containing atmosphere [1-5]. In contrast to BCY, Y-doped barium zirconate (BZY) shows high chemical stability but has relatively low proton conductivity due to its high proton resistance at grain boundaries [6-10]. Since a solid solution can be formed easily between barium cerate and barium zirconate, it is possible to find a composition for a compromise between high proton conductivity and high chemical stability. From this point of view, we collaborated with C.-S. Tu *et al.*, to study the stability of Ce-substituted Y-doped barium zirconate (BZCY) [11]. Other than the stability issue, one of the major challenges in BZCY ceramics is that the material is hard to sinter to high density (>93%), which is required for the electrolyte membrane of SOFCs. Usually, extreme temperature (1700 ^{o}C – 1800 ^{o}C), long dwell times (> 20 hours)

and fine powders are required for producing high density ceramic [1,5,12]. Since Li^+ is an easily diffusing ion, and already used for reducing the sintering temperature of $BaTiO_3$ [13], it is possible to reduce the sintering temperature of BZCY by using the same sintering additive.

Presently, considerable effort is being dedicated to the H-SOFC area to find materials with higher proton conductivity and chemical stability. However, electrochemical analysis results for H-SOFC are limited. From the strategic point of view, it is very important to understand how the operating parameters affect the cell performances so that the optimal design of the cell can be made. Along with the modeling, one must calculate carefully the fuel and exhaust gas concentrations at the electrode-electrolyte interfaces. The key parameter in determining the concentration gradient across the electrode is the tortousity τ, which is the ratio of the typical diffusion path length to the electrode thickness. This parameter strongly affects the terminal voltage V as a function of electrolyte current density i and the quality of the anode pore configuration when a supporting anode is used. A careful measurement of tortuosity also provides a more accurate modeling of *V(i).*

1.1 Dissertation Overview

This dissertation begins with this introductory chapter, which gives background of proton conducting oxides, proton transport mechanism, and SOFC. Chapter 2 describes the ceramic fabrication and presents the results of densification studies by introducing lithium fluoride as a sintering aid along with how the sintering additive affects the

conductivity of the ceramics. The fabrication and testing of electrolyte-supported and anode-supported H-SOFCs are reported in Chapter 3. Having the performance of the tested cells, the data provide information for the calculations in the following two chapters.

In Chapter 4, the dusty-gas model, which includes the Stefan-Maxwell equation and Knudsen terms, is used to determine the tortuosity of our supporting anodes. The modeling calculation of H-SOFC is presented in Chapter 5. The theoretical calculation results and experimental data are compared to show the accuracy of our derived model. The model predictions for the effects of operating parameters on H-SOFC are also presented and discussed. A summary of the results presented in this dissertation is given in Chapter 6.

1.2 High Temperature Proton Conducting Oxides

Perovskite-type oxides including rare-earth doped $BaCeO_3$, $BaZrO_3$, $SrCeO_3$ and $SrZrO_3$ were first systematically investigated by Takahashi and Iwahara in 1980 and revealed the proton conductivity of the materials when exposed to H_2 or water containing atmosphere [14,15]. They can be applied to many devices such as hydrogen and hydrogen containing compound sensors, solid oxide fuel cells, hydrogen separation membranes and electrochemical reactors. On exposing the material to hydrogen gas at high temperature, usually higher than 400 ^oC, they become almost pure protonic conductors. The protonic conduction in these oxides was verified by electrochemical hydrogen transport under hydrogen or water vapor containing atmosphere at high

temperatures; for example, the proton transference number of $BaCe_{0.95}Sm_{0.05}O_3$ is ~0.85 at 600 ^oC [16]. Usually, the conductivity of the proton conductive ceramics is in the order of 10^{-2} to 10^{-4} S cm^{-1} at 1000 ~ 600 ^oC. Fig. 1.2.1 shows the proton conductivities of various oxides, which are calculated from available data on proton concentrations and mobilities, for a wide range of temperature.

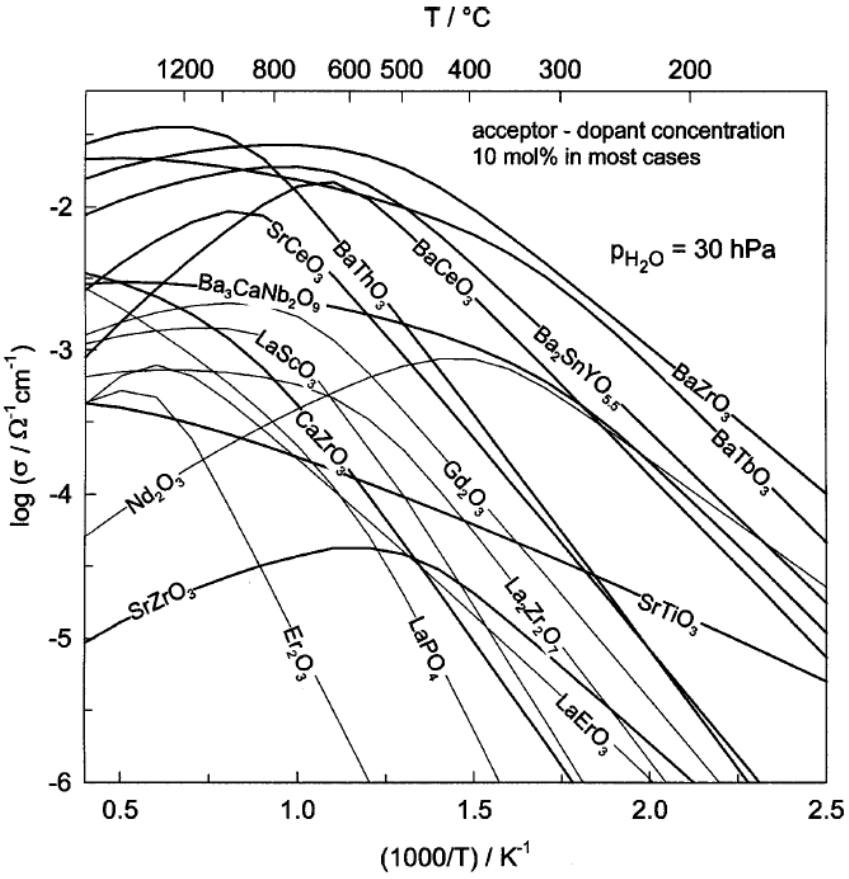

Figure 1.2.1 Calculated proton conductivities based on proton concentrations and mobilities for various oxides. Conductivities of oxides with perovskite-type structure are shown by bold lines [23].

1.2.1 Proton Incorporation

The most important reaction for perovskite ceramics leading to proton uptake is the dissociative absorption of water, which requires the presence of oxygen ion vacancies. Perovskite structure ceramics such as $BaCe_{0.8}Y_{0.2}O_{2.9}$ have been shown to be good protonic conductors [18-22]. The Y^{3+} ions substituting on the perovskite B sites for Ce^{4+} require an O^{2-} ion vacancy for every two Y^{3+} ions to maintain charge neutrality, if there are no protons present. The reaction can be written by Kroger-Vink notation as

$$2Ce_{Ce}^{x} + O_{O}^{x} + Y_2O_3 \rightarrow 2Y'_{Ce} + V_O^{\bullet\bullet} + 2CeO_2. \qquad (1.2.1)$$

From the valence point of view, when Y^{3+} ions replace some Ce^{4+} ions, an oxygen with a Y^{3+} neighbor should welcome one proton to keep the neutrality of the structure. If protons are added by exposure of the ceramic to hydrogen or steam, charge neutrality requires that an O^{2-} ion be added for every two protons added and can be presented as

$$\tfrac{1}{2}H_2 + O_{O}^{x} \rightarrow OH_O^{\bullet} + e', \text{ and} \qquad (1.2.2)$$

$$H_2O_{(g)} + O_{O}^{x} + V_O^{\bullet\bullet} \rightarrow 2OH_O^{\bullet}. \qquad (1.2.3)$$

The loss of oxygen vacancies when protons are added into the structure limits the proton concentration to the same value as the dopant concentration, 0.2 protons per formula unit in $BaCe_{0.8}Y_{0.2}O_{2.9}$, if we assume that oxygen ions can only be added until all oxygen ion vacancies are filled. This limitation of proton concentration not usually exceeding Y^{+3} concentration has been validated experimentally. In particular, Schober and Bohn found maximum proton concentration of 0.083 for $BaZr_{0.9}Y_{0.1}O_{2.95}$, close to the assumed limit

of 0.1[16]. The remaining reduction of the saturation limit from the dopant concentration may be the result from a slight incorporation of the dopant to the A-site where it acts as a donor.

The energy for the incorporation of water into Y-doped $BaCeO_3$ was calculated by Glockner *et al.* using the equation

$$E_{H_2O}=2E_{OH}-E(V_O^{\bullet\bullet})+E_{PT}, \qquad (1.2.4)$$

where E_{OH} is the energy associated with substitution of an O^{2-} ion with an OH^- ion, $E(V_O^{\bullet\bullet})$ is the energy needed to create an oxygen vacancy and E_{PT} is the energy of the gas phase reaction $O^{2-}+H_2O=2OH^-$ [25-27]. It is found that the enthalpy for water incorporation, E_{H_2O}, is exothermic, which indicates Y-doped $BaCeO_3$ is dominated by protons at low temperature and by oxygen vacancies at high temperature. Their results are also consistent with observation that the doped $BaCeO_3$ system is more exothermic than the undoped system when incorporated with water and suggested an energetic stabilization of the protonic defect with doping.

1.2.2 Mobility of Protonic Defects

High diffusivities of protonic defects in the perovskite oxides are a general phenomenon at high temperature. The principle of the transport mechanism involves rotational diffusion of protonic defects and proton transfer between adjacent oxygen ions rather than hydroxyl ion migration. This means only the proton shows long-range diffusion whereas oxygen ions reside on the crystallographic positions for the proton

transport mechanism. Experimentally, this mechanism has been directly proven by Kreuer *et al.* using $BaCeO_3$-based oxides [28]. The ^{18}O-tracer diffusion coefficient is found to be more than 3 orders smaller than what is needed to explain the diffusivity of the protonic defect via hydroxyl ion migration.

The rate-limiting step of the proton transfer mechanism is not clear. Quantum molecular dynamics (QM) simulations and experimental study show the proton transfer reaction in the perovskites is the rate-limiting step because the rotational diffusion has been shown to be fast with low activation barriers [26,29]. However, the infrared spectra indicate the strong hydrogen bond interactions favor faster proton transfer reactions than rotation processes because the rotation process requires the breaking of H-bonds [78].

The distance between oxygen ions in the perovskite oxides is usually larger than 290 pm and strong hydrogen bonds in H-bonded crystal have 250 to 280 pm [26]. Therefore, the gain in free energy of the system due to hydrogen bond formation is competing with the free energy required for the lattice distortion that is required for hydrogen bonding. The QM simulations of cubic perovskites find protons can locally "soften" the lattice. Thus, short oxygen ion separations, which favor proton transfer, and long oxygen ion separations, which allow hydrogen bond breaking, can be achieve. Fig. 1.2.2 shows the instant configurations of one of these protons hopping between neighboring oxygen ions. For the time average, the presence of the protonic defect only leads to a slight reduction of the O-O separation. However, for an instant one of the eight

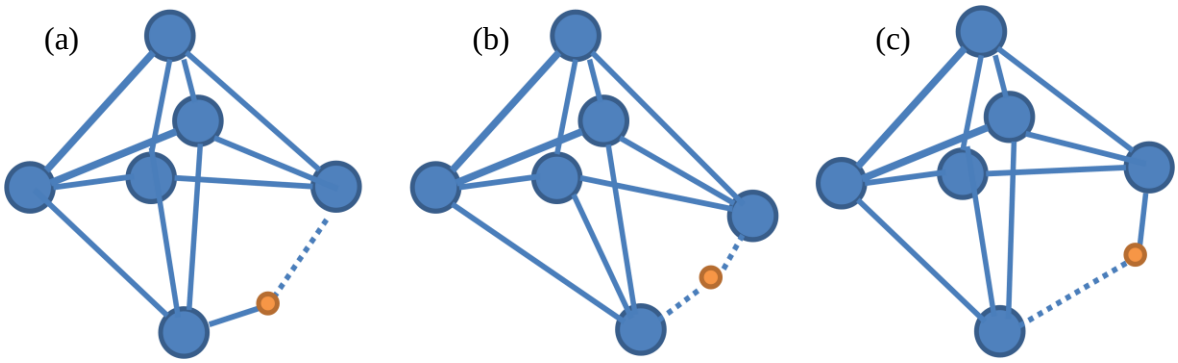

Figure 1.2.2 Instantaneous proton transfer configurations obtained from quantum molecular dynamics (QM) simulations [26].

O-O separations is reduced to about 280 pm for allowing the hydrogen bonding and makes the proton defect behaves almost like a free hydroxyl.

QM simulations also reveal the proton is not found between the two oxygen ions on the edge of the octahedron but outside the BO_6 octahedron as part of a strongly bent hydrogen bond. The reason for this is probably the repulsive interaction between the proton and the B-site cation. The repulsion between proton and B-site cation is also proved by the finding that the activation enthalpies of proton mobility in cubic perovskites with pentavalent B-site cations are significantly higher than for tetravalent B-site cation perovskites.

1.3 Solid Oxide Fuel Cell

1.3.1 Definition of a Fuel Cell

A fuel cell is an electrochemical device consisting of an electrolyte, a porous anode and a porous cathode, which can convert chemical energy directly into electrical energy by performing a chemical reaction. Because the electrolyte is an electronic insulator, electrons from the chemical reaction need to go from anode to cathode by an external circuit, which provides the power to run electronic devices, Fig 1.3.1. In the production of electricity, fuel and oxidative gases flow along the surface of the anode and cathode, respectively, and react electrochemically at triple phase boundaries (TPB) where the electrode, electrolyte and pore meet. Therefore, the consistent generation of electricity can be ensured when fuel and oxidative gases are constantly fed to the porous electrodes. Normally, a single cell produces a voltage around 1.0 V and a series connection between cells is needed for obtaining higher voltage for actual use.

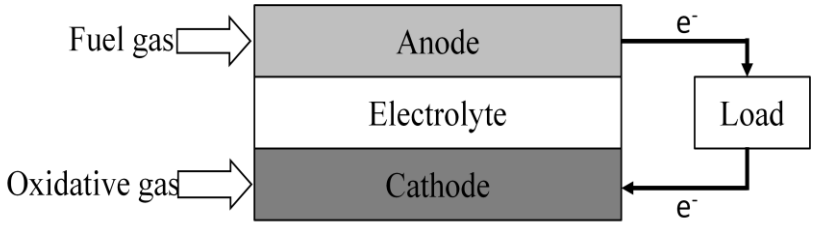

Figure 1.3.1 Schematic representation of a fuel cell.

Many different types of fuel cells have been developed based on this concept. The different fuel cell types are usually classified by the electrolyte that is used, though different classifications based on various parameters such as operating temperature and type of fuel used are also available. Table 1.3.1 lists basic information on different types of fuel cell [31].

Table 1.3.1 Data for different types of fuel cell [31].

Fuel cell type	Mobile ion	Operating temperature	Applications and notes
Alkaline (AFC)	OH^-	50–200°C	Used in space vehicles, e.g. Apollo, Shuttle.
Proton exchange membrane (PEMFC)	H^+	30–100°C	Vehicles and mobile applications, and for lower power CHP systems
Direct methanol (DMFC)	H^+	20–90°C	Suitable for portable electronic systems of low power, running for long times
Phosphoric acid (PAFC)	H^+	~220°C	Large numbers of 200-kW CHP systems in use.
Molten carbonate (MCFC)	CO_3^{2-}	~650°C	Suitable for medium- to large-scale CHP systems, up to MW capacity
Solid oxide (SOFC)	O^{2-}	500–1000°C	Suitable for all sizes of CHP systems, 2 kW to multi-MW.

1.3.2 Historical Perspective of SOFC

The first demonstration of a fuel cell was by Sir William Grove who operated a successful hydrogen-oxygen cell in 1839. He built a cell in which dilute acid solution served as electrolyte, hydrogen as fuel gas and oxygen as oxidative gas to produce electricity and water. The first solid electrolyte was invented by German scientist and Nobel laureate in 1897, Hermann Walther Nernst, who discovered zicronia-based solid oxides have very high electrical resistance and can be used for lighting when electric

current is applied. The most promising oxide mixture is yttria stabilized zirconia (YSZ), which is still the most widely used electrolyte material in the solid oxide fuel cells [32].

The first working SOFC was demonstrated by Baur and Preis at 1937. Zirconia ceramics were used as electrolyte and coke and magnetite as fuel and oxidant, respectively, at 1273 K to achieve the demonstration. In the 1940s, Prof. Davtyan from Russia mixed several carbonates and oxides in order to increase the conductivity, but still experienced low power output, which limited practical application [33]. By the late 1950s, research in solid oxide technology began to accelerate and spread world-wide into several laboratories.

Intense activity in SOFC research began in the 1960s driven by space programs and military applications. The research at that time was focused on improving electrolyte conductivity. A second period of high activity began in the mid-1980s and continues on today, focusing on developing new materials and their technological applications in devices. More recently, with the increasing energy prices and demand, numerous companies, universities and national laboratories are involved in SOFC research [30].

1.3.3 The Solid Oxide Fuel Cell

The Solid Oxide Fuel Cell is a complete solid-state device, which consists of two electrodes, an anode and a cathode, separated by an ionic conductor electrolyte. The cells are usually operated at temperatures between 600 to 1000 ^{o}C, depending on the design of cell configurations. High operating temperature is required for SOFC to increase the ionic conductivity of the electrolyte to generate usable power output. The high operating temperature also gives benefits of no need of precious metals, such as platinum, for

electrocatalyst, and availability of internal hydrocarbon reforming at the anode, which means hydrocarbon fuel such as methane (natural gas), ammonia, coal syngas and propane can be used as fuel directly.

The electrolyte in SOFC mainly determines the cell operating temperature and is used to prevent electronic contact between the two electrodes by blocking the electrons. At the same time, it allows ions to diffuse from one electrode to the other to maintain the overall electrical charge neutrality. Based on the type of diffusing ion, the SOFC can be classified into oxygen ion conducting SOFC (O-SOFC), Fig 1.3.2 (a), and proton conducting SOFC (H-SOFC), Fig. 1.3.2 (b).

For O-SOFC, the most commonly used electrolyte material is YSZ. The advantages of using YSZ include:

i) High strength and toughness, which provide better fracture resistance when serving as electrolyte in SOFC.
ii) High oxygen ion conductivity at temperature higher than 700 ^{o}C, 0.18 S/cm at 1000 ^{o}C and 0.052 S/cm at 800 ^{o}C [34,35].
iii) Exhibits pure oxygen ion conductivity and high chemical stability.
iv) Easy to process sintered material to relative high density, which is required for serving as SOFC electrolyte.

Based on these advantages, YSZ has drawn the most attention from researchers and is the most mature SOFC technology for commercial use.

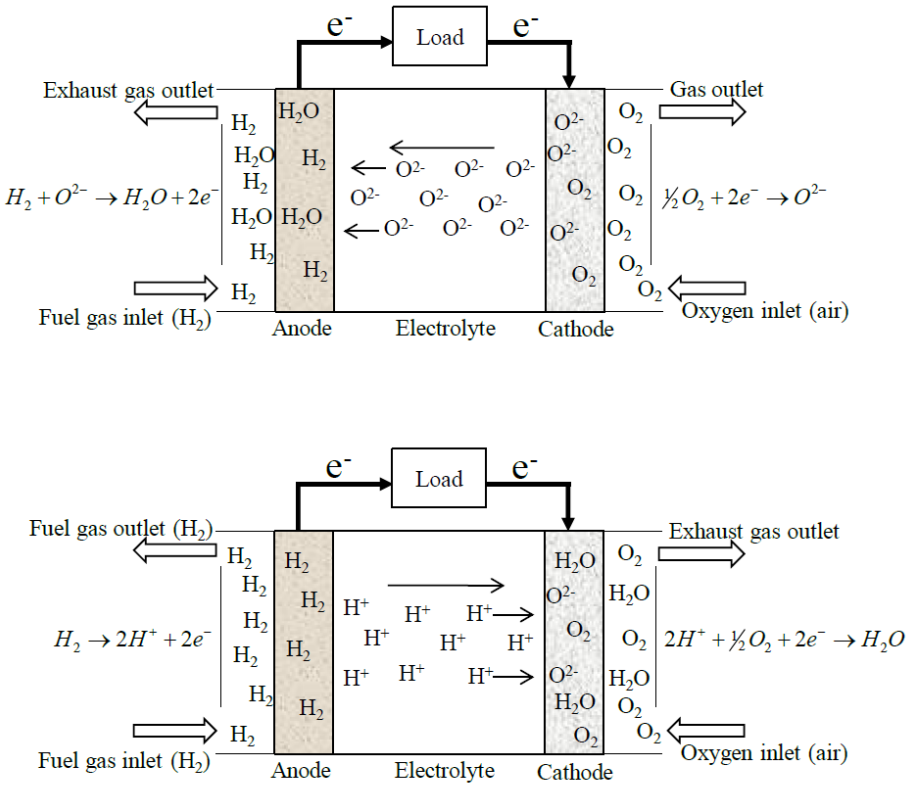

Figure 1.3.2 Diagram of SOFC based on (a) oxygen ion conducting SOFC and (b) proton conducting SOFC.

Proton conductive ceramic was not discovered until the 1960s and the first systematic investigation was done in 1980. Compared to YSZ, which was discovered more than a century ago, there is far less history and research for proton conductive ceramics. Theoretical calculations do show some benefits from using proton conductive ceramics as electrolyte instead of oxygen ion conductive ceramics. The advantages include [36-39]:

i) H-SOFC produces steam at the cathode, which results in no need for a complicated gas separation process at the anode.

ii) Without the steam generation on the anode side, complete fuel utilization is highly plausible.

iii) The Nernst potential of H-SOFC is higher than that of O-SOFC, resulting in higher open-circuit cell potential and higher energy efficiency.

iv) The activation energy of proton conductivity is lower than that of oxygen ion conductivity, which means H-SOFC can be operated at a lower temperature, 500- 700 ^{o}C. This could significantly lower the cost of other parts in the SOFC system and lower the overall price.

The proton conductors discovered to date do not show high proton conductivity and high chemical stability at the same time. A lot of effort is currently focused on increasing proton conductivity and chemical stability of the proton conductive ceramics.

In general, SOFC anodes are fabricated by a mixture of electrolyte material and metal oxide, the metal oxide subsequently being reduced to metal under a reducing atmosphere prior to operation. The mixing of the two materials not only inhibits the sintering of the metal particles but also provides a thermal expansion coefficient more comparable to that of electrolyte material. The anode structure is fabricated with a high porosity, 30% - 50 %, so that gas transportation inside the anode can be done. With respect to the consideration of volatility, chemical stability, catalytic activity and cost, nickel appears to be the best material as a metallic anode [20].

Most recently, research has been directed toward novel ceramic anodes, which are mixed conductors for both electrons and oxygen ions. A further advantage of using a mixed conductor as anode is that it provides a means of extending the TPB at the anode-electrolyte interface. The example materials are Gd-doped ceria mixed with Zr and Y, and various TiO_2-based systems such $SrTiO_3$. However, such materials have much lower electronic conductivity when compared to nickel, which results in high ohmic loss in the cell. Much more effort is still needed in this area.

The same as for the anode, the cathode is a porous structure that allows mass transport of reactant and product gases. Under oxidative atmosphere, the cathode material needs to be both oxygen ionic and electronic conductor and also have high catalytic activity for oxygen molecule dissociation or reduction. The most commonly used material for cathode is $La_{1-x}Sr_xMnO_3$ (LSM), which is a perovskite p-type semiconductor. The transition metal Mn can be substituted by Co and leads to significantly improving the ionic conductivity [20]. However, the doping of Co also leads to higher mismatch of thermal expansion coefficient with electrolyte materials. Some other perovskite materials such as lanthanum strontium ferrite, samarium strontium cobaltite and n-type semiconductors also show good electrocatalysis. Nevertheless, the chemical stability of the material to electrolyte material is an issue.

Due to the early stage of H-SOFC development, the well-studied O-SOFC cathodes have been used for H-SOFC as well. However, the electrode reaction mechanism has not been well understood and the cathodic polarizations are much larger than what is acceptable, about 10 times higher than O-SOFC [40-42]. The remarkable

difference is attributed to the limited electrochemically active reaction sites when an oxygen ion and electron conducting cathode is used as electrode for a proton conducting electrolyte. Therefore, finding a compatible cathode for H-SOFC is a key for H-SOFC development.

CHAPTER 2

LOW TEMPERATURE SINTERING OF $Ba(Zr_{0.8-x}Ce_xY_{0.2})O_{3-\delta}$ USING LITHIUM FLUORIDE ADDITIVE

2.1 Fabrication of Ceramic Powders

$Ba(Zr_{0.8-x}Ce_xY_{0.2})O_{3-\delta}$ (BZCY) powders were synthesized by the Glycine-Nitrate process (GNP) and Solid State Reaction (SSR). For the powders prepared by the glycine-nitrate process, barium nitrate ($Ba(NO_3)_2$, 99.999%), zirconium dinitrate oxide hydrate ($ZrO(NO_3)_2 \cdot xH_2O$, 99.9%), cerium nitrate hexahydrate ($Ce(NO_3)_3 \cdot 6H_2O$, 99.5%) and yttrium nitrate hexahydrate ($Y(NO_3)_3 \cdot 6H_2O$, 99.9%) purchased from Alfa Aesar were dissolved in distilled water. Small amount of the solutions were measured and heated to 1000 ^oC to form metal oxides to determine the concentration of the solutions. Stoichiometric amount of solutions were then weighed and mixed. In addition to constituents, 1.8 times the number of Ba moles of glycine were added to and dissolved in the solution. The solutions were heated on a hot plate under stirring until precipitations were seen and then cooked on a stove to get a viscous gel, then auto-ignited to form powders. The powders were collected and calcined at a temperature of 1200 ^oC for 10 hours to remove possible carbon and impurity residues and form well crystallized BZCYs. Figure 2.1.1 shows the foam structure of the bulk powder from GNP.

For the powders prepared from SSR, stoichiometic amounts of barium carbonate ($BaCO_3$, 99.8%), zirconium oxide (ZrO_2, 99.5%), yittrium oxide (Y_2O_3) from Alfa Aesar and cerium oxide (CeO_2, 99.97%) from Inframat Advanced Material were mixed by an

agate auto-grinding machine for two hours. Then, the powders were calcined at 1200 ^{o}C for 15 hours to form the perovskite phase. The auto-grinding and calcining processes were repeated until a single phase of the material was confirmed by X-ray diffraction.

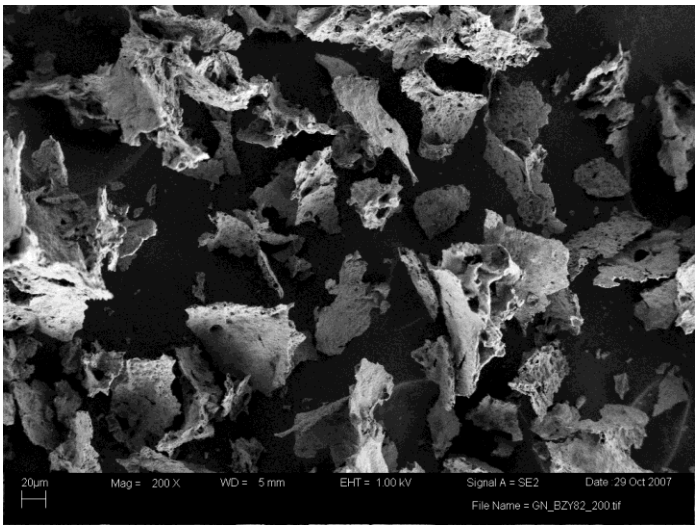

Figure 2.1.1 SEM image of foam structure from $Ba(Zr_{0.8}Y_{0.2})O_{3-\delta}$ powder.

The X-ray diffraction (Scintag, XGEN-400) with Cu Kα (λ=1.5418 $\mathring{A}$) results from calcined $Ba(Zr_{0.8}Y_{0.2})O_{3-\delta}$ powders are shown in Figure 2.1.2 The wider peaks from GNP indicate that the grain sizes were smaller than the powder from SSR. By applying Scherrer's equation, the average grain size of GNP powder was determined to be 21 nm and SSR powder was 35 nm. The particle size measured by TEM from GNP agreed with the calculated result from XRD, Fig. 2.1.3 (b). However, the SEM image, Fig. 2.1.3 (a), shows that the grain size from SSR was about 100 nm, which excludes the

using of Scherrer's equation because for this grain size, other factors determine the XRD linewidth.

The ceramic sintering process occurs by diffusion of atoms through the microstructure. This diffusion is caused by a gradient of chemical potential – atoms move from an area of higher chemical potential to an area of lower chemical potential. This mechanism indicates that pellets with smaller particle size, i.e. higher surface density, will be easier to sinter to higher relative density. Therefore, powders from GNP were chosen for the rest of the research.

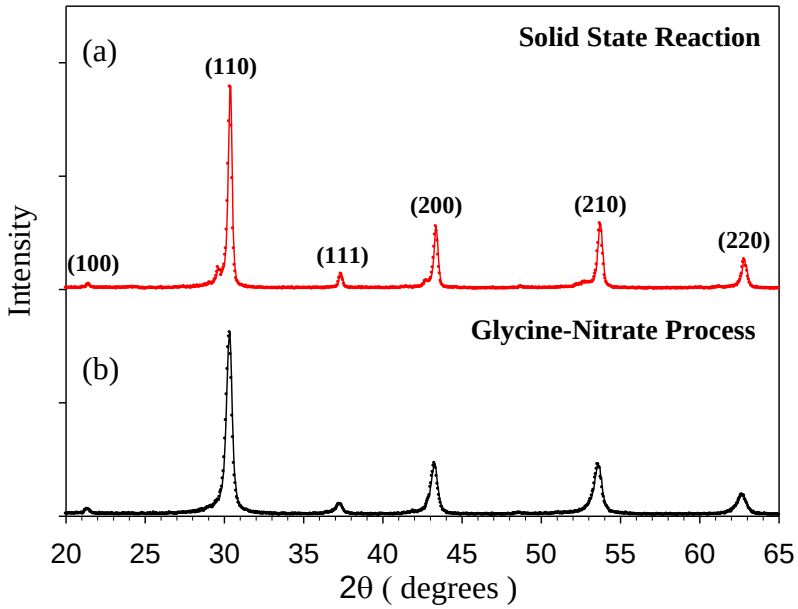

Figure 2.1.2 XRD analysis of $Ba(Zr_{0.8}Y_{0.2})O_{3-\delta}$ powders synthesized by (a) solid state reaction and (b) glycine-nitrate process.

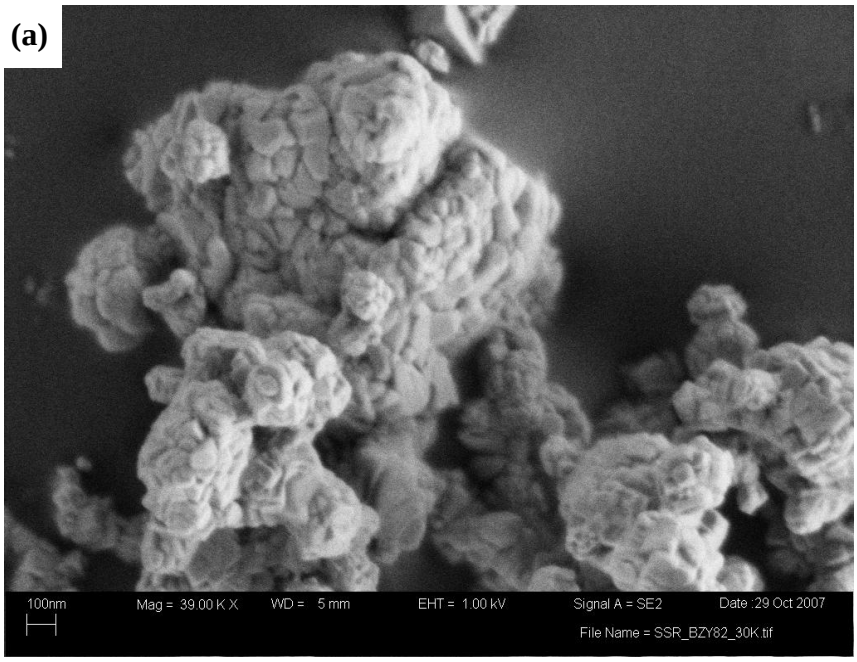

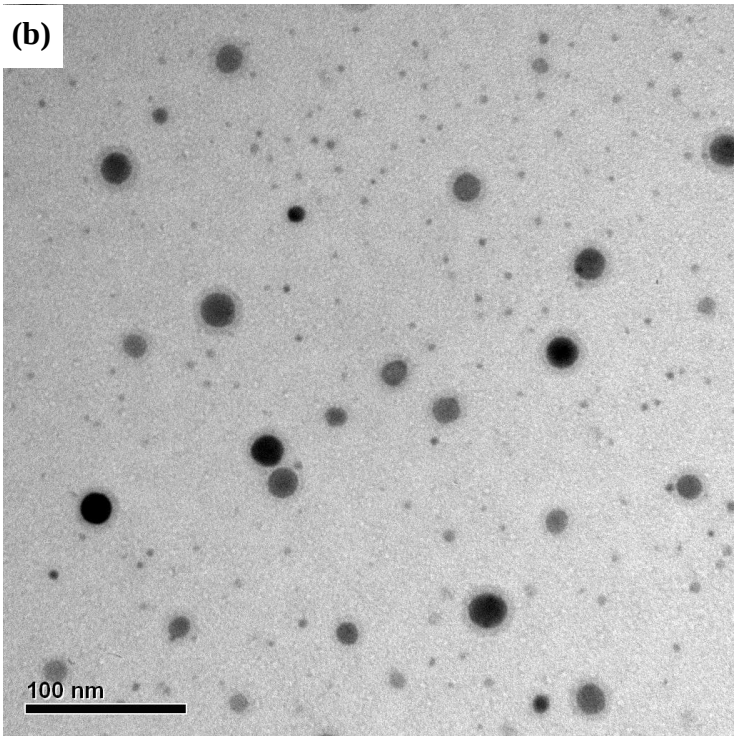

Figure 2.1.3 Microstructural observation of $Ba(Zr_{0.8}Y_{0.2})O_{3-\delta}$ powders synthesized by (a) solid state reaction using SEM and (b) glycine-nitrate process using TEM.

2.2 Ceramic Densification Studies Using Lithium Fluoride Addition

In the ceramic fabrication process, one of the major challenges in BZCY ceramics is that the material is hard to sinter to high density (>93%), which is required for the electrolyte membrane of SOFCs. Usually, extreme temperature (1700 ^{o}C – 1800 ^{o}C), long dwell times (> 20 hours) and fine powders are required for producing high density pellets. Under this extreme condition, not only is economic efficiency low but also is causes barium evaporation, which results in low ionic conductivity [1, 6, 43]. Different methods have been used to approach this problem, which include using wet chemical methods to produce fine powders and using ZnO as a sintering additive to reduce the sintering temperature [7, 44-46]. However, the improvement from using wet chemical methods is limited and the introduction of ZnO results in a Zn evaporation problem at temperature higher than 1300 ^{o}C, which results in dropping more than 20% of relative density when sintering temperature is higher than 1300 ^{o}C. This Zn evaporation problem is serious when a long working time at high temperature is needed for the device. Moreover, Zn can actually replace the element at the B-site and change the microstructure, which results in lowering the ionic conductivity.

Li^{+} is an easily diffusing ion at low temperature, which makes it a very efficient sintering additive for many perovskite materials. The addition of lithium in a form such as lithium fluoride (LiF), has been used to sinter $BaTiO_3$ and $CaZrO_3$ at a temperature 250-300 ^{o}C lower than that necessary for pure material densification [47-49]. The aim of the work described in this chapter was to study the densification process of

$Ba(Zr_{0.8-x}Ce_xY_{0.2})O_{3-\delta}$ $(0 \leq x \leq 0.4)$ ceramics by introducing lithium fluoride and to study the corresponding microstructures.

2.2.1 Experimental Procedures

Densification Studies Densification studies were performed by measuring linear shrinkage from dilatometry and direct measurements of density that were made from the sintered samples. Dilatometric measurements were carried out in static lab air using a Linseis Dilatometer L75. All of the measurements were made with 3 ^{o}C/min heating rate from room temperature to 1500 ^{o}C. Sintering studies were done at temperatures between 1100 ^{o}C and 1500 ^{o}C with different dwell times in a static air atmosphere. To prevent Ba evaporation at high temperature, samples were covered by the same powder during the sintering process. Densities of sintered samples were measured by the Archimedes method using pure ethanol as the immersion medium.

LiF Detection A series of $Ba(Zr_{0.6}Ce_{0.2}Y_{0.2})O_{3-\delta}$ /LiF samples sintered at 1400 ^{o}C, using 5 K/min heating and 10 K/min cooling, with different dwell times was used in this investigation. After polishing one side of the samples to the midplane of their original thickness, a 2 MeV van de Graaff linear accelerator capable of producing a proton beam current of up to one microampere was used to carry out a nuclear reaction process. A silicon surface barrier detector was placed at an angle of 150^{o} relative to the incident particle beam path and used to detect alpha particles resulting from the nuclear reactions:

$$^{7}Li + p \rightarrow {}^{4}He + \alpha \quad \text{and} \tag{2.2.1}$$

$$^{19}F + p \rightarrow {}^{16}O + \alpha\,. \tag{2.2.2}$$

SIMNRA software by Matej Mayer was then used to simulate the experimental data and integrate the alpha particle spectra peaks to determine the amount of lithium and fluorine residing in the samples.

Microstructure Studies The microstructures of sintered samples were investigated by Field Emission Scanning Electron Microscopy (SUPRA^{TM} 55 Versatile High Performance FESEM, Zeiss). Before the study, the samples for investigation were polished by diamond sandpaper to remove any possible impurities on the surface. Thermal etching was then applied in order to see the grain interiors and grain boundaries.

2.2.2 Results and Discussion

Figure 2.2.1 shows the XRD patterns of BZCYs/LiF ceramics, which were sintered at 1400 ^{o}C for 5 hours. All samples displayed a single phase without any LiF-related product peak. The XRD spectra shift to lower angle with increasing Ce concentration, which results from the substitution of the larger Ce^{+4} (0.87 Å) for the smaller Zr^{+4} (0.72 Å) ions at the B-site. The pseudo-cubic lattice parameters calculated from the XRD spectra are shown in Fig. 2.2.2. The linearly increasing lattice parameter indicates that Ce atoms are homogeneously distributed inside the barium zirconate structure and reveals the good stoichiometry of the samples.

The differences in sintering behavior between BZCYs/LiF and BZCYs are shown in Figure 2.2.3. Dilatometric results show that BZCYs/LiF started their densification

process at ~600 ^{o}C while samples without LiF started at ~1000 ^{o}C. The sintering behaviors of BZCYs/LiF accelerated right after 600 ^{o}C and reached the fastest sintering rate in the whole process between 700 ^{o}C and 1000 ^{o}C. This high shrinkage rate is correlated to the melting of LiF at 848 ^{o}C, about the central point between 700 ^{o}C and 1000 ^{o}C. After 1000 ^{o}C, the shrinking process slowed down, whereas the BZCYs shrinkage mechanism was introduced at this temperature, as seen in BZCYs' sintering

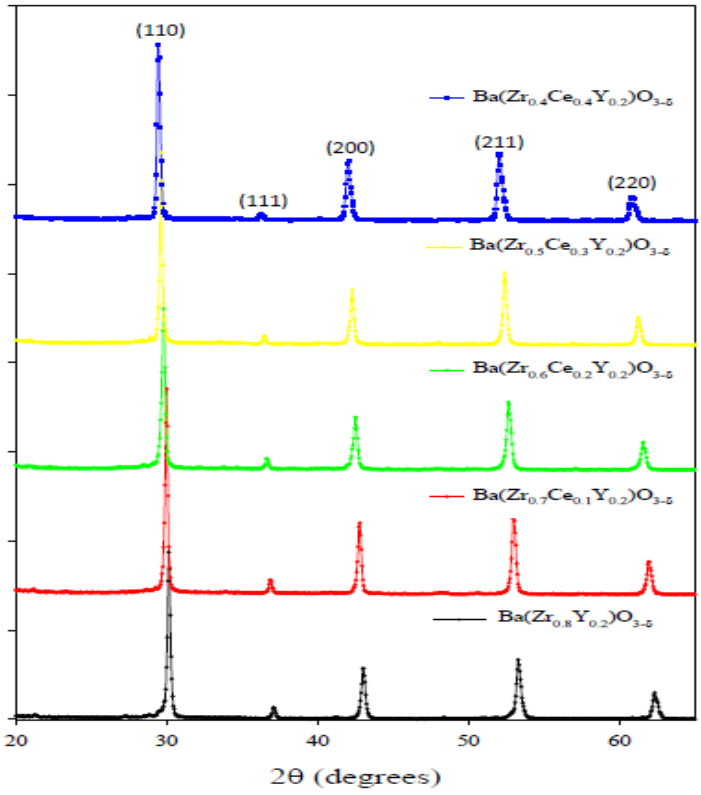

Figure 2.2.1 X-ray diffraction patterns of BZCYs/LiF ceramics which were sintered at 1400 ^{o}C for 5 hours.

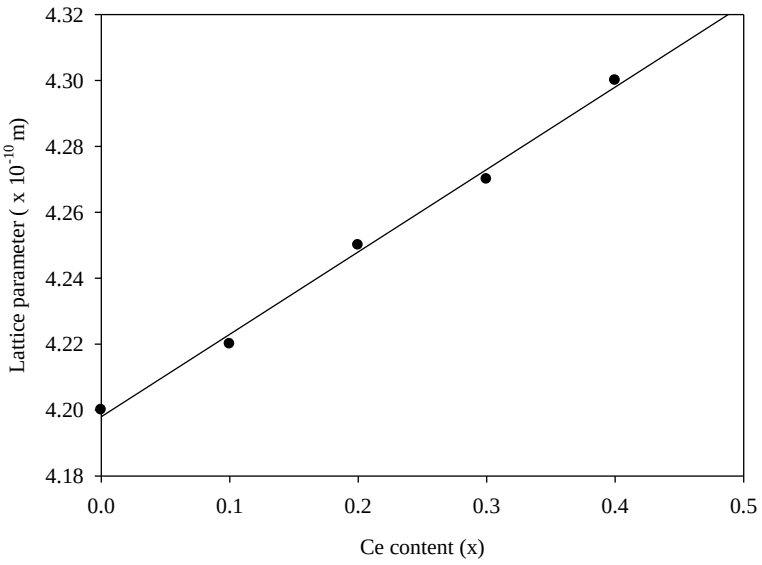

Fig 2.2.2 Pseudo-cubic lattice parameters of BZCYs/LiF calculated from XRD.

behavior. The total shrinkage of BZCYs/LiF samples was between ~15% to ~20%, depending on the composition, which is about four times that of the BZCYs samples. If it is assumed that all the LiF evaporated out of the samples during the sintering process, the contribution from LiF evaporation to the shrinkage is about ~5%. After subtracting this factor due to the presence of LiF, the results still give two to three times higher shrinkage in samples with LiF than in those without LiF.

A further observation in the sintering study was made on a series of samples sintered in a kiln furnace between 1100 ^{o}C and 1500 ^{o}C. It was found that dense ceramics (> 90%) only result from a sintering temperatures higher than 1200 ^{o}C; 1100 ^{o}C only giving results of ~70% density. Comparing samples with and without LiF addition sintered at 1400 ^{o}C for 5 hours, BZCYs/LiF samples were from ~91% to ~96%

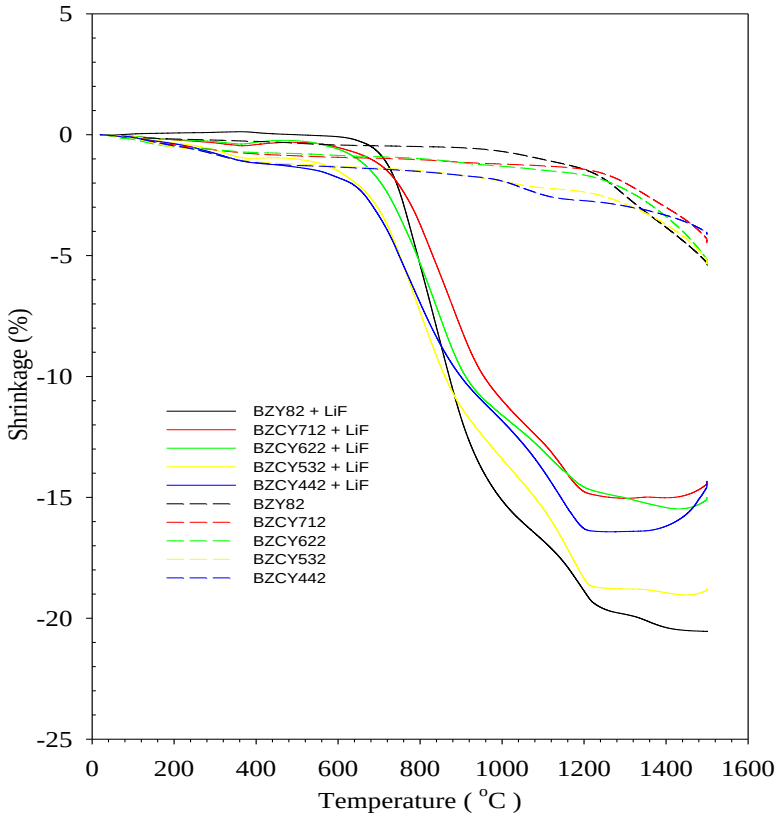

Figure 2.2.3 Temperature dependence of linear shrinkage in BZCYs/LiF and BZCYs.

of the theoretical density, depending on the material, while BZCYs were from ~61% to ~70% dense. Moreover, the appearance and the mechanical properties of the materials are very different when comparing BZCYs/LiF and BZCYs pellets. Comparing the mechanical properties of BZCYs/LiF and BZCYs at similar densities, from different sintering temperatures, pellets with the LiF sintering additive are much tougher than samples without LiF. A hardness test carried out by the Leco microhardness testing system showed that a $Ba(Zr_{0.8}Y_{0.2})O_{3-\delta}$/LiF pellet, sintered at 1400 ^{o}C for 5 hours, had hardness 716.7 HV_{300} and $Ba(Zr_{0.8}Y_{0.2})O_{3-\delta}$, sintered at 1500 ^{o}C for 10 hours, had

hardness 166.0 HV_{300}. The brittleness property of the Y-doped $BaZrO_3$ sample had been reported by many different groups and is a drawback for service as an electrolyte for SOFCs [6,23]. The results of hardness tests show this problem can be alleviated considerably by introducing LiF in the sintering process. Another difference is that BZCYs disintegrated into small pieces upon exposure to air for a couple of days but BZCYs/LiF stay intact even over a long time of exposure to air. This unique property is also evident in our LiF-added $BaCe_{0.8}Y_{0.2}O_{3-\delta}$ (BCY82/LiF) pellets for electrolyte supported fuel cells. The BCY82/LiF, ~300 μm thickness, can keep its glossy polished surface after sitting on a desk for more than a year. $BaCeO_3$-based oxides had been reported highly reactive to CO_2 and H_2O in the air, which makes it disintegrate easily

Table 2.2.1 Porosities and the maximum relative densities achieved from densification studies of (a) BZCYs with LiF sintering additive and (b) BZCYs.

(a) Sample (LiF addition)	Sintering Temperature (°C)	Dwell Time (hours)	Theoretical Density (g/cm^3)	Open Porosity (%)	Closed Porosity (%)	Relative Density (%)
BZY82	1400	5	6.26	1.54	5.83	92.63
BZCY712	1500	8	6.37	1.89	6.92	91.19
BZCY622	1400	5	6.48	0.62	6.29	93.09
BZCY532	1400	5	6.60	1.19	3.96	94.85
BZCY442	1400	5	6.71	0.34	3.66	96.00

(b) sample	Sintering Temperature (°C)	Dwell Time (hours)	Theoretical Density (g/cm^3)	Open Porosity (%)	Closed Porosity (%)	Relative Density (%)
BZY82	1500	8	6.26	11.53	3.59	84..88
BZCY712	1500	20	6.37	4.33	4.52	91.15
BZCY622	1500	20	6.48	1.63	5.06	93.30
BZCY532	1500	20	6.60	3.78	7.19	89.03
BZCY442	1500	20	6.71	7.20	6.40	86.39

*Theoretical density calculated from XRD results using pseudo-cubic structure and $Ba(Zr_{1-x}Ce_xY_{0.2})O_{2.9}$ as atomic weight formula.

upon exposure to air [3,4]. The maximum relative densities that were achieved in the density studies are reported in Table 2.2.1.

Figure 2.2.4 shows the Nuclear Reaction Analysis (NRA) results from a series of LiF-added $Ba(Zr_{0.6}Ce_{0.2}Y_{0.2})O_{3-\delta}$ samples, which were sintered at 1400 ^{o}C with different dwell times. For the as-prepared sample, the two major peaks for lithium and fluorine were identified by the SIMNRA simulation program, Fig. 2.2.4(a). After the heat treatment, even without a dwell time at 1400 ^{o}C, only a small amount of fluorine was detected by NRA but no lithium was detected in any sintered sample, Fig. 2.2.4(b). The results reveal that all the lithium and most of the fluorine evaporated out of the samples during the heating process. Fluorine then continued to leave the samples at a much slower rate at the dwell temperature of 1400 ^{o}C. The detection of only fluorine also shows the non-concomitant departure of lithium and fluorine from

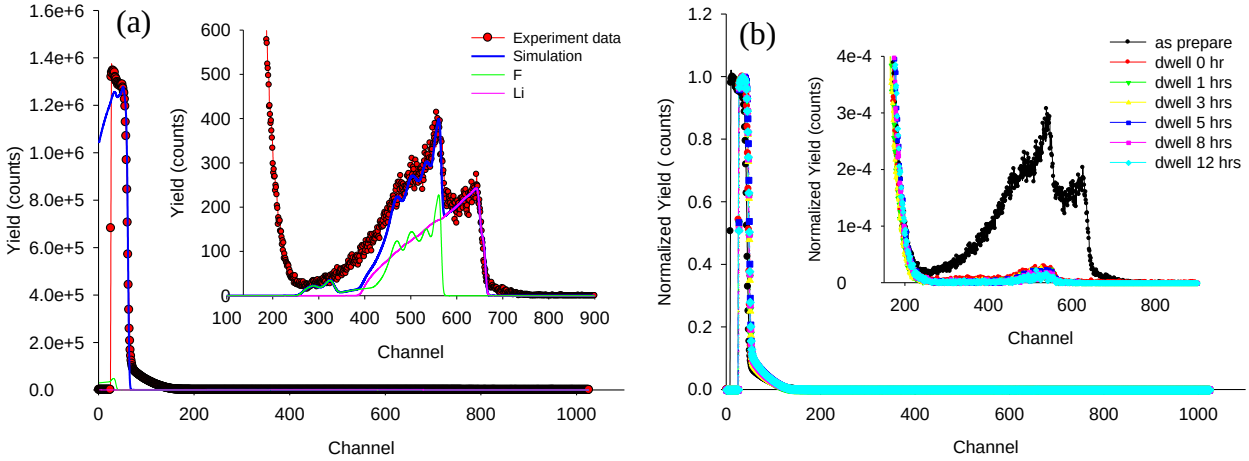

Figure 2.2.4 Nuclear reaction results of (a) as prepared BZCY622/LiF and SIMNRA simulation of the data and (b) BZCY622/LiF sintered at 1400 ^{o}C with dwell time from 0 ~ 12 hours.

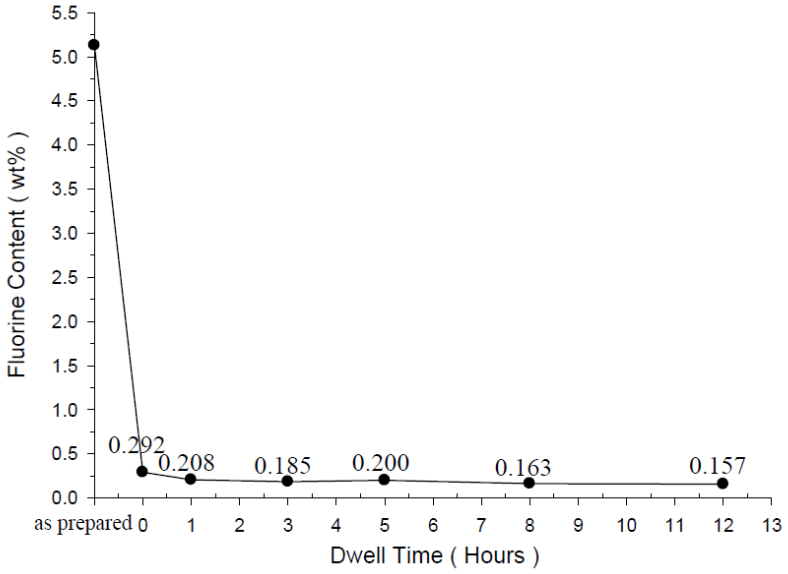

Figure 2.2.5 The amount of fluorine residing inside BZCY622 after different dwell times at 1400 ^{o}C.

$Ba(Zr_{0.6}Ce_{0.2}Y_{0.2})O_{3-\delta}$/LiF samples. By integrating the alpha particle spectrum peaks, the amount of fluorine residing in the samples was calculated and shown in Fig. 2.2.5. Since fluorine cannot exist inside the sample by itself, this means LiF needs to react with some other material and then decompose to fluoride at a higher temperature. Therefore, a small amount of $Ba(Zr_{0.6}Ce_{0.2}Y_{0.2})O_{3-\delta}$ possibly reacted with LiF as shown in equation (2.2.3). As temperature increased, Li_2O evaporated gradually from the $Ba(Zr_{0.6}Ce_{0.2}Y_{0.2})O_{3-\delta}$ sample but kept $(Zr,Ce)Y_{0.2}O_{2-\delta}$ inside the structure, which made the whole $Ba(Zr_{0.6}Ce_{0.2}Y_{0.2})O_{3-\delta}$ sample a barium deficient system. The $BaLiF_3$ melted incongruently near 850 ^{o}C and then decomposed into BaF_2, as seen in Eq. (2.2.4).

$$Ba(Zr_{0.8-x}Ce_xY_{0.2})O_{3-\delta} + 3LiF \rightarrow BaLiF_3 + Li_2O + (Zr,Ce)Y_{0.2}O_{2-\delta} \quad (2.2.3)$$

$$BaLiF_3 \rightarrow BaF_2 + LiF \quad (2.2.4)$$

Combining the results above, the liquid phase mixture between LiF, melt point at 848 ^oC, and $BaLiF_3$, melting point at 857 ^oC, help $Ba(Zr_{0.6}Ce_{0.2}Y_{0.2})O_{3-\delta}$ particles to diffuse leading to densification at a lower temperature than when only $Ba(Zr_{0.6}Ce_{0.2}Y_{0.2})O_{3-\delta}$ is used by itself. This solid to liquid phase transformation and diffusion process also explains the fastest sintering mechanism observed in the dilatometry measurement.

Figure 2.2.6 shows the FE-SEM images of BZCYs/LiF, which were sintered at 1400 ^oC with a 5 hour dwell time. All the pellets showed a dense structure together with bimodal grain sizes after the sintering process. Roughly half of the volume of $Ba(Zr_{0.8}Y_{0.2})O_{3-\delta}$/LiF had micron size grains (1~2 mm) and the other half had smaller grain sizes (~100 nm). This structure is similar to T. Schober's report on $BaZr_{0.9}Y_{0.1}O_{3-\delta}$, which was sintered at 1715 ^oC with a 30 hour dwell time [9]. As the Ce content increases, the structure maintains its bimodal nature, but both large and small grains grew into micrometer sizes. Therefore, the results suggest the grains grow larger with increasing Ce content in the oxide. Along with the microstructure investigation, an Energy-Dispersive X-Ray Spectrometer (EDS) was used to analyze the chemical composition in both the grain and grain boundary to locate the residual fluorine. However, the fluorine peak was not observed in the spectra due to the small quantity of fluorine present. More fluoride may have evaporated from the sample surface during the thermal etching process

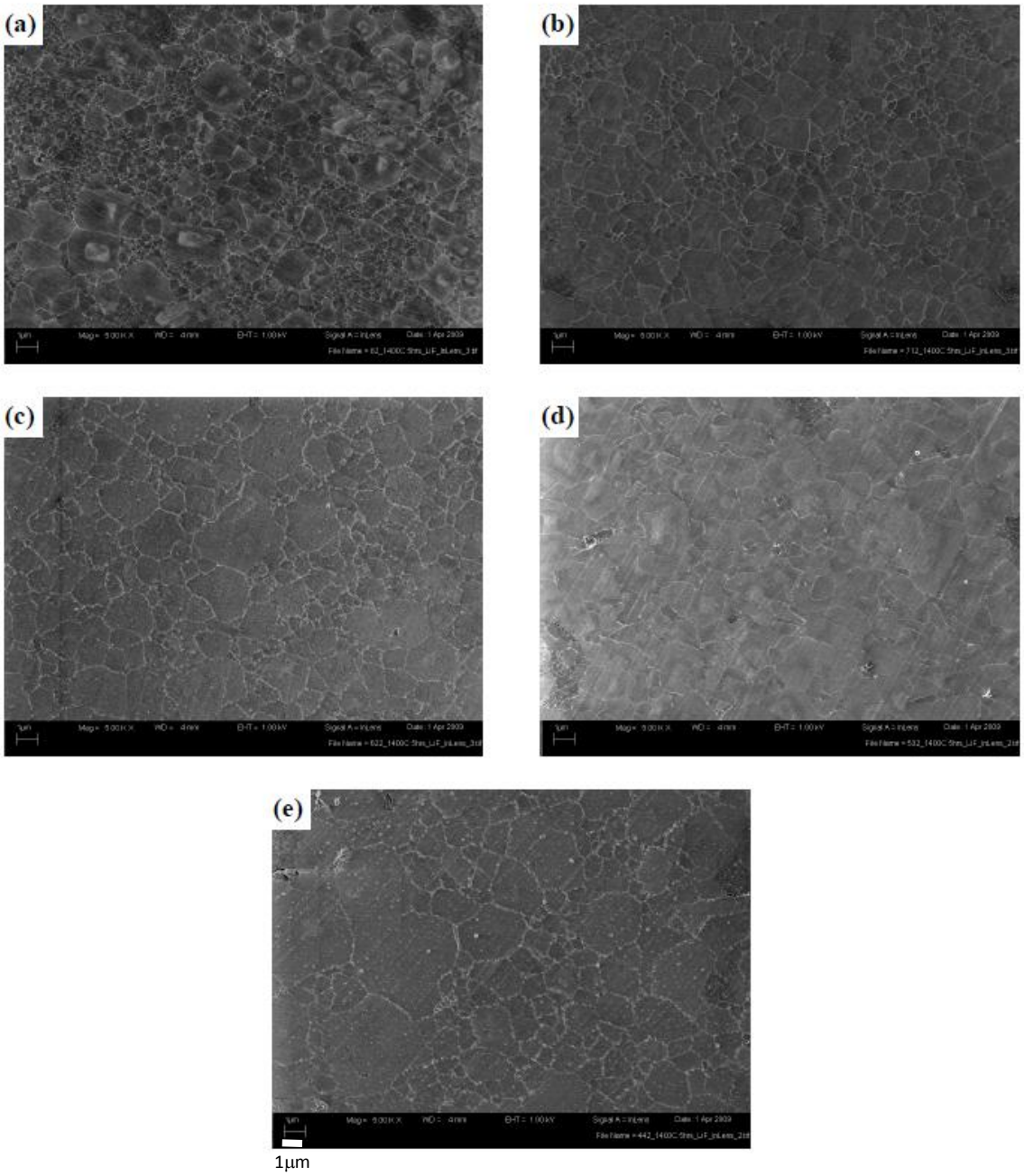

Figure 2.2.6 FE-SEM surface micrograph of sintered (a) $Ba(Zr_{0.8}Y_{0.2})O_{3-\delta}$, (b) $Ba(Zr_{0.7}Ce_{0.1}Y_{0.2})O_{3-\delta}$, (c) $Ba(Zr_{0.6}Ce_{0.2}Y_{0.2})O_{3-\delta}$, (d) $Ba(Zr_{0.5}Ce_{0.3}Y_{0.2})O_{3-\delta}$ and (e) $Ba(Zr_{0.4}Ce_{0.4}Y_{0.2})O_{3-\delta}$ sintered at 1400 ^{o}C for 5 hours.

and the protecting film in front of the detector blocks out the x-ray signal from lithium, if there is any lithium, and most of the signal from fluorine.

2.3 Electrochemical Studies of BZCY Ceramics

AC Impedance Spectroscopy is a powerful tool for characterizing electrical and interface physical properties of materials. When a frequency dependent electric field is applied, each physical property has its unique way to respond to the electric field. This behavior allows us to use this tool to study the proton conductivity of BZCYs.

2.3.1 Experimental Procedures

Electrochemical impedance data collection was carried out using a Solartron 1260 impedance analyzer with a 100 mV/cm applied ac field. For comparison, samples sintered at 1400 ^{o}C for 5 hours with LiF sintering additive and 1500 ^{o}C for 10 hours without LiF sintering additive were chosen for this study. Before the measurements, both sides of the samples were polished to remove any possible impurities and then brush-painted with silver paint (SPI Flash-Dry Silver Paint) to serve as electrodes. The samples were first heated to 850 ^{o}C with a 3^{o}C/min ramp rate and held at 850 ^{o}C for 5 hours to reach equilibrium to ambient atmosphere before measurements were taken. The impedance spectra were obtained in the frequency range of 0.1 Hz to 1 MHz between 850 ^{o}C and 75 ^{o}C with 25 ^{o}C steps in a water saturated (P_{H2O} = 3.5 kPa) 4% H_2 / 96% Ar atmosphere. ZView (Scribner Associates, Inc.) electrochemical impedance software was used for data analysis. At high temperature, ~400 ^{o}C and higher, the experiment encountered a limitation, that either the bulk arc or the grain boundary arc was no longer

accessible, because the characteristic frequency exceeded the measuring ability of our equipment. Therefore, the intersection value between the Z' axis and the data was taken as the total resistance of the sample.

2.3.2 Results and Discussion

Arrhenius plots of temperature dependent total electrical conductivities with different Ce content in water saturated (P_{H2O} = 3.5 kPa) 4% H_2 / 96% Ar atmosphere are shown in Fig. 2.3.1. The inset shows the Ce content versus total conductivities, which were measured at 700 ^oC for BZCYs/LiF and BZCYs. The total conductivities appear with two different slopes at low and high temperature ranges with a separating point ~550 ^oC. This change of slope at high temperature was attributed to loss of protons, e.g. the dehydration process, in materials at elevated temperature [8,9]. At high temperature, ~550 ^oC and above, the introduction of Ce into the BZY structure clearly increases the total conductivity. However, the total conductivities of BZCYs/LiF with less than 20% Ce dopant only increased slightly even though the grain size of $Ba(Zr_{0.6}Ce_{0.2}Y_{0.2})O_{3-\delta}$ has increase greatly due to the introduction of Ce. Comparing to BZCYs specimens, individual BZCYs/LiF have higher conductivities than those of BZCYs, except $Ba(Zr_{0.7}Ce_{0.1}Y_{0.2})O_{3-\delta}$ /LiF and $Ba(Zr_{0.7}Ce_{0.1}Y_{0.2})O_{3-\delta}$ have similar total conductivity. Although the reason for this increase in conductivity is not clear, a possibility is the accumulation of BaF_2 along the grain boundary, assuming BaF_2 can't go into the perovskite structure because of the different structure. Another could be the deficiency of Ba in the BZCYs/LiF, where LiF takes over Ba from BZCYs to form BaF_2, and increases the proton conductivity. The deficiency of A site cation in Y-doped ABO_3 resulting in

higher total conductivity has been reported by Ma *et al.* in Y-doped barium cerate and Ferreira *et al.* in Y-doped strontium zirconia systems [1,50]. According to NRA results, assuming all fluorine, which resided inside $Ba(Zr_{0.6}Ce_{0.2}Y_{0.2})O_{3-\delta}$/LiF, was in the form of BaF_2, the reaction leads to 2.22 and 1.55 mol% of barium deficiency in $Ba(Zr_{0.6}Ce_{0.2}Y_{0.2})O_{3-\delta}$/LiF, which have dwell times of zero and 5 hours respectively at 1400 ^{o}C. This small amount of BaF_2 is also the reason that we did not see any second phase in the XRD spectra. However, a possible simple reason could be that the higher

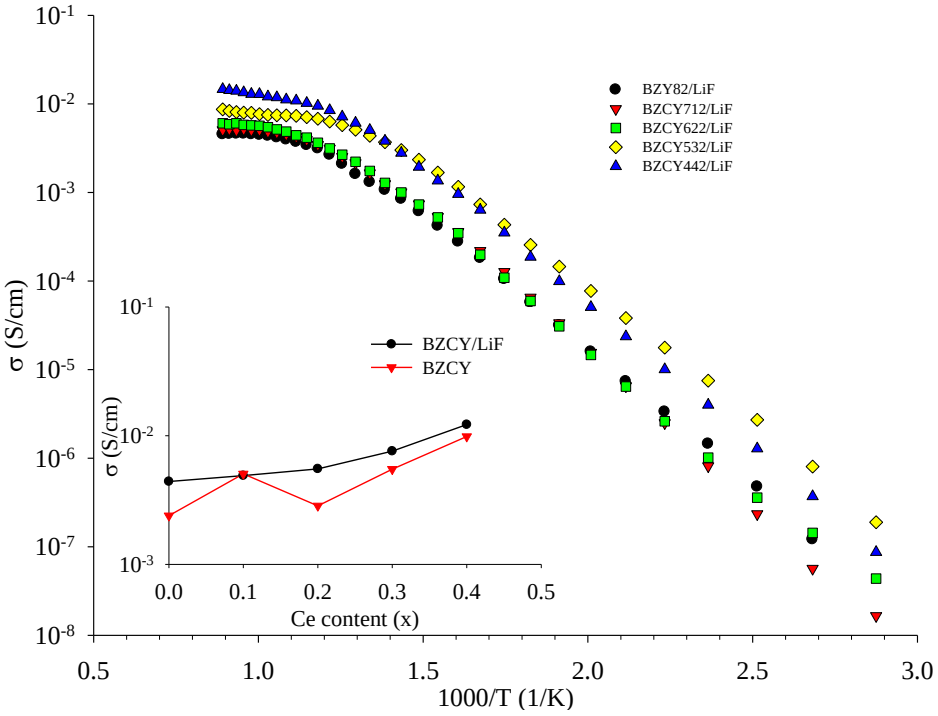

Figure 2.3.1 Total conductivity of BZCYs/LiF as a function of temperature plotted in Arrhenius form. The inset compares the total conductivity of BZCYs/LiF and BZCYs at 700 ^{o}C.

density of LiF added pellets gave better proton transport, which is similar to the better results that often come from higher density pellets, which are sintered at elevated temperature with long soaking time. For example, K. Nomura *et al.* reported a 96% relative density for $Ba(Zr_{0.8}Y_{0.2})O_{3-\delta}$ sintered at 1675 ^{o}C for 10 hours and measured a total conductivity of 4.2×10^{-3} S/cm at 600 ^{o}C in wet 40% H_2-60% Ar atmosphere, which is similar to the total conductivity of $Ba(Zr_{0.8}Y_{0.2})O_{3-\delta}$/LiF, 3.46×10^{-3} S/cm, at 600 ^{o}C in wet 4% H_2-96% Ar atmosphere [10]. Among the three reasons mentioned above, the argument for a slight deficiency of barium in the structure is the favored explanation from our point of view.

At temperatures lower than 350 ^{o}C, the impedance spectra can be analyzed by ZView software and different semicircles corresponding to grain interior, grain boundary and electrode response can be assigned. Due to the limitation of our facility, grain interior semicircles can only be seen at temperatures below 225 ^{o}C. The values for grain interior above 225 ^{o}C were taken to be the intercepts of the grain boundary semicircle and the real (Z´) impedance axis. Fig. 2.3.2(a) shows the temperature dependent grain interior conductivities of BZCYs/LiF. The inset at the left corner lists the activation energies, E_a, and pre-exponential factors, A, determined from a fit of the data to the Arrhenius equation

$$\sigma = A\exp(-\frac{E_a}{k_b T}). \qquad (2.3.1)$$

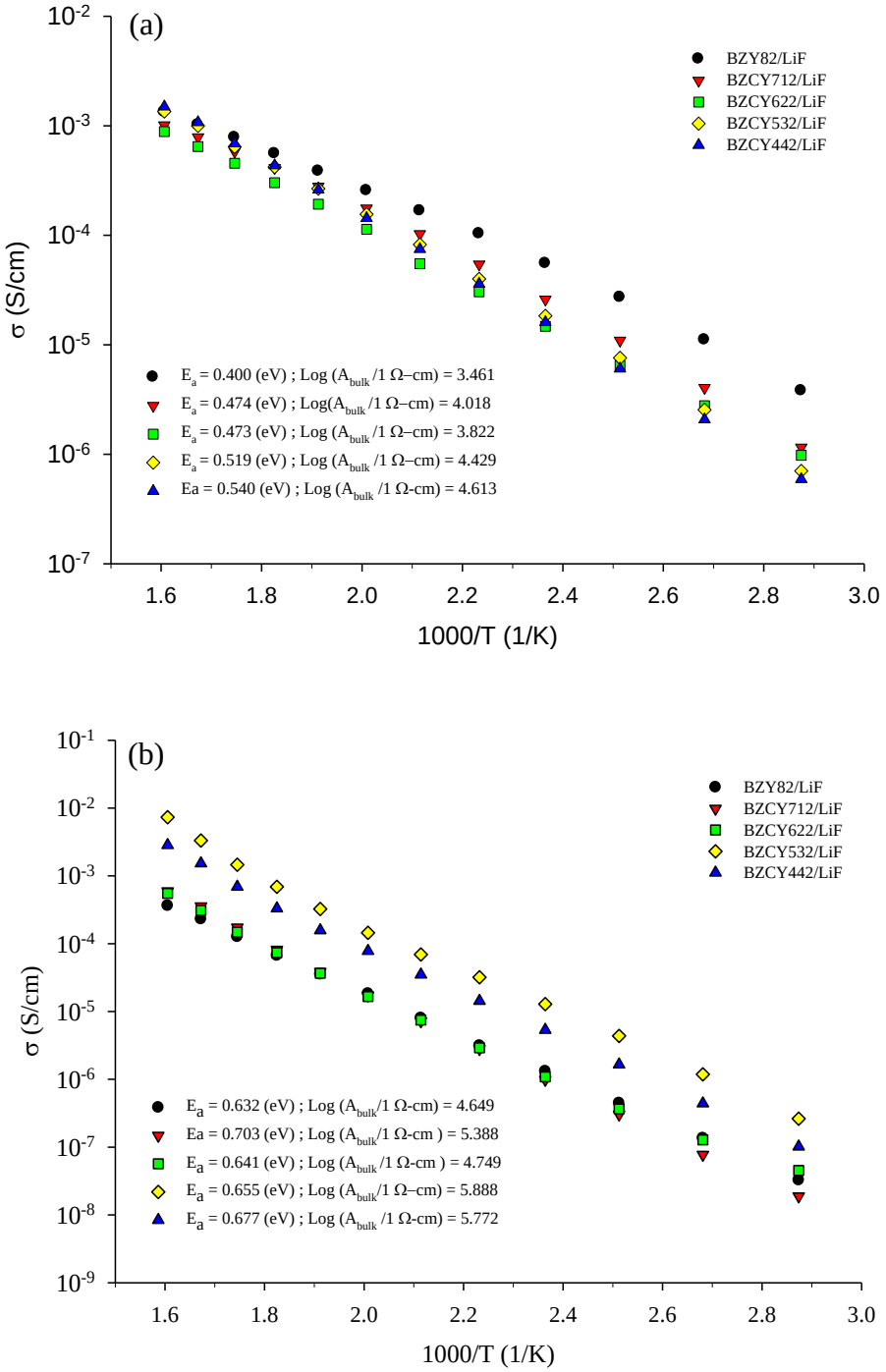

Figure 2.3.2 The conductivity of BZCYs/LiF (a) grain interior conductivity and (b) grain boundary conductivity. The insets show the activation energy and pre-exponential factor of the grain interior and grain boundary respectively.

Among the materials, $Ba(Zr_{0.8}Y_{0.2})O_{3-\delta}$/LiF has the highest grain interior conductivity with lowest activation energy. With the increase of Ce content, the grain interior conductivities decrease with an accompanying increase of activation energy. This behavior is consistent with Kreuer's report that $BaZrO_3$ should be a better proton conductor than $BaCeO_3$ by studying the quantum molecular dynamics [23]. For the grain boundary conductivities, samples with Ce content below 20% have similar proton conductivities and then increase the value when Ce content gets higher. If we take the geometry (effective length and area) of grain boundary into account, i.e. specific grain boundary conductivity [6], the value of grain boundary conductivities is about 2 orders of magnitude lower than the data shown in Fig. 2.3.2 (b). This means the total resistances of the BZCYs/LiF are more from grain boundary contributions than from the grain interior, which provides the information that the grain boundaries in perovskite BZCYs/LiF are not the favored pathways for fast proton transport at low temperature. Fig. 2.3.3 shows the temperature dependent grain interior and grain boundary conductivities of BZCYs. Comparing the conductivity measurements between BZCYs/LiF and BZCYs, the tendencies of the conductivities are similar, except the values of grain boundary are about an order of magnitude lower. This lower value of conductivity at grain boundary makes the total conductivity lower than that in BZCYs/LiF. The average activation energies of the grain interior and grain boundary are 0.031 eV and 0.058 eV higher in BZCYs/LiF than that of BZCYs, which also suggests the possibility of barium deficiency in the structure.

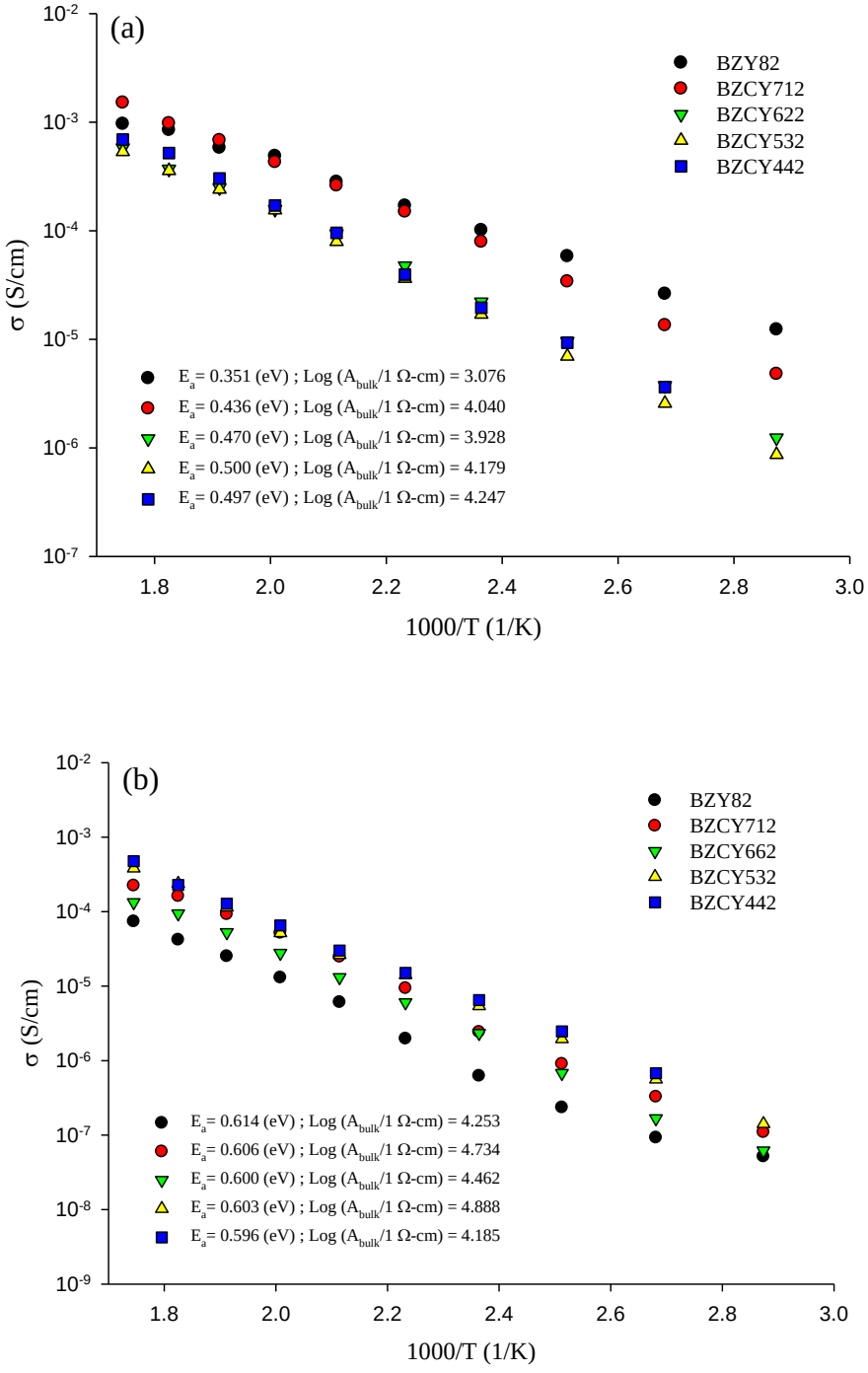

Figure 2.3.3 The conductivity of BZCYs (a) grain interior conductivity and (b) grain boundary conductivity. The insets show the activation energy and pre-exponential factor of the grain interior and grain boundary respectively.

2.4 Conclusions

Single phase $Ba(Zr_{0.8-x}Ce_xY_{0.2})O_{3-\delta}$ ($0 \leq x \leq 0.4$) powders were synthesized by the Glycine-Nitrate Process and Solid State Reaction. By introducing LiF sintering additive, the liquid phase of LiF and its product, $BaLiF_3$, melt incongruently around 850 ^oC. This encourages the diffusion between BZCYs particles, which results in high density ceramics at reduced sintering temperature (1400 ^oC) and dwell time (5 hours). The mechanical properties and stability of BZCYs are also improved by introducing LiF sintering additive. Nuclear reaction studies show there is no lithium and only a small amount of fluorine remaining inside the $Ba(Zr_{0.6}Ce_{0.2}Y_{0.2})O_{3-\delta}$/LiF samples, which indicates the non-concomitant departure of lithium and fluorine. The slightly higher activation energy at the grain and grain boundary of BZCYs/LiF than that of BZCYs implies the formation of barium deficiency in the material. Bimodal grain size distributions were observed in all BZCYs/LiF sintered pellets by FE-SEM. As Ce content increases, both small and big grains grow into larger micron-size grains but still keep the bimodal structure. Conductivity measurements show that $Ba(Zr_{0.8}Y_{0.2})O_{3-\delta}$ /LiF has the highest grain interior conductivity and decreases as Ce content increases. In contrast to that for the grain interior, grain boundary conductivities increase with increasing Ce content. When the geometry of the grain boundary is considered, the specific grain boundary conductivity was much lower than the grain interior conductivity, which indicates that the grain boundary is not the favored pathway for proton transport. Individual BZCYs/LiF have higher total conductivities at high temperature than BZCYs, which is likely the result of LiF causing a slight barium deficiency in the structure.

Overall, LiF is a good sintering additive for sintering BZCYs at lower temperature and makes BZCYs good candidates for serving as electrolytes in sensors and fuel cells.

CHAPTER 3

FABRICATION AND TESTING OF SOLID OXIDE FUEL CELLS

In solid oxide fuel cell (SOFC) applications, most designs are focused on planar and tubular structure. Planar SOFCs can be further classified into three categories, which are electrolyte-supported cell, anode-supported cell and cathode-supported cell. However, the cathode-supported cell is not favored because of the lower electronic conductivity of cathode material and the failure problem during thermal cycling caused by a big difference in thermal expansion coefficients between cathode and electrolyte material.

Electrolyte-supported planar SOFCs use the electrolyte to support thin electrodes on either side. The advantages of this configuration are relatively strong structural support from dense electrolyte and little susceptibility to a failure due to anode re-oxidation. The disadvantage is that the system needs to be run at higher temperature, 900-1000 ^{o}C, to minimize the ohmic polarization from the thick electrolyte.

In an anode-supported planar SOFC, a thick porous anode is used to support a thin electrolyte and cathode. This design allows the cell to run at lower temperature, 600-800 ^{o}C. Thus, low cost metallic materials such as ferritic stainless steels can be used as interconnects to reduce the overall cost of the system. However, the anode re-oxidation in the thermal cycles may cause failure of the system. Mass transport limitations due to the thick anode also constrain the power output at high current density.

3.1 Solid Oxide Fuel Cell Fabrication

3.1.1 Electrolyte-Supported Cells

The BZCY powders were prepared by the Glycine-Nitrate Process as described in Chapter 2. The powders were planetary ball milled with 7 wt% lithium fluoride and ethanol for 4 hours at 150 rpm, individually. After drying the solutions, the powders were uni-axial die-pressed into one inch discs and sintered at 1400 ^{o}C for 5 hours to form high density hard discs with a diameter ~2 cm. The discs were then polished down to 300 μm thickness to serve as electrolyte. Nickel oxide mixed with BZCY powder, individually, was screen printed on the electrolytes and sintered at 1300 ^{o}C for two hours to serve as anodes. Then, cathode materials including platinum, $(La_{0.8}Sr_{0.2})MnO_{3-\delta}$ (LSM), $(La_{0.6}Sr_{0.4})(Fe_{0.8}Co_{0.2})O_{3-\delta}$ (LSCF), $La_{0.5}Sr_{0.5}CoO_{3-\delta}$ (LSC) and $Ba(Ce_{0.4}Pr_{0.4}Y_{0.2})O_{3-\delta}$ (BCPY) were applied on the other side of the electrolytes by screen printing and sintered at 1000 ^{o}C for two hours to serve as cathodes.

3.1.2 Anode-Supported Cells

For anode-supported SOFCs, only $Ba(Zr_{0.6}Ce_{0.2}Y_{0.2})O_{3-\delta}$ and $Ba(Ce_{0.8}Y_{0.2})O_{3-\delta}$ were chosen to serve as electrolyte in the cells because $Ba(Zr_{0.6}Ce_{0.2}Y_{0.2})O_{3-\delta}$ is chemically stable in 100% CO_2 atmosphere with acceptable proton conductivity and $Ba(Ce_{0.8}Y_{0.2})O_{3-\delta}$ is one of the highest proton conductivity materials discovered so far.

To prepare supporting anodes, the $Ba(Zr_{0.6}Ce_{0.2}Y_{0.2})O_{3-\delta}$ and $Ba(Ce_{0.8}Y_{0.2})O_{3-\delta}$ powders were weighed and mixed with NiO at volume ratio 1 to 2, individually. In addition to ceramic powders, 10 to 8 wt% cornstarch of the total solid load, depending

upon what percent of porosity is needed, was added to serve as pore former. The powders were then planetary ball milled with ethanol at 150 rpm for two hours. After drying, the powders were uni-axial die-pressed with a ¾" die to form green pellets with thickness ~1.35 mm to serve as supporting anode.

Other structure layers were prepared by applying ceramic inks on the green anode-support pellets. To prepare the inks, solid powder loads were mixed with alpha terpinol, ethylcellulose, oleic acid and xylene by a THINKY mixer at 1000 rpm for 10 minutes to form the inks. Then, green anode-supported pellets were first coated with an ink, which was made from a mixture at volume ratio 1:1 to serve as anode interlayer. After drying, another layer made from electrolyte material was applied. Then, the pellets were re-pressed by the uni-axial die press and sintered in air at a temperature of 1400 ^{o}C for 5 hours to form a well-bonded electrolyte-anode structure. Cathode material, LSM, was then applied on the sintered pellets and fired to 1000 ^{o}C in air for two hours to form a good bond between cathode and electrolyte.

3.1.3 The Measurement of Cell Performance

A home-made seal-less testing system from Inconel 600 was used for the measurements, Fig. 3.1.1. Silver mesh and nickel foam were used as cathode and anode current collectors, respectively. The total input gas flow rates on each side were controlled by MKS mass flow controllers at 200 ml/min in all experiments. The water vapor concentration in fuel gas was about 3% by flowing the fuel gas through a water bubbler at room temperature. Measurements were carried out at temperature between

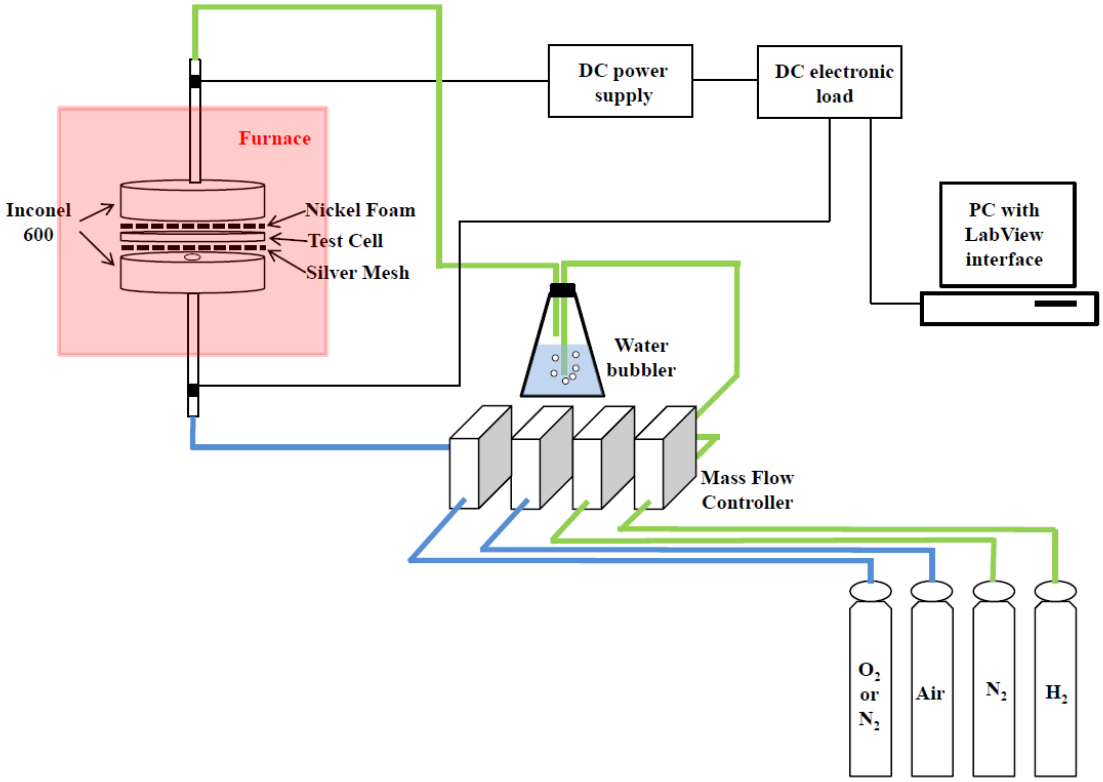

Figure 3.1.1 Schematic of fuel cell test system.

600 ^{o}C and 800 ^{o}C at ambient pressure. All cells were reduced in situ at high temperature in a 60% H_2 + 40% N_2 mixture for more than an hour prior to the measurements.

SOFC performance was measured using various fuel gas and oxidative gas mixtures, i.e. at various partial pressures of H_2/N_2 in fuel gas and O_2/N_2 in oxidative gas while the total flow rate of the gas on each side was kept constant at 200 ml/min. Current densities were calculated based on the cathode area.

3.1.4 Cell Characterization

Porosity of the supported anode was measured using Archimedes' method. The tested cell, after reducing, was broken into two pieces. One of the pieces was polished to erase the cathode and electrolyte layers and cleaned with an ultrasonic bath in ethanol. The sample was then kept in a dry oven at 95 ^{o}C for more than two hours to evaporate the ethanol. Dry weight, W_{dry}, wet weight, W_{wet}, and weight saturated with ethanol, W_{sat}, were measured using a high accuracy balance. Prior to measuring W_{wet} in ethanol, the sample was immersed in ethanol and kept in vacuum for 10 minutes to remove possible air in the pores. The W_{sat} was measured in air soon after the surface of the sample was shaken dry. Porosity was calculated by using the equation

$$Porosity\ (\%) = \frac{W_{sat} - W_{dry}}{W_{sat} - W_{wet}} \times 100\%. \qquad (3.1.1)$$

The other part of the cell was hardened in an epoxy and polished. Field Emission Scanning Electron Microscopy (SUPRA^{TM} 55 Versatile High Performance FE-SEM, Zeiss) was used to examine the microstructure of the cell. The mean pore radius of the cell was determined by quantitative measurements of the pore size on SEM images.

3.2 Results and Discussion

3.2.1 Electrolyte-Supported SOFC

Fig. 3.2.1 shows the microstructure images from an electrolyte-supported $Ba(Zr_{0.6}Ce_{0.2}Y_{0.2})O_{3-\delta}$ fuel cell after tests. It was found that the anode, Ni/ $Ba(Zr_{0.6}Ce_{0.2}Y_{0.2})O_{3-\delta}$, and cathode, LSM, were about 10 μm in thickness. The same configurations were also found on other cells with different cathode materials, except Pt electrodes had a thickness of about 2 μm. It can be seen that the bonding between electrodes and electrolyte is very good.

The I-V curves and power densities of electrolyte supported Pt | BZCYs/LiF | Pt solid oxide fuel cells tested at 800 ^{o}C are shown in Fig. 3.2.2 (a) and 500 ^{o}C to 850 ^{o}C

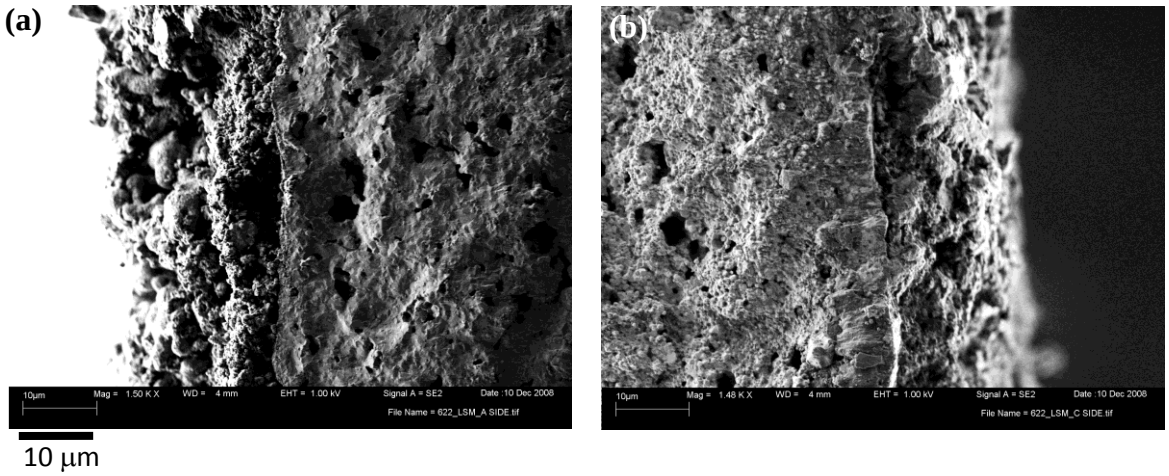

Figure 3.2.1 SEM images of $Ba(Zr_{0.6}Ce_{0.2}Y_{0.2})O_{3-\delta}$ electrolyte supported SOFC at interface between (a) electrolyte and Ni/$Ba(Zr_{0.6}Ce_{0.2}Y_{0.2})O_{3-\delta}$ anode, (b) electrolyte and LSM cathode.

temperature dependent peak power outputs are shown in Fig. 3.2.2 (b). It is clear that the maximum power outputs increase with increasing Ce content of the electrolyte. This tendency of the temperature dependent peak power output is consistent with the BZCYs/LiF total conductivity measurements at high temperature, Fig 2.3.1. The power outputs of electrolyte supported BZCYs/LiF cells are relatively low in our tests. This result is mainly attributed to the ohmic polarization from the thick electrolyte, as indicated by the almost constant slopes of I-V curves in Fig. 3.2.2 (a). However, the low power output is also a result from the relativly low total conductivity of BZCYs/LiF when compared to 8 mol% Y-doped zirconia (8YSZ) at temperatures higher than 600 ^{o}C. This suggests that a higher amount of Ce must be introduced into the material to produce a power output comparable to 8YSZ SOFC at temperature higher than 600 ^{o}C.

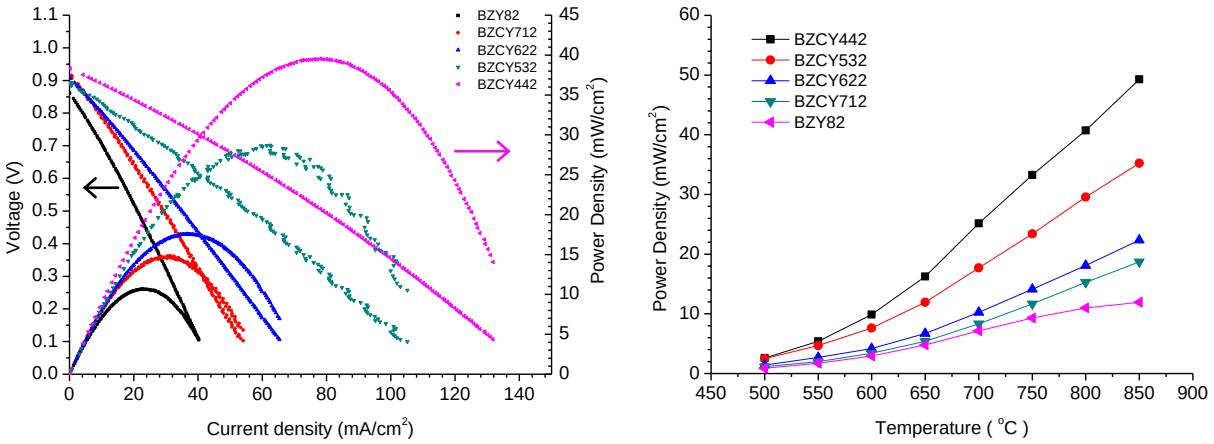

Figure 3.2.2 BZCYs/LiF electrolyte-supported fuel cell with platinum electrodes (a) I-V curves and power density outputs at 800 ^{o}C and (b) temperature dependence of maximum power outputs from 500 ^{o}C to 850 ^{o}C.

The development of compatible cathode material for H-SOFCs is in its early stage and remains as a big challenge. Conventionally, these mixed oxygen ion and electronic conductor cathodes are mostly designed for O-SOFCs and may or may not be adequate for practical use in H-SOFCs when a reducing atmosphere is generated at the interface between proton conductive electrolyte and the cathode. Fig. 3.2.3 shows the performances of BZCYs/LiF electrolyte-supported cells with different cathode materials, including Pt, LSM, LSC, LSCF and BCPY. The linear I-V curves show ohmic polarization is still the major loss mechanism limiting the cell performance. Among the cathode materials, Pt, which is known as the best hydrogen and oxygen molecule dissociation catalyst, gave the best power outputs and BCPY gave the lowest. The huge difference in power output for Pt compared to other cathode materials suggests finding some other adequate cathode material is important for H-SOFC development.

It is interesting to note that LSC gave better performance with Ce content increase in the electrolyte. To investigate this phenomenon, mixtures between $Ba(Zr_{0.4}Ce_{0.4}Y_{0.2})O_{3-\delta}$ and all four cathode materials, at weight ratio 1:1, were pressed into pellets and fired to 900, 1000, 1100 and 1200 ^{o}C for two hours, respectively. The X-ray diffraction results, Fig. 3.2.4, show that there was no observable chemical reaction between $Ba(Zr_{0.4}Ce_{0.4}Y_{0.2})O_{3-\delta}$ and BCPY, LSM and LSCF. However, the mixture of $Ba(Zr_{0.4}Ce_{0.4}Y_{0.2})O_{3-\delta}$ and LSC did show a new phase near $2\theta=32^{o}$ when the pellets were fired to a temperature higher than 1000 ^{o}C. The peaks corresponding to $Ba(Zr_{0.4}Ce_{0.4}Y_{0.2})O_{3-\delta}$ were shifted to the right, indicating that a smaller element was

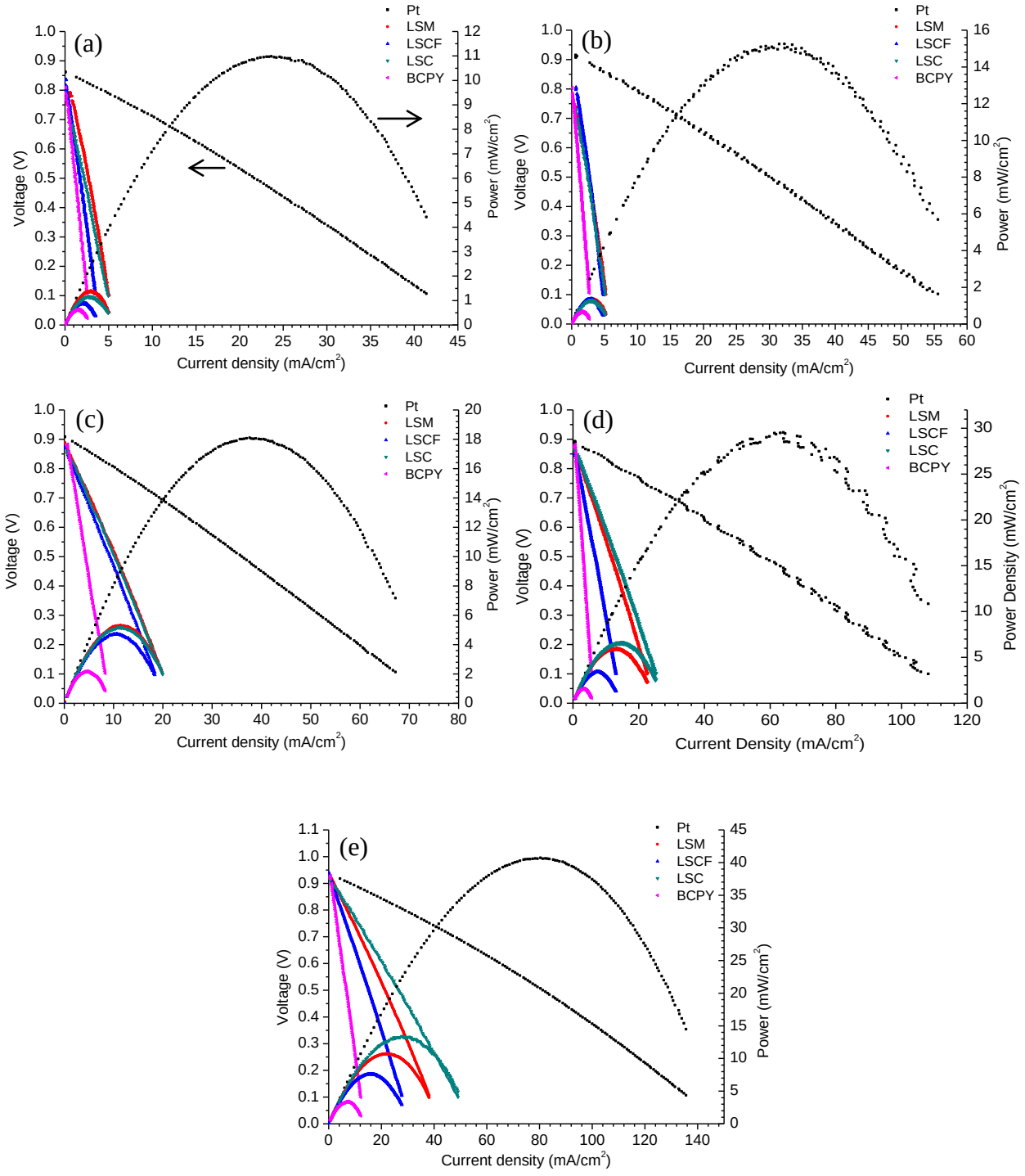

Figure 3.2.3 Cell performances with different cathode materials at 800 ^{o}C for (a) $Ba(Zr_{0.8}Y_{0.2})O_{3-\delta}$, (b) $Ba(Zr_{0.7}Ce_{0.1}Y_{0.2})O_{3-\delta}$, (c) $Ba(Zr_{0.6}Ce_{0.2}Y_{0.2})O_{3-\delta}$, (d) $Ba(Zr_{0.5}Ce_{0.3}Y_{0.2})O_{3-\delta}$ and (e) $Ba(Zr_{0.4}Ce_{0.4}Y_{0.2})O_{3-\delta}$.

doped into $Ba(Zr_{0.4}Ce_{0.4}Y_{0.2})O_{3-\delta}$. By looking at the elements, the most possible is the replacing of Ce ions at B-sites by Co ions. Yang *et al.* reported that Co-doped BZCY is an excellent mixed proton-electronic conductor [51]. The presence of this mixed ion conductor material allows protons to travel from the electrolyte into the cathode and results in more reaction area to give better performance. Further research on finding the reaction between $Ba(Zr_{0.4}Ce_{0.4}Y_{0.2})O_{3-\delta}$ and LSC may provide information for making good cathode material for H-SOFCs.

3.2.2 Anode-Supported SOFC

$Ba(Zr_{0.6}Ce_{0.2}Y_{0.2})O_{3-\delta}$ Anode Supported SOFC Because of its complete stability in 100% CO_2 atmosphere and relatively high ionic conductivity, $Ba(Zr_{0.6}Ce_{0.2}Y_{0.2})O_{3-\delta}$ was first chosen for making anode-supported H-SOFCs [11]. Other concerns such as chemical reaction between BZCY and cathode material were also considered. Therefore, to simplify the test, LSM was chosen as cathode since there is no reaction between LSM and $Ba(Zr_{0.4}Ce_{0.4}Y_{0.2})O_{3-\delta}$ up to 1200 ^{o}C as shown in Fig. 3.2.4

Fig. 3.2.5 shows the microstructure and configuration of anode-supported SOFCs. The fabricated $Ba(Zr_{0.6}Ce_{0.2}Y_{0.2})O_{3-\delta}$ electrolyte has thickness about 40 μm and is completely dense. The cathode is LSM which was sintered at 1000 ^{o}C for two hours. The electrochemical performances of an anode supported $Ba(Zr_{0.6}Ce_{0.2}Y_{0.2})O_{3-\delta}$ cell at 700 ^{o}C under different hydrogen partial pressures are shown in Fig. 3.2.6. The peak power densities are 154, 148, 136, 126 and 113 mW/cm^2 for 80%, 60%, 40%, 30% and

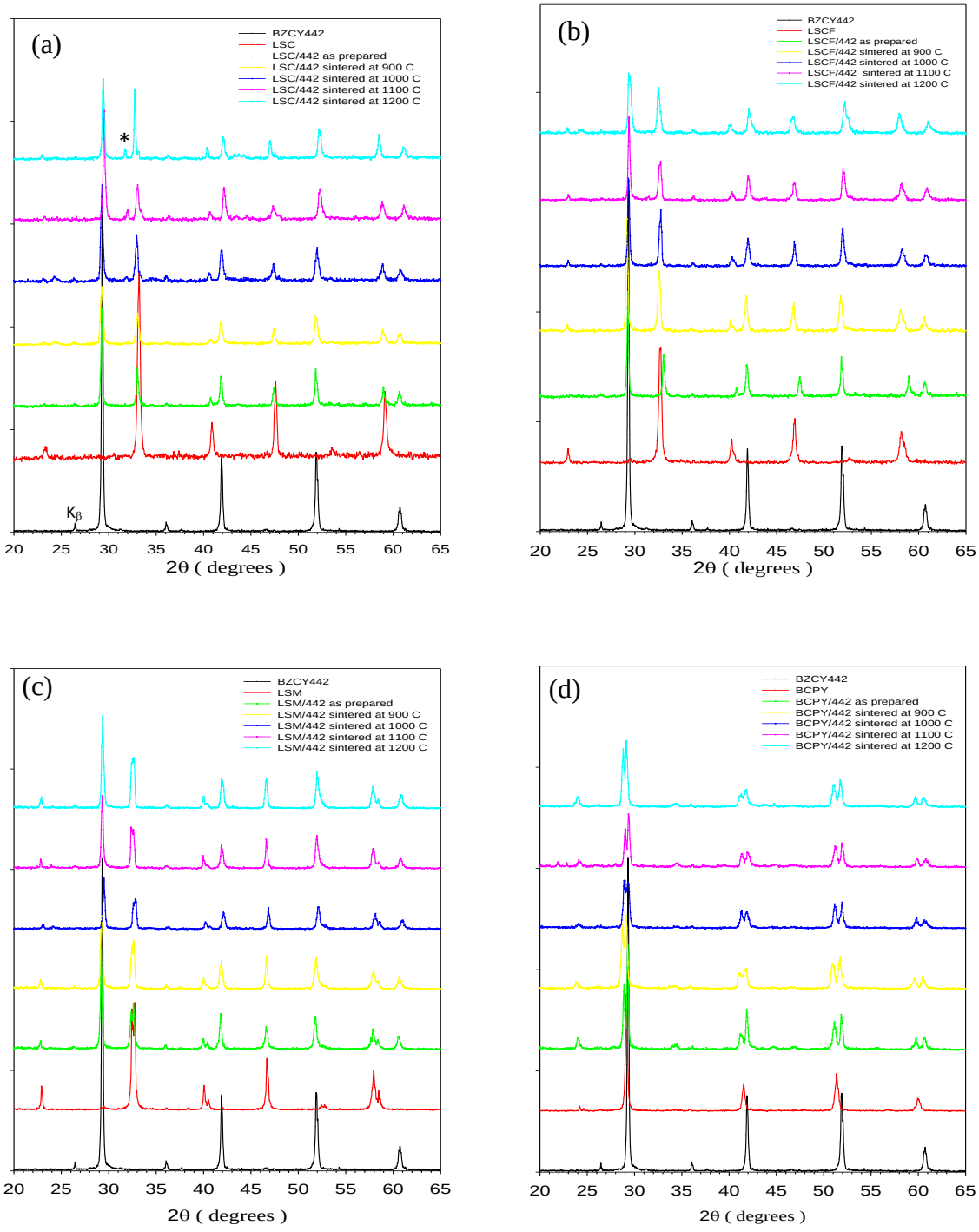

Figure 3.2.4 X-ray diffraction results for different sintering temperatures of mixture between $Ba(Zr_{0.4}Ce_{0.4}Y_{0.2})O_{3-\delta}$ and (a) LSC, (b) LSCF, (c) LSM and (d) BCPY.

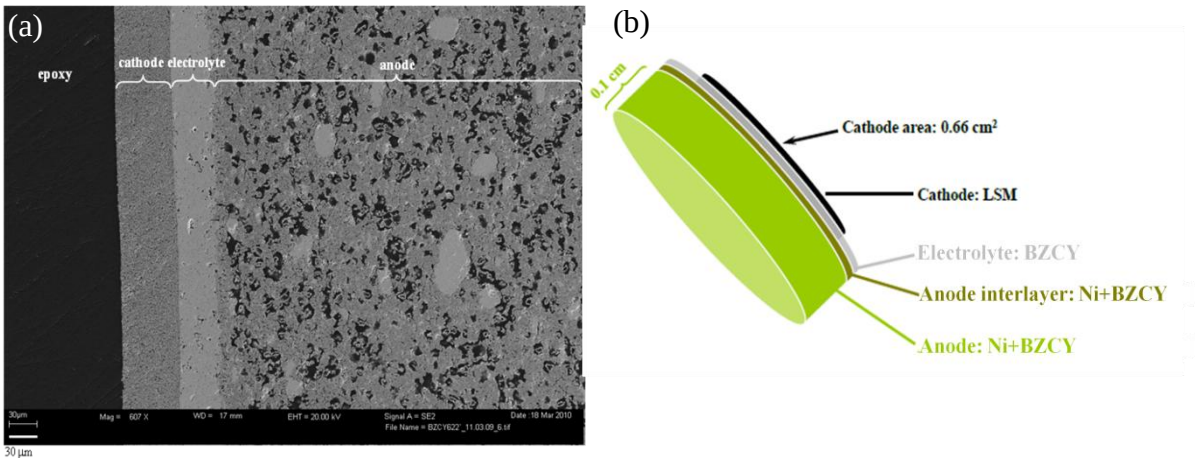

Figure 3.2.5 (a) Microstructure of anode supported $Ba(Zr_{0.6}Ce_{0.2}Y_{0.2})O_{3-\delta}$ cell and (b) configuration of anode supported cell.

20% hydrogen concentration, respectively. When examining the I-V curves, the almost linear I-V curves imply the losses from activation and concentration polarization are small. Even when H_2 partial pressure was as low as 20% and the electrolyte was as thin as 40 μm, the concentration polarization of the cell still could not be seen. To observe saturation current density, a relatively thick supporting anode is needed for $Ba(Zr_{0.6}Ce_{0.2}Y_{0.2})O_{3-\delta}$. However, the low power outputs of anode supported $Ba(Zr_{0.6}Ce_{0.2}Y_{0.2})O_{3-\delta}$ cells suggest $Ba(Zr_{0.6}Ce_{0.2}Y_{0.2})O_{3-\delta}$ is not good enough for practical use. The low ionic conductivity needs to be improved by increasing Ce content or finding another suitable dopant, which doesn't decrease its chemical stability but increases its proton conductivity. In order to find the tortuosity of the supporting anode and to do H-SOFC modeling, it is necessary for us to find saturation current density

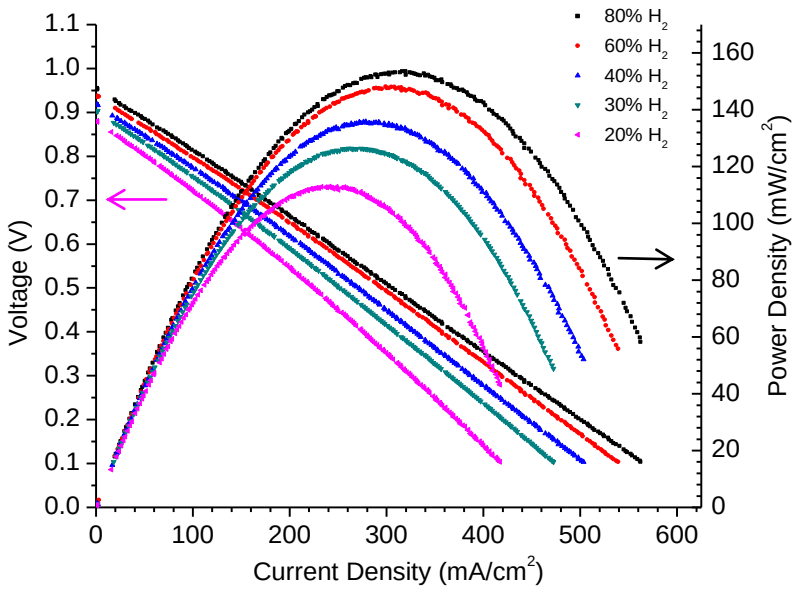

Figure 3.2.6 The electrochemical performances of $Ba(Zr_{0.6}Ce_{0.2}Y_{0.2})O_{3-\delta}$ anode supported cell under different H_2 partial pressures at 700 ^oC.

under concentration polarization. Therefore, the idea of choosing $Ba(Zr_{0.6}Ce_{0.2}Y_{0.2})O_{3-\delta}$ was discarded and $Ba(Ce_{0.8}Y_{0.2})O_{3-\delta}$ was then chosen for further research.

<u>$Ba(Ce_{0.8}Y_{0.2})O_{3-\delta}$ Anode Supported SOFC</u> $Ba(Ce_{0.8}Y_{0.2})O_{3-\delta}$ has one of the highest proton conductivities discovered among the perovskite ceramics. Its chemical instability in CO_2 and high H_2O containing atmosphere is a drawback for its serving as electrolyte in SOFCs because of the formation of proton insulating $BaCO_3$ and CeO_2 [52-54]. However, this problem can be excluded by using H_2 as fuel instead of using carbon containing fuel.

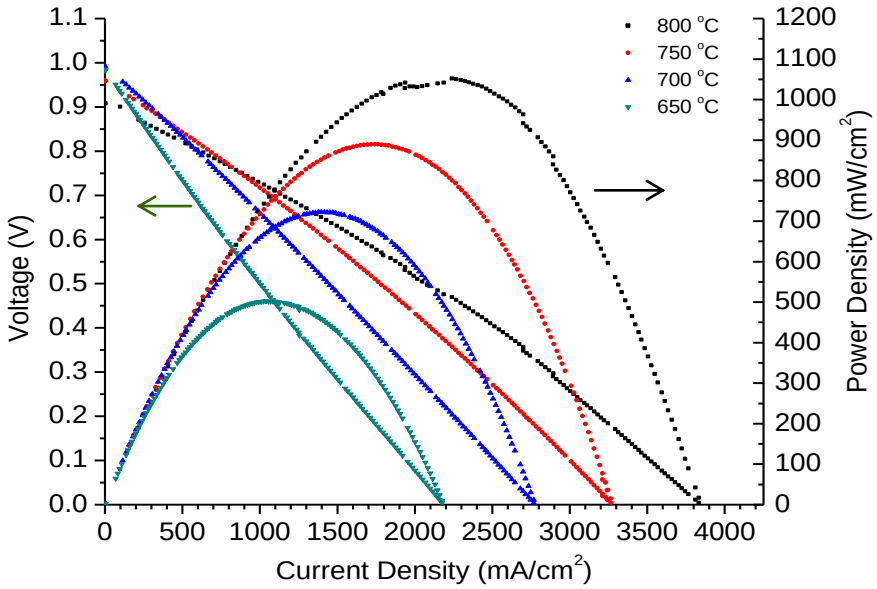

Figure 3.2.7 Temperature dependent electrochemical performances of $Ba(Ce_{0.8}Y_{0.2})O_{3-\delta}$ anode supported cell using 60% H_2 + 40% N_2 as fuel.

Fig. 3.2.7 shows the temperature dependent electrochemical performances of an anode supported $Ba(Ce_{0.8}Y_{0.2})O_{3-\delta}$ H-SOFC using 60% H_2 + 40% N_2 as fuel gas. The peak power densities are 1052, 889, 722 and 503 mW/cm^2 at temperature 800, 750, 700 and 650 ^oC, respectively. These performances are very good, especially at low temperature ranges when compared to oxygen ion conductor cells, e.g. 10 μm thick 8YSZ electrolyte and LSM-8YSZ cathode showed 850, 625, 430 and 275 mW/cm^2 at temperature 800, 750, 700 and 650 ^oC, respectively [55]. The high open circuit voltage, ~1 V at 700 ^oC, indicates the $Ba(Ce_{0.8}Y_{0.2})O_{3-\delta}$ electrolyte is sufficiently dense and the electronic conduction should be negligibly small.

The I-V curve dependences on H_2 partial pressures on anode fuel gas while air was used on the cathode side are shown on Fig. 3.2.8 (a). The convex I-V curve of 20% H_2 indicates concentration polarization came into play when high current density was driven from the cell. However, the loss from ohmic polarization still dominated when high H_2 partial presssure fuel gases were used. It is interesting to note that the peak power outputs increase dramatically from 20% to 60% H_2 partial pressure but saturate when higher H_2 partial pressure gases are used, with almost no change between 80% and 100% H_2. The same test was done on an oxygen ion conductor YSZ cell and this behavior was not seen, Fig 3.2.9. This behavior will be explained later by our model in Chapter 5.

A series of oxygen partial pressure dependent tests for cathode oxidative gases with 100% H_2 as anode fuel gas is shown on Fig. 3.2.8 (b). It is surprising that the cell

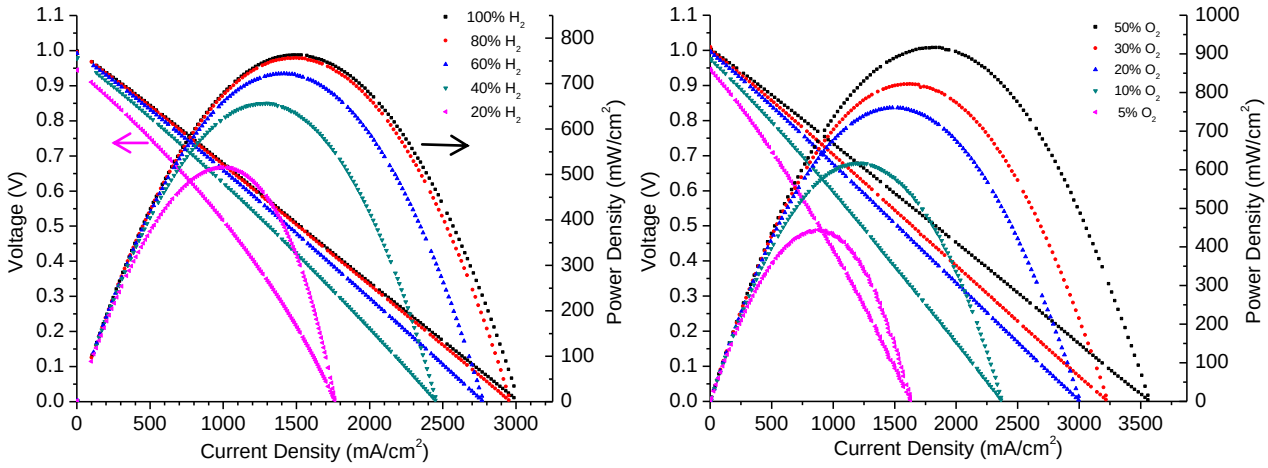

Figure 3.2.8 Electrochemical performances of a $Ba(Ce_{0.8}Y_{0.2})O_{3-\delta}$ anode supported cell for (a) H_2 partial pressure dependent tests on anode side and (b) O_2 partial pressure dependent tests on cathode side.

can be run with O_2 partial pressure as low as 5% without encountering serious concentration polarization from the cathode side. The peak power outputs clearly increase with increasing O_2 partial pressure. However, the producing of steam on the cathode side of H-SOFCs makes it a problem if it is economically efficient to use high O_2 concentration gas instead of air to run the system.

Fig. 3.2.10 shows the microstructure of the tested cell. The dense electrolyte is ~30 μm in thickness and adheres to a ~25 μm anode interlayer very well. The average pore size of the anode is about 1.42 μm in diameter, which was calculated quantitively from SEM pictures. The thickness of the support anode was about 1.15 mm with a porosity ~ 44%.

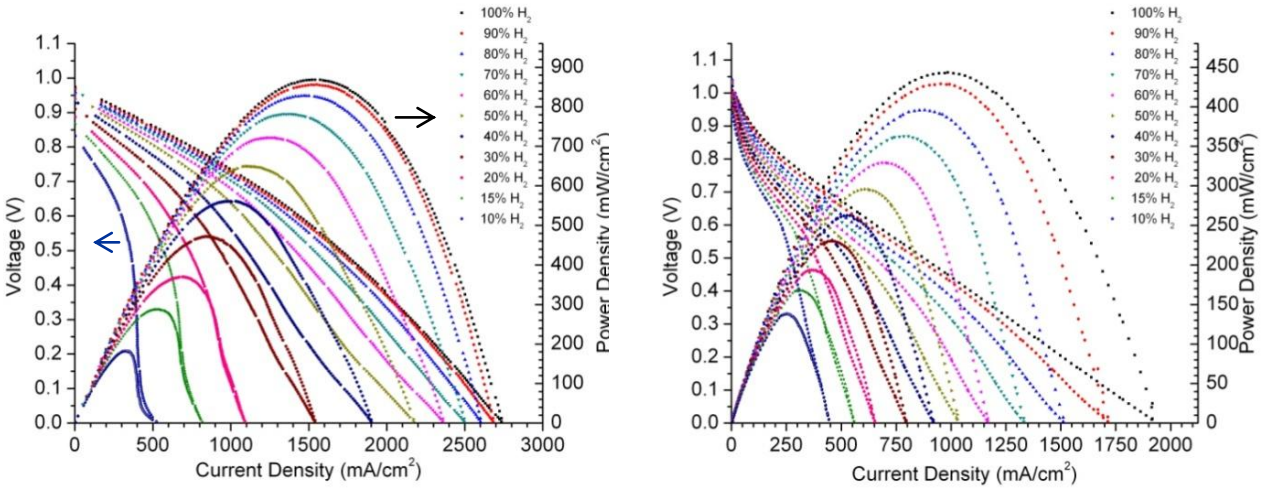

Figure 3.2.9 Hydrogen partial pressure dependent electrochemical performance of (a) $Ba(Ce_{0.8}Y_{0.2})O_{3-\delta}$ and (b) 8YSZ anode supported SOFC at 800 ^oC.

For the purpose of tortuosity investigation, another batch of anode-supported $Ba(Ce_{0.8}Y_{0.2})O_{3-\delta}$ H-SOFCs with lower porosity, ~34%, and different anode thicknesses, from 1.85 mm to 1 mm, were made. Fig. 3.2.9 (a) shows the electrochemical performances of a $Ba(Ce_{0.8}Y_{0.2})O_{3-\delta}$ anode-supported H-SOFC with a 1.5 mm-thick anode. The test was at a temperature of 800 ^{o}C under different H_2 partial pressures while air was used as oxidant at the cathode. An anode-supported oxygen ion conductor 8YSZ SOFC with the same thickness anode was also made and tested under the same conditions for comparison, Fig. 3.2.9 (b). The convex I-V curvatures of the $Ba(Ce_{0.8}Y_{0.2})O_{3-\delta}$ H-SOFC indicates the activation and ohmic polarization loss of the cell are small compared to the concentration polarization. The concentration polarization effect is easily seen when the cell was running at high current density with H_2 partial pressure less

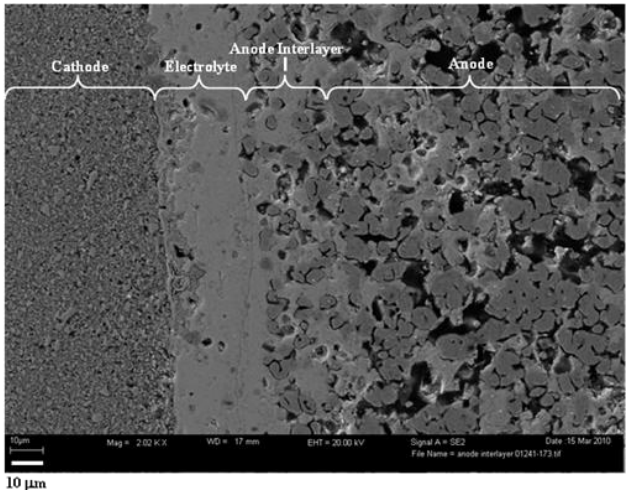

Figure 3.2.10 Microstructure of $Ba(Ce_{0.8}Y_{0.2})O_{3-\delta}$ anode supported H-SOFC from SEM image.

than 30%, in the convex curvatures with straight down feature of the I-V curve. Contrary to the $Ba(Ce_{0.8}Y_{0.2})O_{3-\delta}$ H-SOFC, the 8YSZ O-SOFC has concave I-V curves for low current density. This feature implies that activation polarization dominates the loss at low current density. Then, depending on H_2 partial pressure, the losses from ohmic and concentration polarization become significant when current density runs up.

When examining the I-V curves from $Ba(Ce_{0.8}Y_{0.2})O_{3-\delta}$ cells, we notice the current density increases rapidly at low voltage, e.g. at voltage lower than 0.05 V for 10% H_2 partial pressure on Fig. 3.2.9 (a). The same feature was not seen on 8YSZ O-SOFC and has never been reported by other groups. Conventionally, we expect a straight down I-V curve when concentration polarization dominates, using up all of the fuel gas at the anode-electrolyte interface, and giving a saturation current density. The reason for this behavior remains unclear and is worth further study in the future.

3.3 Conclusions

Proton conductive perovskite BZCY has been demonstrated to have the ability to serve as an electrolyte for SOFCs. With LiF addition, high density ceramic can be made and used for fabricating electrolyte supported H-SOFCs. The test results of electrolyte-supported cells result in low power outputs due to their thick electrolytes and relative low proton conductivities. Cells with Pt electrodes had much higher power output, implying that an adequate but less expensive cathode for H-SOFC should be developed.

A $Ba(Zr_{0.6}Ce_{0.2}Y_{0.2})O_{3-\delta}$ anode-supported H-SOFC with electrolyte thickness ~40 μm using LSM as cathode only gave peak power output ~150 mW/cm^2. By inspecting

its I-V curves, the power outputs are mainly limited by ohmic polarization, which results from low proton conductivity. Although $Ba(Zr_{0.6}Ce_{0.2}Y_{0.2})O_{3-\delta}$ has very high chemical stability, the low power output makes it impractical for commercial use.

$Ba(Ce_{0.8}Y_{0.2})O_{3-\delta}$ anode-supported H-SOFCs using LSM as cathode show excellent power output. The peak power outputs increase dramatically with H_2 pressure at low H_2 partial pressure, but saturate when higher H_2 partial pressure gases are used. When different oxygen partial pressures are used on the cathode, the peak power densities increase with increasing O_2 partial pressure. The electrochemical performances using different H_2 and O_2 partial pressures provide information for H-SOFC modeling. By changing the thickness of the supported anode, saturated current density due to concentration polarization can be seen. From the saturated current density, tortuosity of the anode can be calculated and this information can be used for improving microstructure construction.

CHAPTER 4

TORTUOSITY IN ANODE-SUPPORTED SOLID OXIDE FUEL CELLS FOUND FROM GAS AND CURRENT FLOW RATES

For modern SOFCs, strong efforts are in progress to extend the operating temperature down to the 600-800 ^{o}C range. The low operating temperature would increase the benefit of using low cost interconnect material, such as stainless steel, and also reduce problems associated with thermal expansion, atomic migration and corrosion. Accordingly, the electrolyte is made as thin as possible to reduce ohmic loss from transferring ions through electrolyte. The electrolyte thickness is usually down to the 20 μm range and requires that an electrode layer, usually the anode, must be made thick enough to mechanically support the cell.

With a thicker anode, gas concentrations at the anode-electrolyte interface need to be calculated carefully because they strongly affect the terminal voltage V as a function of electrolyte current density i, especially in the high current density range. A key parameter in determining the pressure gradient is the tortuosity τ, which is the ratio of the typical diffusion path length to the electrode thickness. Measurement of its value is needed for determining the quality of the anode pore configuration and necessary for any *V(i)* modeling. Many modern SOFC models do not adequately calculate the value of τ and invoke anode tortuosities in the range as high as 10 to 17 [56,57]. Such high tortuosities do not seem physically reasonable when the porosity is usually higher than 30% of the supporting anode.

The impact of such high tortuosity (10 to 17) is to produce concentration polarization easily when running the cell. With this misleading analysis, one might think decreasing the anode thickness or increasing its porosity would be advantageous. But, these designs always come with the expense of structural integrity. Tortuosity calculations from our tested cells indicate that high tortuosity values may not be correct. The results also provide more accurate information for SOFC design and *V(i)* modeling.

4.1 Description of Experiment

The anode supported $Ba(Ce_{0.8}Y_{0.2})O_{3-\delta}$ SOFCs were fabricated and tested as described in Chapter 3. For the purpose of tortuosity investigation, different anode thicknesses 1.85, 1.50, 1.34 and 1.00 mm were made and tested under different H_2 partial pressures. The porosity of the supporting anode was determined by the method described in Chapter 3 and was found to be 34%. The average pore radius is 1.41 μm, which was quantitatively determined from SEM images. The saturation current densities of different anode thickness cells under H_2 partial pressures less than 30% for 700 and 800 ^{o}C are listed in Table 4.1.1. Basically, the saturation current density increases as anode thickness decreases. This decreasing of saturation current density is mainly due to the longer diffusion path when the thickness of the anode increases, which results in lower H_2 concentration at the anode-electrolyte interface.

Table 4.1.1 List of saturation current densities for different anode thicknesses which were tested under different H_2 partial pressures at (a) 800 ^oC and (b) 700 ^oC.

(a) p_{H_2}	i_{as} (A/cm^2) Anode 1.84 mm	i_{as}(A/cm^2) Anode 1.50 mm	i_{as}(A/cm^2) Anode 1.34 mm	i_{as}(A/cm^2) Anode 1.00 mm
10%	0.506	0.522	0.709	0.854
15%	0.782	0.816	0.955	1.174
20%	1.055	1.091	1.193	1.410
30%	1.489	1.537	1.493	1.686

(b) p_{H_2}	i_{as} (A/cm^2) Anode 1.84 mm	i_{as}(A/cm^2) Anode 1.50 mm	i_{as}(A/cm^2) Anode 1.34 mm	i_{as}(A/cm^2) Anode 1.00 mm
10%	0.543	0.517	0.619	0.757
15%	0.721	0.782	0.802	1.058
20%	0.846	1.015	0.950	1.294
30%	1.005	1.338	1.117	1.590

4.2 Dusty-Gas Model for Gas Flow in Pores

The multi-gas diffusion process in pore structure is generally described by the dusty-gas model, which includes the Stefan-Maxwell equation and Knudsen terms. The equation in molar units is

$$\frac{N_i}{D_{Ki}} + \sum_{j \neq i} \frac{X_j N_i - X_i N_j}{D_{ij}} = -\frac{1}{RT} \frac{\partial (P X_i)}{\partial x}, \qquad (4.2.1)$$

where N_i and N_j are molar fluxes of components *i* and *j* (mol·cm^{-2}·s^{-1}), respectively, D_{Ki} and D_{ij} are the Knudsen diffusion coefficient for component *i* and the binary diffusion coefficient for components *i* and *j*, respectively, X_i and X_j are the fractional molar concentration of components *i* and *j*, *P* is the total pressure, *R* is the gas constant, and *T* is

the absolute temperature. It is important to clarify that *x* is the coordinate along a typical gas diffusion path, not across the anode. Therefore, the total diffusion path length is τw, the product of the tortuosity and the anode thickness.

The Knudsen diffusion coefficient considers the collisions between gas molecules and the wall. The equation for the Knudsen diffusion coefficient from the kinetic theory of gases is

$$D_{Ki} = \frac{2}{3}\left(\frac{8RT}{\pi M_i}\right)^{1/2} \bar{r}\,, \tag{4.2.2}$$

where $\bar{r}$ is the mean pore radius and M_i is the molecular molar mass of the diffusing gas. In the present experiments, the mean pore radius of the supporting anodes estimated from SEM micrographs was ~1.41 μm. The calculated Knudsen diffusion coefficients for H_2, N_2 and H_2O at 700 and 800 ^{o}C are listed in Table 4.2.1 (a).

The binary diffusion coefficient, D_{ij}, is calculated using the Chapman-Enskog equation from Cussler [58]

$$D_{ij} = \frac{1.86\times10^{-3}T^{2/3}\left(\frac{1}{M_i}+\frac{1}{M_j}\right)^{1/2}}{P\Omega\sigma_{ij}^2}\,, \tag{4.2.3}$$

where Ω is a dimensionless collision integral, based on the Lennard-Jones potential, σ_{ij} is the average collision diameter of molecules *i* and *j* (in Å), M_i and M_j are molecular weights of diffusion gases *i* and *j*, respectively, and *P* the total pressure (in atm). Using

Tables 2.2 and 2.3 in Cussler for Ω and σ_{ij} and total pressure P=1 atm , the calculated D_{ij} for various gases at temperature 700 and 800 ^{o}C are listed in Table 4.2.1 (b).

It is more convenient for us to work with molecular units. To convert Eq. (4.2.1) to molecular units, we use $P=nkT$, where n is the total number of gas molecules per unit volume, at the right side of Eq. (4.2.1). The gas constant R has moles in the denominator, so putting N_A in the numerator changes R to k. Since $nX_i = n_i$ and kT factors cancel, the right side of Eq. (4.2.1) is $-N_A \partial n_i / \partial x$. The N_i are converted to J_i molecules per unit area and time by multiplying by Avogadro's number N_A. D_{ij} has the total concentration n in its denominator, but since D_{ij} itself is in the denominator in Eq. (4.2.1), n appears in the numerator in that term, and n multiplied by X_i or X_j changes them to n_i or n_j. N_A cancels on both sides and Eq. (4.2.1) converts to

$$\frac{J_i}{D_{Ki}} + \frac{\left(J_i n_j - J_j n_i\right) kT}{D_{ij1} P_1} = -\frac{\partial n_i}{\partial x}. \qquad (4.2.4)$$

Here, D_{ij1} is the binary diffusion coefficient at $P_1 \equiv 1$ atm, and the nkT-type terms in the numerator divided by P_1 convert D_{ij1} to D_{ij} at the actual total pressure at any position x along the anode pore.

Table 4.2.1 Calculated (a) Knudsen and (b) binary diffusion coefficients for various gases at 700 and 800 ^{o}C.

(a) D_{Ki} $(cm^2/\sec)$	H_2	N_2	H_2O
$\bar{r} = 1.41\ \mu m$ at 800 ^{o}C	31.68	8.47	10.56
700 ^{o}C	30.17	8.06	10.06

(b) D_{ij1} $(cm^2/\sec)$	H_2-N_2	H_2-H_2O	N_2-H_2O
700 ^{o}C	5.35	6.65	1.87
800 ^{o}C	6.10	7.70	2.21

4.3 Calculation for Gas Input

The experiments were performed on flow of H_2/N_2 gas mixtures in the anode of $Ba(Ce_{0.8}Y_{0.2})O_{3-\delta}$ anode-supported SOFCs. The H_2/N_2 gas mixture picked up H_2O (steam) through a water bubbler so that it is a ternary system, or a binary system when 100% H_2 was used. The flow density of H_2 is $J_{H_2} = i\tau/\phi q$, where i is the current density (A cm^{-2} = C cm^{-2} s^{-1}) in the solid electrolyte and q is the charge (3.2×10^{-19} C molecule^{-1}) carried per H_2 molecule annihilated in the reaction at the anode/electrolyte interface.

The τ/ϕ factor is an enhancement factor by which the flow density J_{H_2} is enhanced compared to its value if the anode were completely porous (i.e. $\phi = \tau = 1$). To derive this result, note that this enhancement factor for an anode of area S with N_{pa} pores each of cross-sectional area A_x is $S / N_{pa} A_x$. The porosity ϕ is the total pore volume

$N_{pa}A_x\tau w$ divided by the anode volume Sw, so $\phi = N_{pa}A_x\tau / S$. By rearranging this equation we find that the enhancement factor $S / N_{pa}A_x$ is τ / ϕ.

Eq. (4.2.4) can then be written as

$$\frac{\partial n_{H_2}}{\partial x} = -(\frac{i\tau}{\phi q})(\frac{1}{D_{K,H_2}} + \frac{n_{N_2}kT}{D_{H_2,N_2,1}P_1} + \frac{n_{H_2}kT}{D_{H_2,H_2O,1}P_1}), \tag{4.3.1a}$$

$$\frac{\partial n_{N_2}}{\partial x} = \frac{i\tau}{\phi q}\frac{n_{N_2}kT}{D_{N_2,H_2,1}P_1}, \text{ and} \tag{4.3.1b}$$

$$\frac{\partial n_{H_2O}}{\partial x} = \frac{i\tau}{\phi q}\frac{n_{H_2O}kT}{D_{H_2,H_2O,1}P_1}. \tag{4.3.1c}$$

Adding Eq. (4.3.1a), (4.3.1b) and (4.3.1c) yields the equation for total concentration n and its solution

$$\frac{\partial n}{\partial x} = -(\frac{i\tau}{\phi q}\frac{1}{D_{K,H_2}}), \text{ and } \quad n = n_{total,p} - \frac{i\tau x}{\phi q D_{K,H_2}} \equiv n_{total,p} - c_{H_2}\tau^2, \tag{4.3.2}$$

where $n_{total,p}$ is the total gas concentration in the plenum and $x = w\tau$ is used in the equation. From the ideal gas law, $P=nkT$, we see that the total pressure P decreases linearly with x from the anode-plenum interface to the solid electrolyte.

We can solve Eq. (4.3.1) for n_{H_2}, n_{N_2} and n_{H_2O}

$$n_{N_2} = n_{N_2,p} \exp(\frac{i\tau x}{n_1 \phi q D_{H_2,N_2,1}}) \equiv n_{N_2,p} \exp(c_{N_2}\tau^2), \tag{4.3.3a}$$

$$n_{H_2O} = n_{H_2O,p} \exp(\frac{i\tau x}{n_1 \phi q D_{H_2,H_2O,1}}) \equiv n_{H_2,p} \exp(c_{H_2O}\tau^2), \text{ and} \tag{4.3.3b}$$

$$n_{H_2} = n_{H_2,p} - c_{H_2}\tau^2 - n_{N_2,p}(\exp(c_{N_2}\tau^2) - 1) - n_{H_2O,p}(\exp(c_{H_2O}\tau^2) - 1), \tag{4.3.3c}$$

where $n_{N_2,p}$, $n_{H_2O,p}$ and $n_{H_2,p}$ are concentrations for N_2, H_2O and H_2 in the plenum, respectively, n_1 is the total gas concentration in the plenum when P = 1 atm = 1.015×10^5 Nm^{-2}, $n_1 = P_1 / kT$ and $n_1 = 7.559\times10^{18}$ cm^{-3} for T = 973 K and $n_1 = 6.855\times10^{18}$ cm^{-3} for T = 1073 K. We see that n_{N_2} and n_{H_2O} increase exponentially along the pore from plenum to electrolyte.

If the cell current density is saturated by concentration polarization at the anode, designated as i_{as}, then i become i_{as} in the "constants" c_{H_2}, c_{N_2} and c_{H_2O}, which are really linear functions of position x/τ across the anode. For $x/\tau = w$ (the anode thickness) at the anode-electrolyte interface, they really become constants and are designated $c_{H_2,as}$, $c_{N_2,as}$ and $c_{H_2O,as}$ for the saturated condition. To find n_{H_2} at the anode-electrolyte interface, we need to apply the coefficient *a,* which describes the forward attempt current density, i.e. for the reaction $H_2 \rightarrow 2H^+ + 2e^-$, in our *V(i)* model. The details of finding coefficient *a* will be discussed in Chapter 5.

The saturation current density i_{as} is defined as the current density at which *V* drops to zero under concentration polarization. Our *V(i)* model under some conditions does predict that voltage drops extremely rapidly toward $-\infty$ as *i* goes through i_{as}. However, we only experimentially observe this behavior on O-SOFCs but not on H-SOFCs, as described in Chapter 3, Fig. 3.2.9. Due to the fact that *a* was obtained from the modeling of impinging rate of H_2 onto the triple phase boundary (TPB), the amount of n_{H_2} present at the anode-electrolyte interface determines the saturation current density when *V* goes to zero. Therefore, we took the current density as i_{as} when the voltage drops to zero in the *I-V* curve measurements.

Our *V(i)* model gives the relation between *a* and n_{H_2}, allowing us to find the n_{H_2} value $n_{H_2,as}$ attained at the anode saturation condition where $a = i_{as}$. This relation is

$$a \equiv \frac{1}{2} n_{H_2} \left(\frac{kT}{m_{H_2}}\right)^{1/2} f_a q (1-\nu_{ele})(1-a_{ele}^3 n_{H,ele}/3)^2 , \qquad (4.3.4)$$

where m_{H_2} is the H_2 molecule mass, and $(kT/m_{H_2})^{1/2}$ is the H_2 molecule average velocity component (through the anode pore) directed toward the TPB. $(1-\nu_{ele})(1-a_{ele}^3 n_{H,ele}/3)^2$ is the probability that an O^{2-} ion without a proton attached to it is at the anode TPB so that the H_2 dissociation reaction can occur, and f_a is the probability that the H_2 molecule strikes the electrolyte at an anode TPB. By setting $n_{H_2} = n_{H_2,as}$ under the anode saturation condition, Eq. (4.3.3c) can be rewritten as

$$n_{H_2,p,as} - c_{H_2,as}\tau^2 - n_{N_2,p,as}(\exp(c_{N_2,as}\tau^2) - 1) - n_{H_2O,p,as}(\exp(c_{H_2O,as}\tau^2) - 1) - n_{H_2,as} = 0\,. \quad (4.3.5)$$

All constants in Eq. (4.3.5) are positive and can be solved numerically for τ.

The constants in Eq. (4.3.5) have been defined except for the boundary conditions $n_{H_2,p,as}$, $n_{N_2,p,as}$ and $n_{H_2O,p,as}$ for gas concentrations in the plenum at the outer anode surface and $n_{H_2,as}$ for the H_2 concentration at the anode-electrolyte interface. To find $n_{H_2,p,as}$ we consider the total flow in and out of the anode plenum. For all the experiments, the total gas inflow rate before going through the water bubbler is 200 mL min^{-1}. The total metered inflow rate of 200 mL min^{-1} at temperature 21 ^oC and at Bozeman atmosphere (4900 ft. above sea level, $P_{Bozeman}$ = 8.534×10^4 N m^{-2}) is, from the ideal gas law,

$$P_{Bozeman}\frac{dV_{in}}{dt} = kT_{in}\frac{dN_{in}}{dt}, \quad \text{so } \frac{dN_{in}}{dt} \equiv j_1 = 7.012\times10^{19} \text{ molec s}^{-1}. \quad (4.3.6)$$

The metered inflow H_2 is found by multiplying the total metered inflow rate by the partial pressure fraction, and N_2 is the balance of the total inflow. Because H_2O is obtained by flowing the inflow gas through a water bubbler, the flow rate of H_2O is the inflow rate multiplied by saturated water partial pressure at room temperature (~3%). For example, a 20% H_2 input gas flow has metered flow rates: $j_{H_2,m} = p_{H_2} j_1 = 1.404\times10^{19}\, s^{-1}$, $j_{N_2,m} = p_{N_2} j_1 = 5.618\times10^{19}\ s^{-1}$ and $j_{H_2O,m} = p_{H_2O,sat.} j_1 = 2.107\times10^{18}\, s^{-1}$.

To find the net flow of each gas into the plenum, we must consider the fuel gas, H_2, outflow into the anode. The inflow rate of H_2 into anode is $j_{H_2} = -iS/q$, where S is

the active area and q = 3.2×10^{-19} C. When the cell is running at saturation current, the inflow rate into the anode is designated as $j_{H_2,as}$. To summarize the analysis for net inflows into the plenum,

$$j_{H_2,net} = p_{H_2} j_1 - \frac{iS}{q}, \quad j_{N_2,net} = p_{N_2} j_1 ,$$
$$j_{H_2O,net} = p_{H_2O,sat.} j_1 \quad \text{and} \quad j_{total,net} = j_{H_2,net} + j_{N_2,net} + j_{H_2O,net} . \qquad (4.3.7)$$

Our test system is open to space and we assume that the gases in the plenum are well mixed and have the same mole fraction everywhere. Accordingly, in the plenum the gas concentrations under anode saturation conditions are

$$n_{total,p} = \frac{P_{Bozeman}}{kT}, \quad n_{H_2 p,as} = \left(\frac{j_{H_2,net,as}}{j_{total,net,as}}\right) n_{total,p} ,$$
$$n_{N_2,p,as} = \left(\frac{j_{N_2,net}}{j_{total,net,as}}\right) n_{total,p} \quad \text{and} \quad n_{H_2O,p,as} = \left(\frac{j_{H_2O,net}}{j_{total,net,as}}\right) n_{total,p} . \qquad (4.3.8)$$

The remaining parameter to determine is $n_{H_2,as}$, the H_2 concentration at the anode-electrolyte interface under the anode saturation condition. From Eq. (4.3.4), n_{H_2} remains proportional to *a* as *i* changes, because we assume the other parameters are independent of *i*. For open circuit (*i* = 0) conditions, n_{H_2} at the interface equals $n_{H_2,0} = p_{H_2} n_{total,p}$. This known value for open-circuit n_{H_2} inserted into Eq. (4.3.4) provides a known value $a_0 = p_{H_2} a_{01}$ for the open-circuit value of *a*, where a_{01} is the open-circuit value for $p_{H_2} = 1$. For the anode saturation condition, $a = i_{as}$, and because n_{H_2} is proportional to *a*, we have

$$n_{H_2,as} = \frac{n_{H_2 0} a_{as}}{a_0} = \frac{p_{H_2} n_{total,p} i_{as}}{p_{H_2} a_{01}} = \frac{n_{total,p} i_{as}}{a_{01}}. \qquad (4.3.9)$$

Inserting the $n_{H_2,as}$ value and the $n_{H_2,p,as}$ value into Eq. (4.3.5) yields the following equation for τ^2 in terms of known parameters

$$(\frac{j_{H_2,net,as}}{j_{total,net,as}}) n_{total,p} - c_{H_2,as}\tau^2 - n_{N_2,p,as}(\exp(c_{N_2,as}\tau^2) - 1) - n_{H_2O,p,as}(\exp(c_{H_2O,as}\tau^2) - 1) - \frac{n_{total,p} i_{as}}{a_{01}} = 0. \qquad (4.3.10)$$

4.4 Results and Discussion

Figure 4.4.1 shows the results from our tortuosity calculation and the electrochemical performances of a BCY82 anode-supported SOFC with an anode

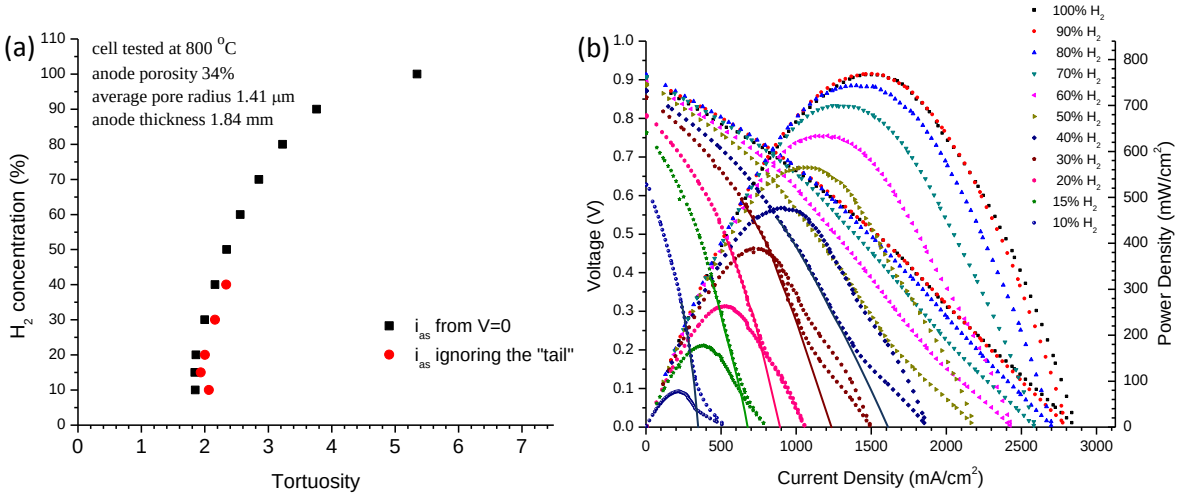

Figure 4.4.1 BCY82 anode supported SOFC (a) calculated tortuosities for its anode and (b) the electrochemical performance at 800 °C under different H_2 partial pressures.

thickness 1.84 mm and porosity 34%. The cell was tested at 800 ^{o}C under different H_2 partial pressures. The tortuosity results range from 5.35 to 1.85, but are limited to a value around 1.85 when H_2 concentrations are below 20 %. As shown on Fig. 4.4.1 (b), the cell performances did not encounter serious concentration polarization at H_2 partial pressure above 50%. The main loss was from ohmic polarization, so that the calculated tortuosity using i_{as} at voltage drop to zero should not be considered for H_2 partial pressure above 50%. Note that when concentration polarization is severe, the tortuosity values approach the same value. Therefore, the tortuosity calculated from lowest H_2 concentrations should be a more accurate number. Fig. 4.4.1 (a) also shows the calculated tortuosity for H_2 partial pressure under 40% when the "tail" effect is ignored, using the intersect value between solid lines and current density axis on Fig. 4.4.1 (b). The tortuosity is then increasing from ~1.85 to ~2.06 at low H_2 concentration. Based on the above results, we consider that the tortuosity for the supporting anode is 1.95 ± 0.1.

$Ba(Ce_{0.8}Y_{0.2})O_{3-\delta}$ anode-supported cells with different anode thickness, but the same porosity and pore radius, were tested and the tortuosities of their anodes were also calculated. The results are shown in Fig. 4.4.2. The tortuosities obtained from 10% H_2 concentration all fall into the same range, 1.95 ± 0.1, and are thickness independent, as they should be, for tests both at 800 and 700 ^{o}C. Compared to 700 ^{o}C, the tortuosity values approach their final value at higher H_2 concentration when cells were tested at 800 ^{o}C. This is because of the higher fuel utilization of cells at 800 ^{o}C.

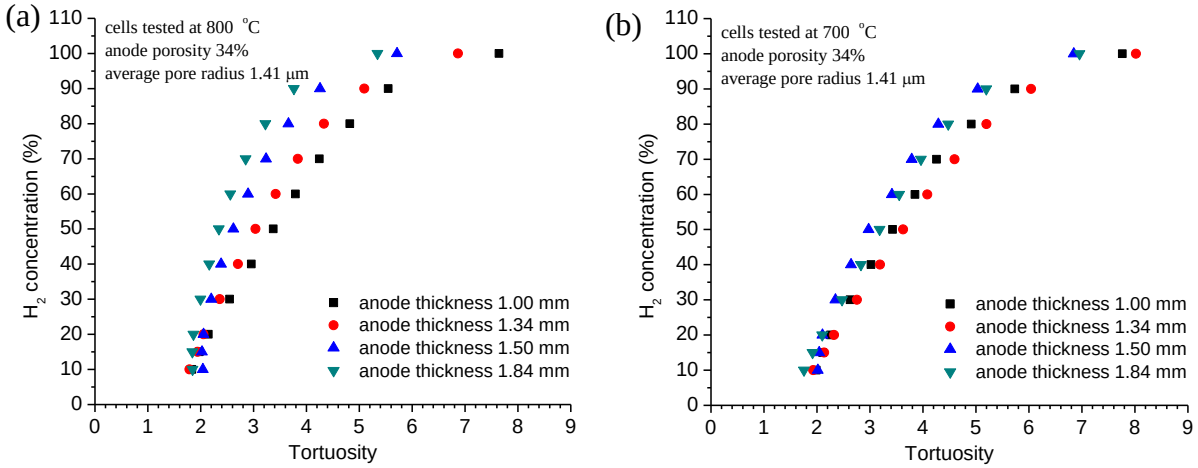

Figure 4.4.2 Calculated tortuosities for different thickness anode cells tested at (a) 800 °C and (b) 700 °C.

Comparing the result presented here, 1.95 ± 0.1, and our previous results, which were analyzed from Jiang-Virkar's experiment [59], 2.3 ± 0.6, the tortuosity value presented here is a little smaller than the previous average value but within the error [60]. This results from its bigger pore radius, 1.41 μm, when compared to Jiang-Virkar's 0.5 μm pore radius, even though our porosity is lower, 34%, compared to their 54% porosity. When looking at Jiang-Virkar's 20%H_2-80%N_2-H_2O ternary system, its saturation current i_{as} is 0.89 Acm^{-2}. The test in Fig. 4.4.1 with 20% H_2 partial pressure delivered a saturation current 1.055 Acm^{-2} or 0.877 Acm^{-2} when the "tail" is not considered. For our much lower porosity but delivering similar amount of H_2 fuel from plenum to anode-electrolyte interface, it makes sense that our tortuosity is lower, i.e. the pores are straighter from plenum-anode interface to anode-electrolyte interface. Furthermore, the bigger pore size reduces the collision rate of gas molecules with the wall, thereby

reducing the effect from Knudsen diffusion, resulting in lower tortuosity of our supporting anode.

Plots of gas concentrations across the anode for six different H_2 partial pressures under anode limiting currents at 700 ^oC are shown in Fig. 4.4.3. The total concentrations only decrease slightly because of the compensation from N_2 concentration increasing. The exponential effects on the gas concentrations appear insignificant. They appear more like linear changes, due to the relativly "thin" supporting anode. A 0.5 to 1 mm thick anode is usually used for anode-supported SOFC. However, a supporting anode thicker than 1 cm with high H_2 concentration is needed to see the exponential curvature clearly from our calculation.

4.5 Conclusions

Based on our calculation, we concluded that the tortuosity for our supporting anode is 1.95 ± 0.1. Our more accurate tests bring down the error to ±0.1 of the total value. This number is a little smaller than the average number but within the error, which we found previously from analyzing the Jiang-Virkar results, 2.3 ± 0.6 [60]. However, the lower porosity and bigger pore size of our supporting anode make it necessary to have a lower tortuosity to deliver the measured similar amount of H_2 gas from plenum to anode-electrolyte interface. The results from different tested cells prepared in the same

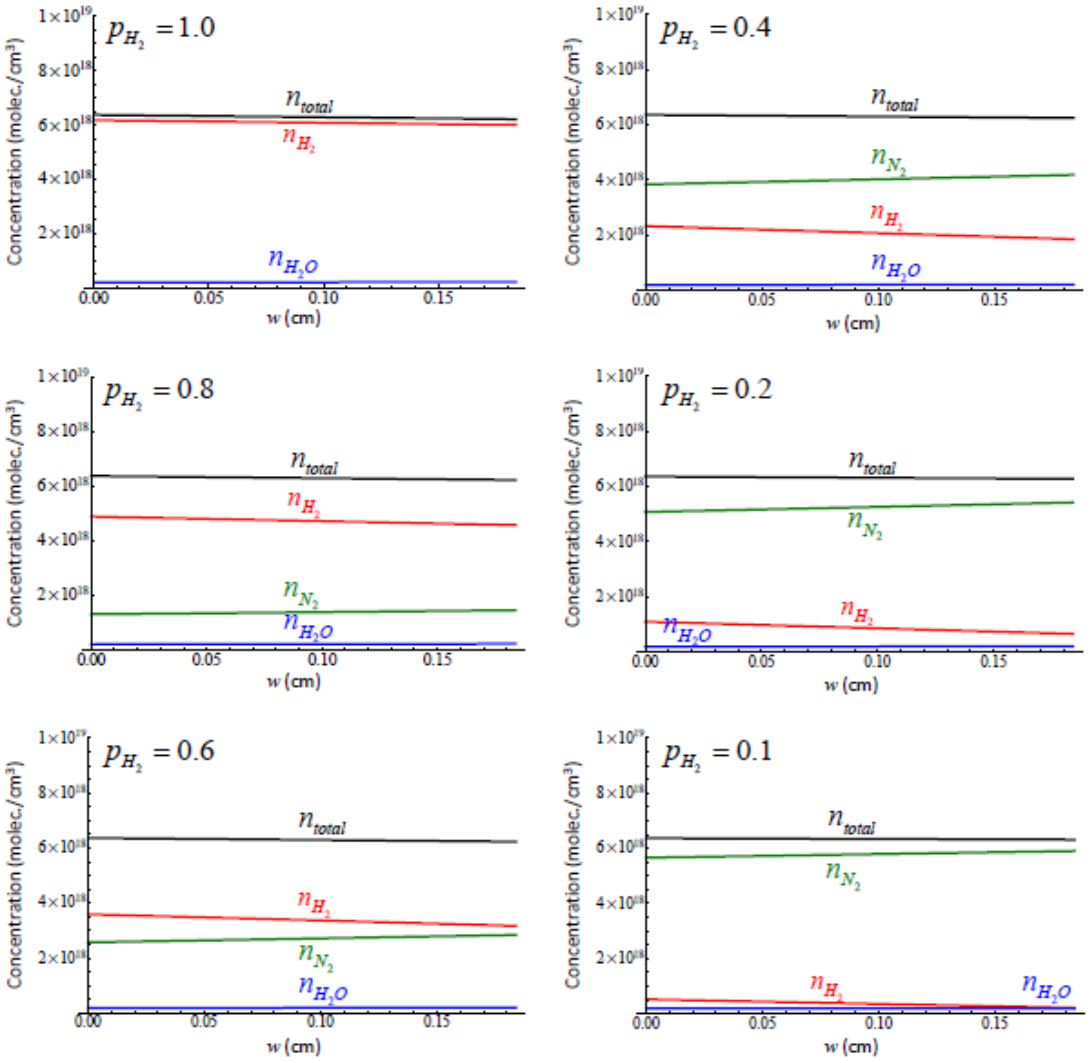

Figure 4.4.3 Plots of gas concentration *vs*. position in anode for 1.84 mm anode thickness under anode-limiting current conditions at 700 ^{o}C.

way but with different thickness all converge to the same tortuosity value range, supporting our conclusion. Our result also agrees fairly well with Williford *et al.* who found the tortuosity for modern anode material with typical porosity > 30% is in the range 2.5-3.0 [61]. Therefore, we can say that our value is in the physically reasonable

range. Knowing the pressure drops across electrodes and tortuosity as presented above provides the required tools for modeling the voltage-current density expression and gives information for new SOFC designs and for analyzing performance of existing designs in both fuel cell and electrolysis modes.

CHAPTER 5

DYNAMIC MOLECULAR-SCALE MODEL FOR PROTON CONDUCTIVE SOLID OXIDE FUEL CELL

The analysis of the I-V curve for proton conductive solid oxide fuel cells (H-SOFCs) is based on the concept of *exchange current density,* i_0. The exchange current density is defined for open-circuit operation in which the equal and opposite current densities in the system result from the equal forward and reverse reaction rates at the interface of anode-electrolyte, cathode-electrolyte and cathode-pore. Accordingly, there are three exchange current densities, one from the reactions at the anode-electrolyte interface, i_{0a}, another from the reactions at the cathode-electrolyte interface, i_{0cw}, and the third from the reactions from the cathode-pore interface, i_{0co}.

For closed-circuit operation, we continue to use the concept of forward and reverse reactions and their corresponding current densities. The net current density across the cell comes from the difference between the forward and reverse current densities, each of which is described as the product of an attempt current density and a reaction success probability.

By normalizing these reaction success probabilities, we obtain expressions for current density as a function of anode or cathode activation polarization that give us the correct saturation current density in the limit of large applied voltage in both the SOFC and SOEC mode. These expressions provide a replacement for the Butler-Volmer $V_{act}(i)$ expression, which incorrectly predicts infinite *i* for infinite applied voltage.

Our $V(i)$ expression is found by including concentration polarization $V_{conc}(i)$, which accounts for variation of gas concentrations at the anode-electrolyte, cathode-electrolyte and cathode-pore interfaces. We also include ohmic polarization $V_{ohm}(i)$, which accounts for ohmic voltage drops from transporting ions through electrolyte and electrons through electrodes. Finally, we use our H-SOFC experimental data to check the accuracy of our model.

5.1 Basics of H-SOFC Voltage Contribution

To simplify the modeling, we idealize the H-SOFC as having a solid electrolyte that is a pure proton conductor, an anode that is a pure electronic conductor and a cathode that is both an oxygen ionic and electronic conductor. The *open-circuit emf* V_0 arises at two locations, the anode-electrolyte and cathode-electrolyte interfaces. There cannot be an *emf* difference across the pore-cathode interface because the pore is an insulator. However, as discussed, there is the reaction of oxygen molecules dissociating to oxygen ions at the pore-cathode interface. For closed-circuit conditions, the three additional contributions besides V_0 to terminal voltage V are commonly called *activation polarization* V_{act}, *concentration polarization* V_{conc} and *ohmic polarization* V_{ohm}. These three are taken as positive in the SOFC mode. They become negative in the solid oxide electrolysis cell (SOEC) mode for which i flows in the opposite direction. Then in both the SOFC and SOEC modes, the terminal voltage is given by

$$V = V_0 - V_{act} - V_{conc} - V_{ohm} \,. \tag{5.1.1}$$

In the SOFC mode, V is output voltage, while in the SOEC mode, V is applied voltage.

For the open-circuit case, at all three interfaces the forward reaction rates are balanced by the reverse reaction rates. There is an *equivalent current density* for each reaction, which is the product of an *attempt current density* and a *success probability*. For closed-circuit operation, even if the gas concentrations at the interfaces remain unchanged, the forward and reverse reaction rates must become imbalanced to allow net current to flow. This imbalance is achieved by altering the success probability by means of changing the potential step at each interface. This change in potential step is called the *activation polarization* for each interface. The additional change in potential step if gas concentrations at the interface alter when current flows is called the *concentration polarization* for that interface. Finally, the *ohmic polarization* is the ohmic voltage drop due to the transfer of ions across the electrolyte and electrons across the anode and cathode. The drop is mainly distributed across the electrolyte, with weaker drops across the anode and cathode.

5.2 Model for Reactions and their Equivalent Current Density Contributions

The reactions at the anode-electrolyte and cathode-electrolyte interfaces are assumed to occur directly at the *triple phase boundary* (TPB) sites, located on lines where pore, electrolyte and electrode meet. The oxygen dissociation reaction takes place on the surface where pore and cathode material meet. The H-SOFC with H_2 fuel, and O_2 oxidizer has three reversible reactions directly involed with SOFC operation, two of

which include electron transfer. A "water shift reaction", which does not include electron transfer, uses the steam produced in the SOFC mode to provide protons for the proton conduction mechanism, Fig 5.2.1.

If the steam partial pressure is different at the anode and cathode TPBs, under open-circuit operation the only effective reaction would be the water shift reaction. This reaction reversibly converts steam at the anode and cathode TPBs into protons and oxygen ions in the solid electrolyte because there is no net charge transfer required. If we consider the TPB at the cathode-electrolyte interface having higher steam concentration than that at the anode-electrolyte interface, there will be an effective steam transfer through the electrolyte by the water shift reaction from the cathode to anode. This transfer requires concentration gradients of protons and oxygen ion vacancies. For local charge neutrality, the oxygen ion vacancy concentration increases at half the rate of the proton concentration decrease when going across the electrolyte from cathode to anode. This requires the sum of proton and oxygen ion vacancy current densities to be zero. Generally, the diffusion coefficients of protons and oxygen ion vacancies should be different. This difference will cause the carriers to set up equal and opposite surface charge density sheets at the two electrolyte surfaces, which cause a uniform field in the electrolyte to equalize the two current density magnitudes.

For our SOFC modeling, we consider the water shift reaction as a reaction independent of the SOFC reactions even though it does consume protons and oxygen ions from the electrolyte. Other than this water shift reaction, we propose a two-step cathode

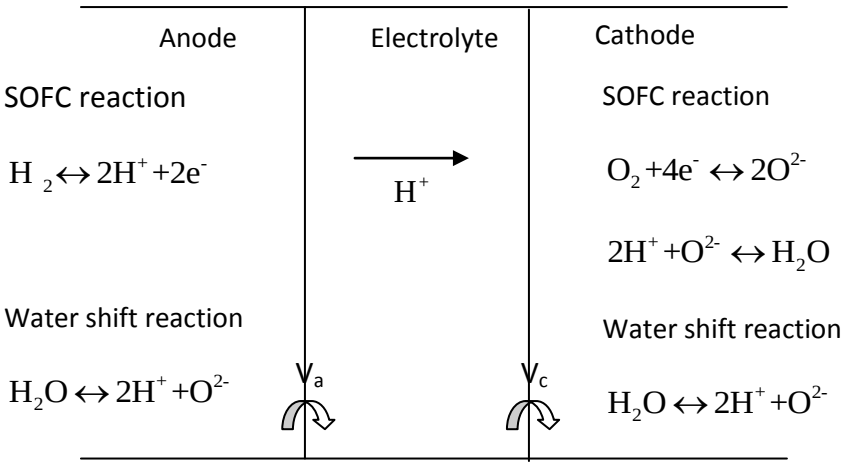

Figure 5.2.1 Electrochemical reactions for an H-SOFC.

reaction mechanism, which is different from the work of Ni *et al*. on H-SOFCs, who assume a one-step reaction at the cathode [62-64]. For a one-step cathode reaction, an O_2 molecule is required to react with 4 protons and 4 electrons at a cathode TPB site to form 2 H_2O molecules. However, the concentration of protons in the electrolyte is low (< 20%), so the probability of four protons simultaneously being within reaction distance is too low to provide the dominant reaction mechanism. In our two-step reaction proposal, the first step is

$$O_2 + 4e^- \leftrightarrow 2O^{2-} . \tag{5.2.1}$$

This reaction does not need to be on a TPB; it can occur anywhere on the cathode-pore interface since the cathode material is both an electronic and oxygen ionic conductor. The unknown for this equation is set as the concentration of O^{2-} ion vacancies v_c in the cathode. The other reaction at the cathode is

$$2H^+ + O^{2-} \leftrightarrow H_2O. \tag{5.2.2}$$

We assume that the electrolyte is a pure proton conductor, so this reaction must occur at the cathode-electrolyte TPB.

5.2.1 Reaction at Anode Side

We first model the reaction at the anode-electrolyte interface. The reaction is

$$H_2 \leftrightarrow 2H^+ + 2e^-. \tag{5.2.3}$$

Consider a line of oxygen ion sites in the electrolyte along a TPB line. We assume *oxygen vacancy probability* v_{ele} that the O^{2-} site is vacant in the electrolyte, and so $1-v_{ele}$ is the probability that the O^{2-} site is occupied. We designate ν_{af} as the ***a**node **f**orward reaction rate*, the probability per unit time that the forward reaction in Eq. (5.2.3) will occur at each occupied site. Similarly, we designate ν_{ar} as ***a**node **r**everse reaction rate.*

One factor in ν_{af} is the *attempt rate*, the probability per unit time $\nu_{af\,0}$ that an H_2 molecule will strike a given occupied O^{2-} site and attempt to cause a reaction. Another factor is *success probability* that the forward reaction of Eq. (5.2.2) will occur when the H_2 molecule strikes the O^{2-} site. If two electrons of combined charge magnitude q travel across the potential difference V_a between anode and electrolyte, this reaction will release heat U_a when the reaction occurs. Thus the net energy required for the reaction to occur is $qV_a - U_a$. If the reaction does not occur, the H_2 molecule bounces back into the anode pore.

Accordingly, the attempt rate is for a collision event that may or may not lead to a reaction. Assume the probability of either reaction or no reaction can be described by classical (Boltzmann) statistics. The un-normalized probability for the reaction event is $\exp[-(qV_a - U_a)/kT]$ and for no reaction event is 1. Normalizing, and multiplying by ν_{af0} , we obtain reaction rate per O^{2-} site

$$\nu_{af} = \nu_{af0} \exp[-(qV_a - U_a)/2kT]/2\cosh[(qV_a - U_a)/2kT]. \qquad (5.2.4)$$

A similar expression, but with opposite sign for the argument of the exponential, holds for the reverse reaction based on recombining the protons in the electrolyte to form H_2 molecules

$$\nu_{ar} = \nu_{ar0} \exp[(qV_a - U_a)/2kT]/2\cosh[(qV_a - U_a)/2kT]. \qquad (5.2.5)$$

To find ν_{af0}, we consider an H_2 fuel gas concentration of n_{H_2} at the anode-electrolyte interface. Half of these H_2 molecules travel toward the surface with mean normal velocity component $< u_y >$. Then the flux of H_2 molecules onto the surface will be $\frac{1}{2} n_{H_2} < u_y >$. We know $\frac{1}{2} kT = \frac{1}{2} m_{H_2} < u_y^2 >$, so then $< u_y >= (kT / m_{H_2})^{1/2}$, where m_{H_2} is the mass of the H_2 molecule. Thus, the flux is $\frac{1}{2} n_{H_2} (kT / m_{H_2})^{1/2}$. The perovskite structure (ABO_3) has three O^{2-} sites in each unit cell. Accordingly, we take the 2/3 power of the volume density, namely $(3/a_{ele}^3)^{2/3} = 3^{2/3}/a_{ele}^2$, where a_{ele} is the perovskite lattice constant, 0.4445 nm for $Ba(Ce_{0.8}Y_{0.2})O_{3-\delta}$ (BCY82), as the surface density of O^{2-}

sites for electrolyte material. Then, the O^{2-} site has area $a_{ele}^2 / 3^{2/3}$ m^2 and the impingement rate per O^{2-} site is

$$\nu_{af\,0} = \frac{1}{2} n_{H_2} \left(\frac{kT}{m_{H_2}}\right)^{1/2} \left(\frac{a_{ele}^2}{3^{2/3}}\right). \tag{5.2.6}$$

We make the approximation that the oxygen reaction site areas cover the whole electrolyte material surface but do not overlap, so that the number of sites per m^2 is $3^{2/3} / a_{ele}^2$. Only a fraction f_a, to be estimated later, of oxygen sites sit on the TPB and are available for the reactions at the anode-electrolyte interface.

To further analyze the reaction of Eq. (5.2.3), we need to make assumptions about the nature of protonic conductivity in the perovskite structure. Two clues come from the two Pauling ice rules. One rule is that there should be one and only one proton in each possible H-bond, where possible H-bond means a pair of nearest-neighbor oxygens. This rule holds for most H-bonded crystals but certainly not for perovskites because there are way too few protons to fill the possible H-bonds.

The second rule is that there are two protons close to a given oxygen, and two farther away, in the four asymmetric H-bonds radiating out from that oxygen. This rule is specific to the ice structure, though it also applies to KH_2PO_4 if "phosphate" is substituted for "oxygen" in the rule. This rule is based on valence; the O^{2-} wants two nearby H^+ for charge balance.

In the perovskite structure each oxygen ion has eight nearest oxygen ion neighbors, but Pauling's second rule certainly doesn't mean that there should be four

close protons in eight filled H-bonds. From the valence point of view, in a pure perovskite structure such as $BaCeO_3$, there should be NO protons because charge neutrality is already satisfied. For our compositions, with Y^{3+} replacing some Ce^{4+} or Zr^{4+} ions, an oxygen with a Y^{3+} neighbor should welcome one close proton, but not more.

In H-bonded crystals, the conduction mechanism consists of two types of proton jumps, both of which are necessary for dc conductivity. One is a jump from one side to the other side of the asymmetric H-bond. The other is a jump from one H-bond to another, but the bond it jumps to must be originally empty. In a pure crystal, if the bond is empty it is because its proton jumped to a higher-energy interstitial position. In a doped crystal, such as KH_2PO_4 doped with SO_4^{2-} ions, there should be proton vacancies because of the lower sulfate valence compared to phosphate. Indeed, it was found that sulfate doping increases the conductivity by an order of magnitude [65]. In our perovskite ceramics, there is no problem for a proton to find a neighboring vacant H-bond. The problem rather is to get enough protons into the sample to obtain a high enough conductivity.

We assume each oxygen ion in the electrolyte can take two protons at a time, one close and one farther in its two filled H-bonds. We need an oxygen ion, which has no protons attached to it, for the dissociation of the H_2 molecule to occur. The probability that an O^{2-} site is occupied by an oxygen ion is $1-v_{ele}$. In the perovskite structure, each oxygen ion has a volume $a_{ele}^3/3$ associated with its unit cell. If the proton concentration in the electrolyte is $n_{H,ele}$, then per oxygen site the probability of an O^{2-} ion

with a proton attached to it is $(1-v_{ele})(a_{ele}^3 n_{H,ele}/3)$ and $(1-v_{ele})(1-a_{ele}^3 n_{H,ele}/3)$ for an O^{2-} ion without a proton attached to it. The current densities are related by a factor q to the gas flow densities resulting in reaction. By defining $\alpha \equiv (U_a - qV_a)/2kT$ and putting all the factors together, we obtain

$$i_{af} = \frac{1}{2} n_{H_2} (\frac{kT}{m_{H_2}})^{1/2} (\frac{a_{ele}^2}{3^{2/3}}) \times f_a \times (\frac{3^{2/3}}{a_{ele}^2}) \times (1-v_{ele})[1-(a_{ele}^3 n_{H,ele}/3)] \times q \times e^{\alpha}/2\cosh\alpha$$

$$= \frac{1}{2} n_{H_2} (\frac{kT}{m_{H_2}})^{1/2} f_a q (1-v_{ele})[1-(a_{ele}^3 n_{H,ele}/3)] e^{\alpha}/2\cosh\alpha$$

$$= a e^{\alpha}/2\cosh\alpha, \qquad \text{where } a \equiv \frac{1}{2} n_{H_2} (\frac{kT}{m_{H_2}})^{1/2} f_a q (1-v_{ele})[1-(a_{ele}^3 n_{H,ele}/3)]. \qquad (5.2.7)$$

For the reverse reaction to be possible, there must be two close protons in the electrolyte in the volume for one oxygen ion, which has a probability $a_{ele}^6 n_{H,ele}^2/9$. Therefore, the density of oxygen ions with two protons attached to them is

$$\frac{3^{2/3}(1-v_{ele})}{a_{ele}^2} \times \frac{a_{ele}^6 n_{H,ele}^2}{9} = 3^{2/3}(1-v_{ele}) a_{ele}^4 n_{H,ele}^2/9. \qquad (5.2.8)$$

We consider a given reaction attempt is the probability that the reaction occurs during a single typical lattice vibration period. Accordingly, we use $\upsilon = 10^{13}/\text{sec}$ as an approximation for the attempt frequency, which limits the reaction attempt rate. This reverse reaction is also located on the TPB lines, so

$$i_{ar} = (3^{2/3}(1-v_{ele})a_{ele}^4 n_{H,ele}^2 / 9) f_a \upsilon q e^{-\alpha} / 2\cosh\alpha$$

$$= be^{-\alpha} / 2\cosh\alpha, \qquad \text{where } b \equiv 3^{2/3}(1-v_{ele})a_{ele}^4 n_{H,ele}^2 f_a \upsilon q / 9 . \tag{5.2.9}$$

Here *a* and *b* are the anode *attempt current densities*. For open-circuit values, we designate the values with subscribe 0. The forward and reverse open-circuit reaction rates are equal because $i = i_{af\,0} - i_{ar0} = 0$ in the electrolyte. The equivalent equal and opposite forward and reverse current densities in the electrolyte are designated here as i_0, the *exchange current density*. In general, i_0 has different values for the reaction at the anode-electrolyte interface , i_{0a} , the cathode-electrolyte interface, i_{0cw} and the cathode-pore interface, i_{0co}. To find exchange current density i_{0a} at the anode, we know that

$$i_{af\,0} = i_{ar0} = i_{0a} . \tag{5.2.10}$$

From Eqs. (5.2.7) and (5.2.9) for the open-circuit case, together with Eq. (5.2.10), we have

$$a_0 \exp(\alpha_0) = b_0 \exp(-\alpha_0) = 2i_{0a}\cosh(\alpha_0) . \tag{5.2.11}$$

From Eq. (5.2.11) we obtain

$$\alpha_0 \equiv \frac{1}{2}\ln(b_0/a_0) . \tag{5.2.12}$$

The subscript 0 emphasizes that for open-circuit the H_2 concentration n_{H_2} at the anode-electrolyte interface is the same as at the outside plenum and the value V_{a0} across the anode-electrolyte interface is the contribution to the open-circuit SOFC *emf* V_0.

5.2.2 Reactions at Cathode Side

Figure 5.2.2 shows the two-step process reactions at the cathode. As discussed previously, there are two reactions at the cathode side, one at the cathode-electrolyte interface and the other at the cathode-pore interface. Similar to the arguments for the reaction at the anode side, both reactions on the cathode side are treated as collision events. The current densities are described by attempt current density multiplied by success probability. Therefore, the forward and reverse current densities of Eq. (5.2.1) are

$$i_{cof} = ce^{\gamma} / 2\cosh\gamma \quad \text{and}$$

$$i_{cor} = de^{-\gamma} / 2\cosh\gamma, \quad \text{where } \gamma \equiv 2U_{co} / 2kT. \tag{5.2.13}$$

U_{co} is the heat released when the dissociation of ½ O_2 molecule happens. The 2 in front of U_{co} is due to double-size charge transfer in the reaction. In this reaction, the cathode material, which is both an oxygen ionic and electronic conductor, provides no barrier for establishing voltage across the cathode-pore interface so that no potential "hill" needs to be conquered by electrons in the forward/reverse process.

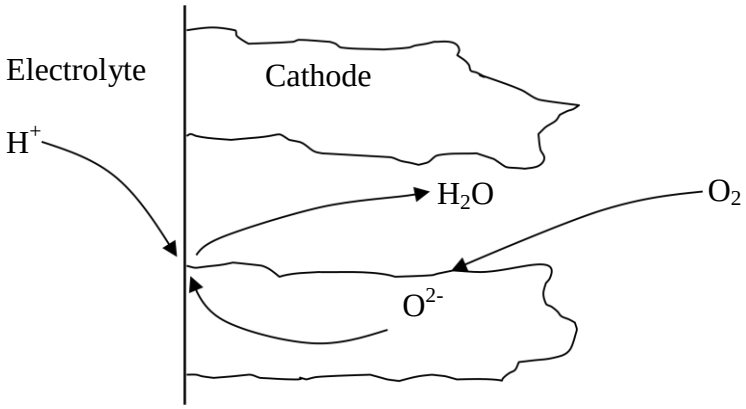

Figure 5.2.2 The two-step process reactions on cathode side.

To find the forward attempt current density *c*, we assume the oxygen concentration n_{O_2} in the cathode pore is the same as outside in the plenum since the cathode is usually very thin ($< 50\ \mu m$). Different from other reactions, the reaction in Eq. (5.2.1) can happen at any place where pore and cathode material meet because the cathode material is both an oxygen ionic and electronic conductor. We need two oxygen vacancies next to each other for the O_2 molecule dissociation process. The cathode material, $(La_{0.8}Sr_{0.2})MnO_{3-\delta}$ (LSM) in our case here, is a perovskite structure with lattice constant a_c = 0.392 nm. Therefore, the density of O^{2-} vacancies on the surface of cathode material adjacent to a pore is

$$v_c^2\left(\frac{3^{2/3}}{a_c^2}\right)(1-\phi_c), \tag{5.2.14}$$

where v_c is the oxygen vacancy probability in the cathode material and ϕ_c is the cathode porosity. We also take into account the impinging rate of O_2 molecules and transfer charge $2q$ for each reaction. The forward current density is

$$i_{cof} = \frac{1}{2} n_{O_2} (\frac{kT}{m_{O_2}})^{1/2} (\frac{a_c^2}{3^{2/3}}) \times v_c^2 (\frac{3^{2/3}}{a_c^2})(1-\phi_c) \times (2q) \times e^{\gamma} / 2\cosh\gamma$$

$$= \frac{1}{2} n_{O_2} (\frac{kT}{m_{O_2}})^{1/2} v_c^2 (1-\phi_c)(2q) e^{\gamma} / 2\cosh\gamma$$

$$= ce^{\gamma} / 2\cosh\gamma, \qquad \text{where } c \equiv \frac{1}{2} n_{O_2} (\frac{kT}{m_{O_2}})^{1/2} v_c^2 (1-\phi_c)(2q). \qquad (5.2.15)$$

The reverse attempt current density calculation requires that two O^{2-} ions sit next to each other on the cathode-pore interface. One question we may ask is whether all the O^{2-} ions are available for the reaction, which means how many O^{2-} ions one can take out freely from the structure without causing the collapse of the structure. For oxide ceramics, oxygen vacancies can be introduced by doping lower valence cations into the material. The limitation of oxygen vacancies that can be created seems to be around 10%, e.g. in the materials such as YSZ, gadolinium doped CeO_2, yttria doped $BaZrO_3$ and yttria doped $BaCeO_3$. If higher percentage dopant is introduced, the structure tends to collapse and oxygen vacancy concentration is then significantly reduced. Therefore, we assume not all the O^{2-} ions in the cathode material are available but only 10% of them are available for the reactions in the cathode material. Accordingly, this assumption also

limits the O^{2-} vacancy to 10% of the total O^{2-} ion concentration, i.e. $(0.1-v_c)$ must be positive.

The reverse reaction is also limited by attempt frequency $\upsilon = 10^{13}$/sec and each reaction transfers $2q$ of charge, so

$$i_{cor} = \frac{3^{2/3}}{a_c^2}(0.1-v_c)^2 \times (2q) \times \upsilon \times (1-\phi) \times e^{-\gamma} / 2\cosh\gamma$$

$$= \frac{3^{2/3}(2q)\upsilon(1-\phi)(0.1-v_c)^2}{a_c^2} e^{-\gamma} / 2\cosh\gamma$$

$$= de^{-\gamma} / 2\cosh\gamma, \qquad \text{where } d \equiv \frac{3^{2/3}(2q)\upsilon(1-\phi)(0.1-v_c)^2}{a_c^2}. \qquad (5.2.16)$$

For Eq. (5.2.2), $2H^+ + O^{2-} \leftrightarrow H_2O$, we have the forward and reverse current densities

$$i_{cwf} = fe^{\xi} / 2\cosh\xi \text{ and}$$

$$i_{cwr} = he^{-\xi} / 2\cosh\xi, \qquad \text{where } \xi \equiv (U_{cw} - qV_c) / 2kT. \qquad (5.2.17)$$

V_c is the potential difference across the cathode-electrolyte interface, and the reaction releases heat U_{cw} when the forward reaction occurs. Thus the net energy required for the forward reaction to occur is $qV_c - U_{cw}$. For the forward reaction of Eq. (5.2.2) to be possible, the oxygen ion from the cathode must meet with two close protons from the electrolyte at the TPB, as in a water molecule in the ice structure. The O^{2-} ion

concentration available at the TPB from the cathode is $\frac{3^{2/3}}{a_c^2}(0.1-v_c)f_c$ in which f_c is the fraction of oxygen sites on the TPB and available for reaction at the cathode-electrolyte interface. The probability of two close protons in electrolyte is $\frac{1}{9}a_{ele}^6 n_{H,ele}^2(1-v_{ele})$. Therefore, the probability of the "water molecules" along the TPB is

$$\frac{3^{2/3}a_{ele}^6 n_{H,ele}^2(1-v_{ele})(0.1-v_c)f_c}{9a_c^2}. \tag{5.2.18}$$

The corresponding current density is found by multiplying the transferred charge q, attempt frequency υ and success probability

$$i_{cwf} = \frac{3^{2/3}a_{ele}^6 n_{H,ele}^2(1-v_{ele})(0.1-v_c)f_c q\upsilon}{9a_c^2} e^{\xi}/2\cosh\xi$$

$$= fe^{\xi}/2\cosh\xi, \qquad \text{where } f \equiv \frac{3^{2/3}a_{ele}^6 n_{H,ele}^2(1-v_{ele})(0.1-v_c)f_c q\upsilon}{9a_c^2}. \tag{5.2.19}$$

To calculate the current density of the reverse reaction of Eq. (6.2.2), we assume the steam concentration on the cathode-electrolyte interface is n_{c,H_2O}. The reaction needs an oxygen ion from the electrolyte, which has no proton attached to it, $(1-v_{ele})[1-(\frac{a_{ele}^3 n_{H,ele}}{3})]$, and one O^{2-} vacancy from the cathode, v_c. The O^{2-} ion and vacancy need to be on the TPB for the reaction. We also need to consider the impinging rate of water molecules and the charge transfer per reaction. In this case

$$i_{cwr} = \frac{1}{2} n_{c,H_2O} (\frac{kT}{m_{H_2O}})^{1/2} [1 - (\frac{a_{ele}^3 n_{H,ele}}{3})](1 - v_{ele}) v_c f_c q e^{-\xi} / 2\cosh\xi \qquad (5.2.20)$$

$$= h e^{-\xi} / 2\cosh\xi , \qquad \text{where } h \equiv \frac{1}{2} n_{c,H_2O} (\frac{kT}{m_{H_2O}})^{1/2} [1 - (\frac{a_{ele}^3 n_{H,ele}}{3})](1 - v_{ele}) v_c f_c q.$$

In Eqs. (5.2.13) and (5.2.17), *c, d, f* and *h* are the attempt current densities for the reactions at the cathode.

5.3 Derivation of Current Density as a Function of Activation Polarization

To find *i* in terms of the anode activation polarization $V_{a,act}$ or cathode activation polarization $V_{c,act}$, the concentration and ohmic polarization effects need to be neglected, so we consider the situation approaching to open-circuit value. To be specific, we study the anode case and take the open-circuit attempt current densities as a_0 and b_0. We begin with $i = i_{af} - i_{ar}$ and Eq. (5.2.7) and (5.2.9) and use the relation $\alpha = \alpha_0 + \delta$, where α_0 is the open-circuit value and $\delta = qV_{a,act} / 2kT$. We have

$$i = i_{af} - i_{ar} = [a_0 \exp(\alpha_0 + \delta) - b_0 \exp(-\alpha_0 - \delta)] / 2\cosh(\alpha_0 + \delta). \qquad (5.3.1)$$

We know that $a_0 \exp(\alpha_0) = b_0 \exp(-\alpha_0)$ from Eq. (5.2.11) and $\cosh(\alpha_0 + \delta) = \cosh\alpha_0 \cosh\delta + \sinh\alpha_0 \sinh\delta$. We obtain

$$i = a_0 \exp(\alpha_0)[\exp\delta - \exp(-\delta)] / 2[\cosh\alpha_0 \cosh\delta + \sinh\alpha_0 \sinh\delta]$$

$$= a_0 \exp(\alpha_0) \tanh\delta / [\cosh\alpha_0 + \sinh\alpha_0 \tanh\delta]. \qquad (5.3.2)$$

From Eq. (5.2.11), we know that $2i_{0a} = a_0 \exp(\alpha_0) / \cosh \alpha_0$, so

$$i = 2i_{0a} \tanh \delta / [1 + \tanh \alpha_0 \tanh \delta]. \tag{5.3.3}$$

Rearranging Eqs. (5.2.7) and (5.2.9) and using $i = i_{af} - i_{ar}$,

$$i = \frac{1}{2}(a - b) + \frac{1}{2}(a + b) \tanh \alpha. \tag{5.3.4}$$

From Eqs. (5.2.11) and (5.2.12), we obtain $i_{0a} = (a_0^{-1} + b_0^{-1})^{-1}$, so that we have $\tanh(\alpha_0) = (b_0 - a_0) / (b_0 + a_0) = (a_0^{-1} - b_0^{-1}) i_{0a}$ and

$$i = 2i_{0a} \tanh \delta / [1 + (a_0^{-1} - b_0^{-1}) i_{0a} \tanh \delta]. \tag{5.3.5}$$

The Butler-Volmer equation was used in much SOFC modeling literature and the expression is [62-64, 66]

$$i = i_0 [\exp(\frac{\alpha z F V_{act}}{RT}) - \exp(-\frac{(1-\alpha) z F V_{act}}{RT})], \tag{5.3.6}$$

where z is the number of electrons involved per reaction, F is Faraday constant, 96485 $\mathrm{C \cdot mol^{-1}}$, and α is considered to be the fraction of the change in the polarization, which leads to a change in the reaction rate constant and is usually set as 0.5 for fuel cells. The $\delta \equiv qV_{a,act} / 2kT$ in our notation is equivalent to $zFV_{a,act} / RT$ in molar notation of Eq. (5.3.6). The Butler-Volmer equation in our notation is

$$i = 2i_{0a} \sinh \delta. \tag{5.3.7}$$

Comparing Eqs. (5.3.5) and (5.3.7) shows that the Butler-Volmer equation and our expression become equivalent in the limit of small V_{act}. However, the Butler-Volmer equation predicted the current density becomes $\pm\infty$ when $V_{act} \to \pm\infty$. This is incorrect because the current density eventually will be limited by the rate at which gas is supplied for the reaction.

In our expression in Eq. (5.3.5), the current density remains finite for infinite applied voltage. Specifically, in the SOFC mode, when $V_{act} \to \infty$, $\tanh\alpha \to 1$. From Eq. (5.3.4) the current density *i* reaches a_0. This value makes sense physically because a_0 corresponds to the rate at which all H_2 molecules striking on the TPB with an O^{2-} ions present dissociate into protons. In the SOEC electrolysis mode, for high negative applied voltage, current density will be limited to $i = -b_0$. This value corresponds to all protons in the electrolyte along the TPB recombining into H_2 molecules, i.e. maximum H_2 production rate when running the cell as an SOEC. These physical predictions make our expression not only valid for SOFC and SOEC modes but also provide a replacement for using the Butler-Volmer equation in SOFC modeling.

5.4 Derivation of Voltage as a Function of Current Density

To derive $V(i)$ for SOFC and SOEC, we need to include the contribution from all polarizations, i.e. $V = V_0 - V_{act} - V_{cenc} - V_{ohm}$. We first consider the anode-electrolyte interface, which contributes V_a to the terminal voltage V. Similar to Eq. (5.3.4) but considering both activation and concentration polarizations, we have

$$\tanh\alpha = (2i - a + b)/(a + b). \tag{5.4.1}$$

In general, we know that $\tanh^{-1} x = \frac{1}{2}\ln(1+x) - \frac{1}{2}\ln(1-x)$, so

$$\alpha = \frac{1}{2}\ln[(b+i)/(a-i)] = (U_a - qV_a)/2kT. \tag{5.4.2}$$

Solving Eq. (5.4.2) for V_a gives

$$V_a = U_a/q - (kT/q)\ln[(b+i)/(a-i)]. \tag{5.4.3}$$

Next, we go to the cathode-electrolyte interface. Similarly, V_c can be found from Eqs. (5.2.17), (5.2.19) and (5.2.20) as

$$\begin{aligned} V_c &= (U_{cw}/q) - (kT/q)\ln[(h+i)/(f-i)] \\ &= (U_{cw}/q) - (kT/q)\ln[(h'v_c + i)/(f'(0.1 - v_c) - i)], \end{aligned} \tag{5.4.4}$$

where $h \equiv h'v_c$ and $f \equiv f'(0.1 - v_c)$. Third, we go to the pore-cathode interface and use Eqs. (5.2.13), (5.2.15) and (5.2.16). We have

$$\gamma = \frac{1}{2}\ln[(d+i)/(c-i)] = U_{co}/kT. \tag{5.4.5}$$

By defining

$$c \equiv c'v_c^2 \quad and \quad d \equiv d'(0.1 - v_c)^2, \tag{5.4.6}$$

we can obtain

$$c'v_c^2 e^{\gamma} - d'(0.1 - v_c)^2 e^{-\gamma} = i(e^{\gamma} + e^{-\gamma}) = 2i\cosh\gamma\,. \tag{5.4.7}$$

To find the terminal voltage V, we use Eqs. (5.4.3) and (5.4.4) and obtain

$$V = (U_a + U_{cw})/q - (kT/q)\{\ln[(b+i)/(a-i)] + \ln[(h'v_c + i)/(f'(0.1 - v_c) - i)]\} - V_{ohm}$$

$$= (U_a + U_{cw})/q - (kT/q)\ln[(b+i)(h'v_c + i)/(a-i)(f'(0.1 - v_c) - i)] - V_{ohm}\,. \tag{5.4.8}$$

For open-circuit emf V_0, by using Eqs. (5.4.7) and (5.4.8) with $i = V_{ohm} = 0$, and all attempt current densities set at their open-circuit values, we have

$$0.1 - v_c = \sqrt{c_0'/d_0'}\, v_c e^{\gamma} \quad \text{and} \tag{5.4.9}$$

$$V_0 = (U_a + U_{cw})/q - (kT/q)\ln[b_0 h_0' v_c / a_0 f_0'(0.1 - v_c)]\,. \tag{5.4.10}$$

Replacing $(1 - v_c)$ in Eq. (5.4.10) by Eq. (5.4.9), we obtain

$$V_0 = (U_a + U_{cw})/q - (kT/q)\ln[\frac{b_0 h_0' \sqrt{d_0'}}{a_0 f_0' \sqrt{c_0'}} e^{-\lambda}]$$

$$= (U_a + U_{cw} + U_{co})/q - (kT/q)\ln[\frac{b_0 h_0' \sqrt{d_0'}}{a_0 f_0' \sqrt{c_0'}}]$$

$$= U/q - (kT/q)\ln[\frac{b_0 h_0' \sqrt{d_0'}}{a_0 f_0' \sqrt{c_0'}}]\,, \tag{5.4.11}$$

where $U \equiv U_a + \mathrm{U_{cw}} + \mathrm{U_{co}}$ is the heat released from combustion of hydrogen.

The activation polarization is given by

$$V_{act} = V_0 - V - V_{conc} - V_{ohm} \,. \tag{5.4.12}$$

If we run a system near open-circuit with low current density, we can set $a = a_0$, etc. in Eqs. (5.4.7) and (5.4.8), and can eliminate V_{conc}. We can solve for V_{act} numerically by inserting Eqs. (5.4.7), (5.4.8) and (5.4.11) into Eq. (5.4.12). Then, concentration polarization V_{conc} can be obtained by using $V_{conc} = V_0 - V - V_{act} - V_{ohm}$.

5.5 Comparison of Model Predictions with Experimental Results

We used our experimental results from a $Ba(Ce_{0.8}Y_{0.2})O_{3-\delta}$ anode supported SOFC, which was described in Chapter 3.2.2. The thickness of supporting anode was about 1.15 mm with a porosity ~ 44%. The average pore radius obtained quantitatively from SEM images is about 0.71 μm. Using the method described in Chapter 4, we found the tortuosity of the supporting anode is about 1.8. The effective cathode area of the cell is 0.57 cm^2.

Now we put in some particular numbers and gas concentrations to calculate all the attempt current densities and $V(i)$ for a particular H-SOFC. We keep in mind that *a, b, c, d, f* and *h* are equivalent current densities corresponding to attempt rate for forward and reverse reactions at the anode-electrolyte, pore-cathode and cathode-electrolyte interface, respectively. We know that from Eq. (5.2.7)

$$a = \frac{1}{2} n_{H_2} \left(\frac{kT}{m_{H_2}}\right)^{1/2} f_a q (1 - \nu_{ele})^2 [1 - (a_{ele}^3 n_{H,ele} / 3)]^2 \,. \tag{5.5.1}$$

The H_2 concentrations at the plenum and anode-electrolyte interface of the cell are found by using Eqs. (4.3.8) and (4.3.10). When the system is running under open-circuit voltage, the H_2 concentration at the anode-electrolyte interface is the same as that in the plenum. The mass m_{H_2} is about 3.32×10^{-27} kg. The charge q transferred per reaction of Eq. (5.2.3) is 2 electrons, i.e. 3.2×10^{-19} C.

For the proton concentration $n_{H,ele}$ in the electrolyte, we assume it is 12% of the $BaCe_{0.8}Y_{0.2}O_{3-\delta}$ (BCY20), i.e. $a_{ele}^3 n_{H,ele} = 0.12$, even though the proton uptake of $Ba(Ce_{0.8}Y_{0.2})O_{3-\delta}$ could be as high as 20%, close to the Y^{+3} concentration in $Ba(Ce_{0.8}Y_{0.2})O_{3-\delta}$ [67]. Accordingly, the O^{2-} vacancy v_{ele} in the electrolyte is 4% of the $Ba(Ce_{0.8}Y_{0.2})O_{3-\delta}$. This is because charge neutrality requires that an O^{2-} ion be added when every two protons are put into the electrolyte. Therefore, $n_{H,ele}$ can be considered as an adjustable constant in the model.

To find the fraction of oxygen sites at TPBs, f_a , we first find d_t , the TPB length per cm^2 of electrolyte surface. Here, we use tortuosity 2.4 instead of 1.8 because we found the concentration polarization effect can not be seen when $\tau = 1.8$ was used. The difference will be discussed later. The tortuosity of the supporting anode is $\tau = 2.4$ and can be modeled as resulting from each pore being straight, but inclined at an angle $\cos^{-1}(1/\tau)$. The pore then meets the electrolyte at this angle and its intersection with the electrolyte is an ellipse of semimajor axis $\tau\bar{r}$ and semiminor axis $\bar{r}$. The pore area as it impinges on the electrolyte then is $\pi\tau\bar{r}^2$. The total pore number n_p of pores impinging

per cm^2 of electrolyte is $n_p = \phi / \pi\tau\bar{r}^2 = 1.158\times10^7 / cm^2$. Each pore perimeter P_p as it impinges on the electrolyte is, according to Marks' Handbook [68]

$$P_p = \pi\bar{r}(1+\tau)[1+\tfrac{1}{4}m^2+\tfrac{1}{64}m^4+\tfrac{1}{256}m^6+.....]. \qquad (5.5.2)$$

where $m=(\tau-1)/(\tau+1)$, so $P_p = 7.909\times10^{-4}$ cm. Multiplying by n_p yields $d_t = 9.156\times10^3$ cm^{-1}. If we take the 1/3 power of O^{2-} ion volume to be the spacing between the O^{2-} ions, i.e. $(a_{ele}^3/3)^{1/3} = a_{ele}/3^{1/3}$, 0.308 nm for $Ba(Ce_{0.8}Y_{0.2})O_{3-\delta}$, then the fraction f_a of electrolyte surface consisting of TPB is 2.822×10^{-4}. In practice, when an interlayer is applied, the TPB can extend from the anode-electrolyte interface into the anode for about 10 μm, a 3-dimensional network instead of 2-dimensional surface [75]. Therefore, we use f_a=2.822×10^{-3}, ten times bigger than what we calculated, as the fraction of oxygen sites at TPBs for our modeling and consider f_a as a somewhat adjustable parameter. The difference between using $f_a = 2.822\times10^{-4}$ and $f_a = 2.822\times10^{-3}$ will be discussed later in this chapter.

If we take 100% H_2 fuel gas inflow as an example and multiply all the factors in Eq. (5.5.1), we have open-circuit forward attempt current density for Eq. (5.2.3) of

$$a_0 = 521.13\ A/cm^2. \qquad (5.5.3)$$

The reverse attempt current density is

$$b_0 = 3^{2/3}(1-v_{ele})^2 f_a a_{ele}^4 n_{H,ele}^2 \upsilon q/9 = 1.460\times10^4\ A/cm^2. \qquad (5.5.4)$$

The reverse attempt current density is a constant in our model. In reality, $n_{H,ele}$ should depends on temperature, gas concentrations at the electrolyte-electrode interface or current density *i*, but in this model it is assumed constant and results in *b* being a constant.

The equation for the oxygen dissociation process at the pore-cathode interface that provides the forward attempt current density *c* is given by

$$c_0 = \frac{1}{2} n_{O_2} \left(\frac{kT}{m_{O_2}}\right)^{1/2} v_c^2 (1-\phi_c)(2q), \tag{5.5.5}$$

where n_{O_2} is the O_2 molecule concentration, fraction of 0.21 atmosphere when air is used as oxidative gas. v_c can be obtained from Eq. (5.4.7) by setting $i = 0$. Figure 5.5.1 shows v_c for various oxygen vacancy concentrations *vs*. current density in the cathode material for different O_2 partial pressures as calculated from Eq. (5.4.7). The value of U_{co} used for the calculation is obtained from the best fit of the model to experimental data, which gives 3.0×10^{-21} Joule. Surprisingly, our calculation shows that only 0.03% and 0.02% of the O^{2-} ions can be taken out of the cathode material when 50% and 20% oxygen gas partial pressures are used, respectively. The hard step of

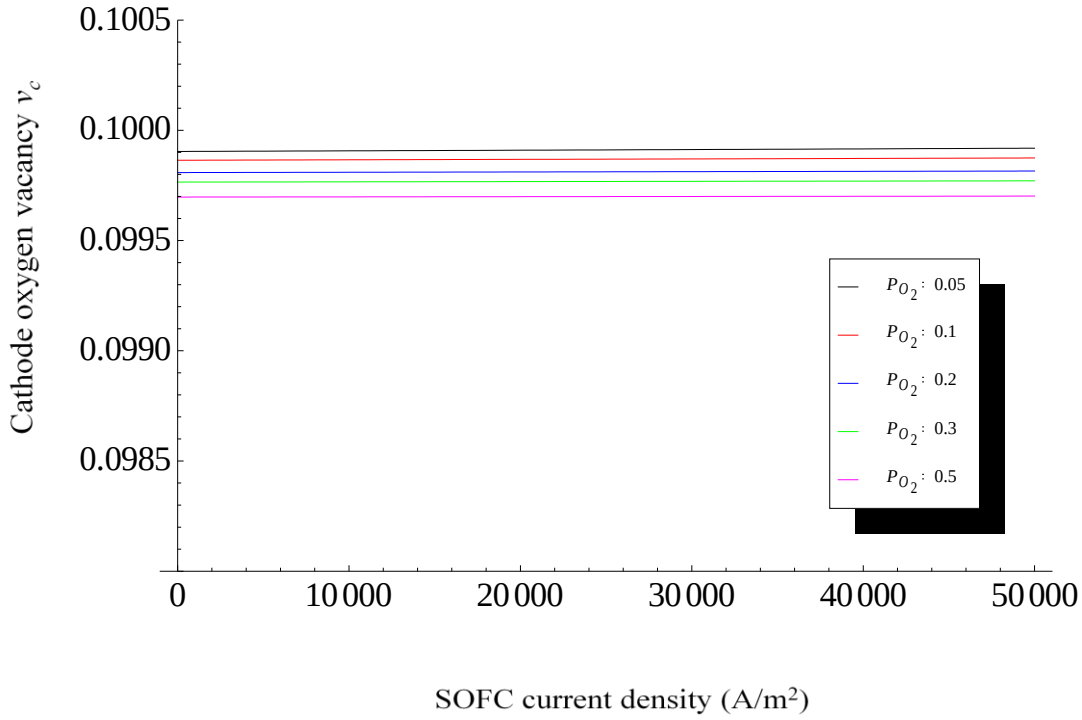

Figure 5.5.1 Calculated oxygen vacancy fraction in cathode *vs*. cell current density output for different oxygen partial pressures in oxidant gas.

taking out oxygen ions from the cathode suggests the performance of H-SOFC is limited by the cathode material. The porosity of thin cathode can't be measured directly and is assumed to be the same as anode, 44%. Putting these factors together, we get

$$c_0 = 119.78 \text{ A/cm}^2 . \tag{5.5.6}$$

We use the same parameters for *c(i)* and know the lattice constant for LSM is 0.392 nm. We obtain

$$d_0 = \frac{3^{2/3}(2q)\upsilon(1-\phi)(0.1-v_c)^2}{a_c^2} = 187.26 \text{ A/cm}^2 . \tag{5.5.7}$$

To calculate forward attempt current density *f* for the reaction at the electrolyte-cathode interface, we assume the fraction f_c of O^{2-} sites on the TPB is equal to f_a. The lattice constant of LSM is 0.392 nm, so

$$f_0 = \frac{3^{2/3} a_{ele}^6 n_{H,ele}^2 (1-v_{ele})^2 (0.1-v_c) f_c q\upsilon}{9a_c^2} = 3.689 \text{ A/cm}^2 . \qquad (5.5.8)$$

The steam concentration at the cathode-electrolyte interface n_{c,H_2O} is a function of operating current density because of the generation of exhaust gas from running the cell. We further assume steam concentration in the air that we used to run the cell is 2% so that the fraction of steam in the air at the anode-electrolyte interface is $0.02 + i/(qn_{total})$, where n_{total} is the total gas concentration at the anode-electrolyte interface. From our calculation, as an example, the steam partial pressure at the cathode-electrolyte interface is 3.475% when running the cell at current density 3 A/cm^2. Therefore, we get

$$h_0 = \frac{1}{2} n_{c,H_2O} \left(\frac{kT}{m_{H_2O}}\right)^{1/2} \left[1 - \left(\frac{a_{ele}^3 n_{H,ele}}{3}\right)\right]^2 (1-v_{ele})^2 v_c f_c q = 3.539 \text{ A/cm}^2 . \qquad (5.5.9)$$

According to Eq. (5.3.4), we note that the current density *i* is limited to a finite range, in which

$$-b \le i \le a \text{ (for anode limitation) and}$$

$$-h \le i \le f \text{ (for cathode limitation)}$$

regardless of the value of *V* as it runs from negative to positive infinity. Our calculation shows the output of H-SOFC is limited by the attempt current density *f,* which refers to the reaction $2H^+ + O^{2-} \rightarrow H_2O$, accordingly 3.689 A/cm^2 for the maximum current density. However, this value can be increased by increasing f_c such as by introducing a cathode interlayer. Similarly, high steam concentration n_{c,H_2O} and high f_c at cathode-electrolyte interface benefit the H_2 production for SOEC mode.

For the reaction $H_2 + 1/2O_2 \rightarrow H_2O$, the Gibbs free energy for reactants and product at standard-state conditions (25 ^{o}C, 1 atm) can be found from thermodynamics properties table in reference [69], which gives

$$\begin{aligned} &\bar{g}_{H_2O} = -306.69 \text{ kJ/mole}, \\ &\bar{g}_{H_2} = -38.96 \text{ kJ/mole}, \text{ and} \\ &\bar{g}_{O_2} = -61.12 \text{ kJ/mole}. \end{aligned} \tag{5.5.10}$$

The equation of Gibbs free energy of formation is $\Delta\bar{g}_f = \bar{g}_{prod} - \bar{g}_{react}$. Then, the Gibbs free energy of formation for the reaction $H_2 + 1/2O_2 \rightarrow H_2O$ can be calculated as

$$\Delta\bar{g}_f = \bar{g}_{H_2O} - \bar{g}_{H_2} - \tfrac{1}{2}\bar{g}_{O_2} = (-306.69) - (-38.96 + 0.5 \times (-61.12)) = -237.13 \text{ kJ/mole}. \tag{5.5.11}$$

The definition of Gibbs free energy is

$$dG = dU - SdT - TdS + Vdp + pdV, \tag{5.5.12}$$

and, the internal energy is

$$dU = TdS - pdV - dW. \tag{5.5.13}$$

In a constant temperature and pressure process, we use Eqs. (5.5.12) and (5.5.13) to obtain

$$dG = -dW = \Delta\bar{g}_f . \tag{5.5.14}$$

Then, the voltage generated by a hydrogen-oxygen reaction under standard-state conditions can be calculated as

$$E^0 = \frac{-\Delta\bar{g}_f}{zF} = \frac{237.13\,(\text{kJ/mole})}{2\times 96485} = 1.228\,(\text{Volt}), \tag{5.5.15}$$

where z is the number of electrons produced per reaction, two electrons for the reaction $H_2 + \frac{1}{2}O_2 \rightarrow H_2O$, and F is Faraday constant. The temperature dependent voltage generated by a hydrogen-oxygen reaction can be found on p. 43 of reference [69] and the value at 700 ^{o}C can be calculated as

$$E_{700C} = E^0 + \frac{\Delta\hat{s}}{zF}(T - T_0) = 1.228 - (2.304\times 10^{-4}\ \text{V/K})(973 - 298) = 1.073\,(\text{Volt}), \tag{5.5.16}$$

where $\Delta\hat{s}$ is a temperature independent mole entropy for changing T by 1 K, $-44.43\,\text{J/(mol}\cdot\text{K)}$ for the hydrogen-oxygen reaction. Eq. (5.5.16) gives the emf U/q at 700 ^{o}C. Therefore, we can calculate the open-circuit voltage by using Eq. (5.4.11) as

$$V_0 = U/q - (kT/q)\ln[\frac{b_0 h_0\sqrt{d_0}}{a_0 f_0\sqrt{c_0}}]$$

$$= 1.073 - 0.042\ln[21038.8/70715.9] = 1.022\ (\text{Volt}). \tag{5.5.17}$$

Figure 5.5.2 (a) compares the results from experiment and model for H_2 partial pressure dependent tests at 700 ^oC. We see the excellent agreement between the experimental and modeling data for different H_2 partial pressures. However, for $p_{H_2} = 0.2$, our model predicts that concentration polarization limits the current density to 1.1 A/cm^2 while the experimental data show that a much higher current density was achieved. Our model does predict the behavior of the first half of the I-V curve but not the other half. This makes us think there might be a mechanism other than gas diffusion, such as surface diffusion of H_2 along the Ni surface in the anode, that helps the transport of H_2 to the reaction area when the H_2 concentration at the anode-electrolyte interface gets very low. This other mechanism may also account for the "tail" effect that we found

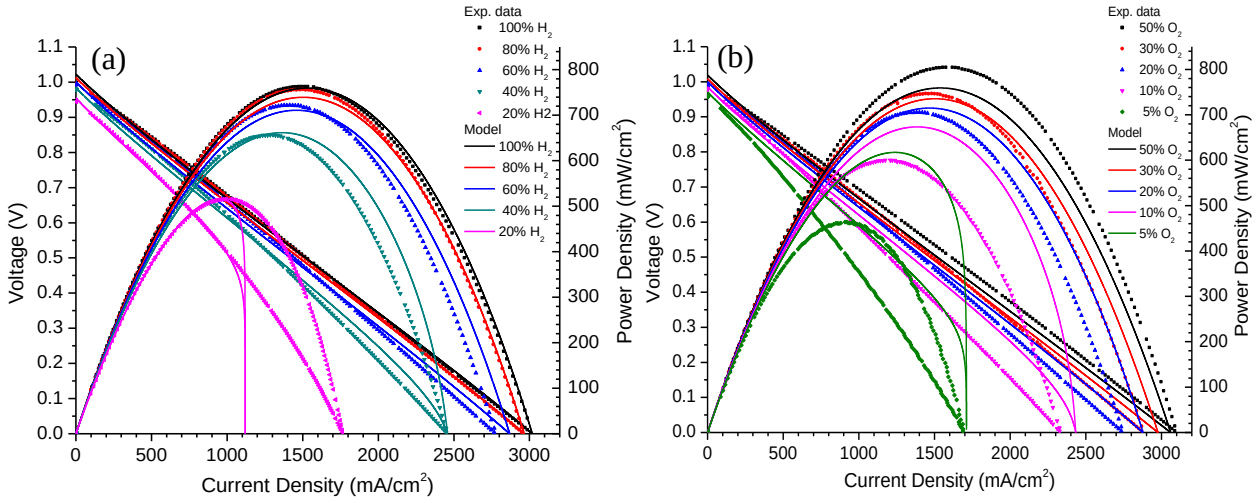

Figure 5.5.2 Comparison of experimental results for *V(i)* with our model predictions for different (a) H_2 partial pressures of anode inflow (using air for cathode) and (b) O_2 partial pressures at cathode inflow (using 60% H_2/40% N_2 for anode)

in Chapter 3. The comparison of experimental results and model prediction for different O_2 partial pressures at the cathode are shown in Fig. 5.5.2 (b), using 60% H_2 /40% N_2 as fuel on the anode. The agreement between modeling and experimental data is not as good as in Fig. 5.5.2 (a). This is possibly because the information for the cathode, such as porosity, tortuosity, and fraction of O^{2-} sites on the TPB, is not available. However, the predictions for high O_2 partial pressures are still good.

Here, we want to emphasis that we use one set of parameters to predict effects of changing both H_2 and O_2 partial pressures. All the parameters that we used are listed in Table 5.5.1. This is different from the works done by other groups such as Ni *et al.* and Zhu *et al.* in that they use a set of parameters to fit only one I-V curve [62-64,70]. Therefore, our model should be a tool to arrive closer to the true physical pictures of H-SOFC operation.

5.6 Model Predictions for the Effects of Operating Parameters on H-SOFC Performance

By using this validated model, the effects from different parameters can be studied. For the purpose of clearly seeing the effects, we lower the ohmic polarization V_{ohm} from0.275i V to 0.2i V for all the study cases (except for studying the effect from changing of V_{ohm}) and keep all the other parameters the same as those we used to fit to the experimental data. All the data presented here are for using 100% H_2 as fuel gas and air as oxidative gas, except 40% H_2/60% N_2 fuel gas is used to see the

Table 5.5.1 Values of input arameters used in the fitting model.

Constant para.	**Number**	**Meaning**
k	1.38×10^{-23}	Boltzmann constant, *j/K*
T	973	SOFC tested temperature, *K*
$P_{Bozeman}$	8.543×10^{4}	Atmosphere in Bozeman, N/m^2
P_1	1.015×10^{5}	1 atmosphere, N/m^2
q	3.2×10^{-19}	Transferred charge per reaction, *C*
m_{H_2}	3.32×10^{-27}	H_2 molecular weight, *kg*
m_{H_2O}	2.988×10^{-26}	H_2O molecular weight, *kg*
m_{O_2}	5.312×10^{-26}	O_2 molecular weight, *kg*
υ	1×10^{13}	Attempt frequency, *Hz*

Meas. para.	**Number**	**Meaning**
a_c	3.92×10^{-10}	LSM lattice constant, *m*
a_{ele}	4.445×10^{-10}	BCY20 lattice constant, *m*
w	1.15×10^{-3}	SOFC anode thickness, *m*
φ	0.44	SOFC anode porosity
s	5.7×10^{-5}	Effective cathode area, m^2
inflow	200×10^{-6}	Input gas flow, m^3

Cal. para.	**Number**	**Meaning**
D_{K,H_2}	15.19×10^{-4}	H_2 Knudsen diffusion coefficient, m^2/sec
D_{K,N_2}	4.06×10^{-4}	N_2 Knudsen diffusion coefficient, m^2/sec
D_{K,H_2O}	5.06×10^{-4}	H_2O Knudsen diffusion coefficient, m^2/sec
D_{H_2,H_2O}	6.65×10^{-4}	H_2/ H_2O binary diffusion coefficient, m^2/sec
D_{H_2,N_2}	5.35×10^{-4}	H_2/N_2 binary diffusion coefficient, m^2/sec
D_{N_2,H_2O}	1.87×10^{-4}	N_2/ H_2O binary diffusion coefficient, m^2/sec
v_{ele}	0.04	Oxygen vacancy in BCY20 electrolyte

Assu. para.	**Number**	**Meaning**
$n_{H,ele}$	0.12	Proton concentration per BCY20 formula
n_{a,H_2O}	3%	Input steam concentration at anode-electrolyte interface
n_{c,H_2O}	2%	Input steam concentration at cathode-electrolyte interface

Adjustable para.	Number	Meaning
τ	2.4	Anode tortuosity
$U_{c,O}$	3.0×10^{-21}	Energy needed for dissociating O_2 molecule into $2O^{2-}$ ion on cathode material, *joule*
V_{ohm}	0.275i	SOFC ohmic polarization, *V*
f_a	2.822×10^{-3}	Fraction of oxygen sites at TPB

effect of changing tortuosity. Figure 5.6.1 (a) shows the effect of increasing f_a, the fraction of oxygen sites at the TPB. The current density is primarily limited by attempt current density *f* when f_a is lower than 2.82×10^{-3} and limited by ohmic polarization when f_a is higher than that value. More precisely, we should say the current density is limited by the fraction of oxygen sites at the cathode TPB, f_c, which provides the area for the reaction $2H^+ + O^{2-} \rightarrow H_2O$. To alleviate this problem, introducing a cathode interlayer, which is made by mixing 50/50 electrolyte/cathode material, can increase the value of f_c. Another possibility like finding a material that conducts protons, oxygen ions and electrons would be even more favorable. Fig. 5.6.1 (a) also shows that if we use $f_a = 2.822\times10^{-4}$ for our model, the current density is limited to 0.37 A/cm^2, which is much lower than what we have in the experimental data. Thus, the increasing of f_a by taking into account the 3-dimensional network gives us a result closer to the experimental data.

The effect of increasing proton concentration in the electrolyte is shown in Fig. 5.6.1 (b). The results from modeling show that there are not enough protons for the reaction

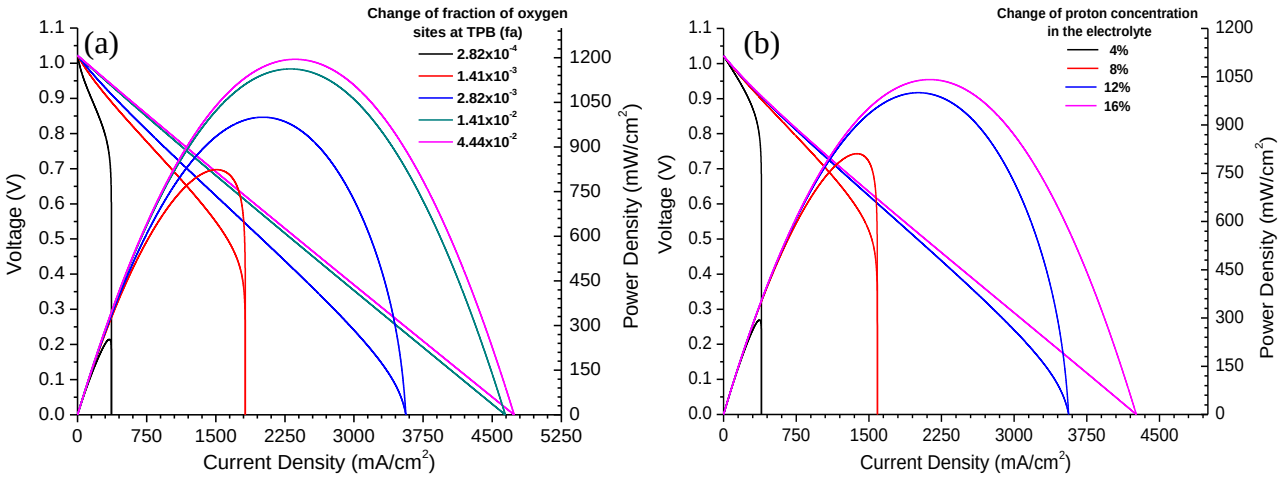

Figure 5.6.1 the effects of changing (a) the fraction of oxygen sites on TPB, f_a and (b) the proton concentration in the electrolyte, $n_{H,ele}$.

$2H^+ + O^{2-} \rightarrow H_2O$ at the cathode TPB when proton concentration is low. It is obvious that the more protons in the electrolyte the better performance of the SOFC. However,the proton concentration in the electrolyte can not be increased infinitely, usually < 20% because of the limitation of dopant that can be introduced into the material.

The parameters for modeling of the effect of lowering ohmic polarization of H-SOFC are different from the others. We keep all the parameters the same as fitting to our experimental data and only change the ohmic polarization. The lowering of ohmic polarization can also be interpreted as increasing proton conductivity of the electrolyte material. The saturation current density increases with decreasing ohmic polarization and limits to 3.63 A/cm^2 when ohmic polarization is lower than 0.2*i*, Fig 5.6.2 (a). This limitation of current density is coming from the shortage of cathode-electrolyte TPB, i.e.

f_c, which provides insufficient reaction area for the reaction $2H^+ + O^{2-} \rightarrow H_2O$ to occur. Reducing ohmic polarization can be done in three ways; one is finding a new material with high proton conductivity, another is increasing operating temperature and the third is decreasing the thickness of electrolyte. It is much easier to increase proton conductivity by increasing operating temperature than to find a new material or to reduce the thickness of electrolyte. We used ~30 μm for the tested cell and it might be hard to make it below 10 μm by conventional methods. However, increasing operating temperature over a certain level introduces high electronic conductivity of the electrolyte material, especially with Ce content material, which leads to lower energy efficiency. It also requires much more expensive material for the other parts of the SOFC system such as interconnect and thermal insulation.

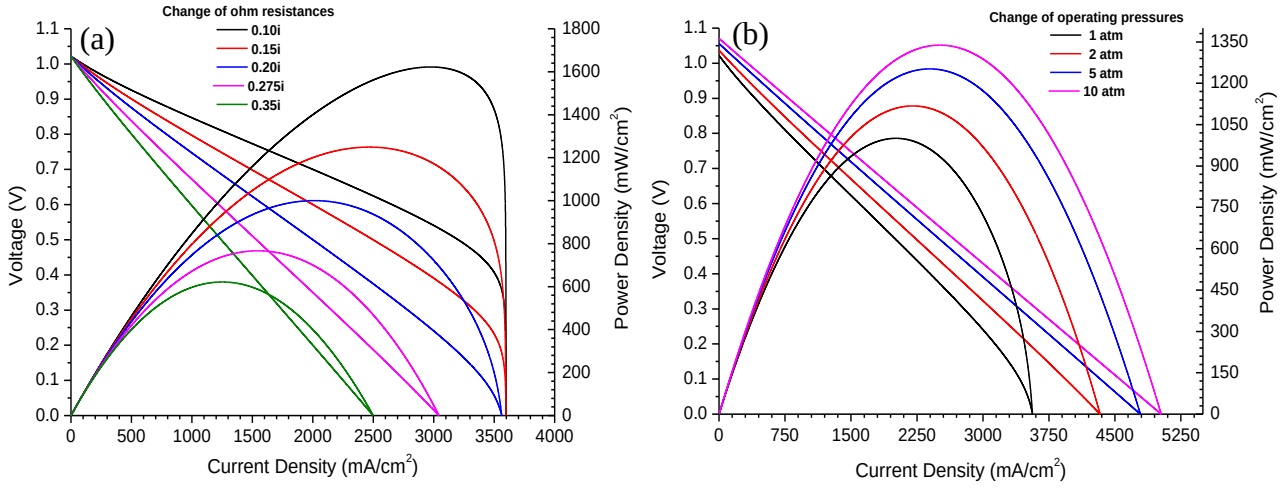

Figure 5.6.2 the effects of changing (a) ohmic polarization of the SOFC and (b) operating pressure.

The influence of SOFC operating pressure is shown in Fig. 5.6.2 (b). The increasing of power density comes from the increase of available O^{2-} ion concentration in the cathode material, thereby increasing the attempt current density *f* of the cell. The peak power density increases 12% when operating pressure doubles. Then, it increases 25% and 34% when operating pressure increases to 5 and 10 atm, respectively. The effect from increasing operating pressure to get higher power output becomes lower when the pressure gets higher. This result suggests that the benefit from increasing operating pressure might not always be positive when we consider the energy it takes to increase the operating pressure.

For the effect of changing tortuosity, we use 40% H_2/60% N_2 fuel gas for the study so that we can see the saturation current density increase with decreasing tortuosity,

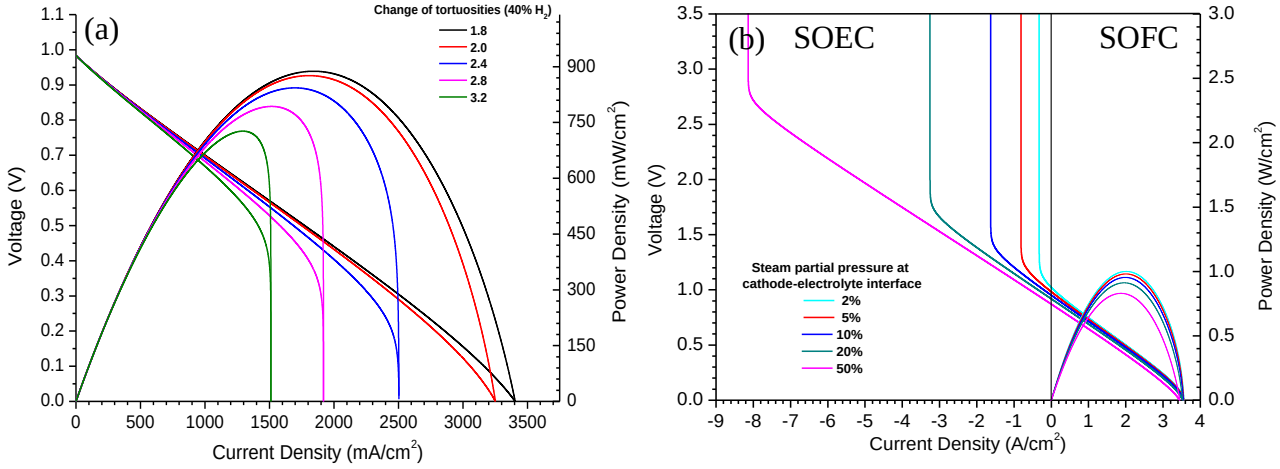

Figure 5.6.3 the effects of changing (a) tortuosity of supporting anode and (b) steam concentration at cathode-electrolyte interface for both SOFC and SOEC modes.

Fig. 5.6.3 (a). This is because of the easier transport of fuel gas to the TPB and exhaust gas out of the cathode when tortuosity is smaller, i.e. diffusion path is shorter. For the tortuosity smaller than 1.8, the saturation current density is limited by attempt current *f*, i.e. shortness of TPB. Therefore, if we use tortuosity 1.8 and ohmic polarization 0.275*i* to fit to our experimental data, we only see a straight I-V curve, i.e. limited by ohmic polarization, instead of a curved I-V curve, having some effect from concentration polarization, for the tested cell using 40% H_2/ 60% N_2 as fuel gas.

Fig. 5.6.3 (b) shows the effect of steam concentration at the cathode-electrolyte interface for both SOFC and SOEC modes. For SOFC mode, we can clearly see that the removal of steam at the cathode, by increasing flowing rate of air, can increase open-circuit voltage and power output. In SOEC mode, the cut-off in current density is limited by attempt current density *h*, which means even a large applied negative voltage could not drive the current density past this limitation. This is the current density corresponding to all steam molecules impinging on the TPB at the cathode-electrolyte interface ionizing into two H^+ and one O^{2-} successfully.

5.7 Conclusions

An electrochemical model was developed to study the I-V performance of H-SOFC. The expression of $V(i)$ that we derive for H-SOFC and the expression derived by Schmidt for O-SOFC are quite similar [71], except the v_c in the H-SOFC expression needs to be solved by another equation, i.e. Eq (5.4.7)

$$H-SOFC \quad V=(U_a+U_{cw})/q-(kT/q)\ln[(b+i)(h'v_c+i)/(a-i)(f'(0.1-v_c)-i)]-V_{ohm},$$

and

$$O-SOFC \quad V=U/q-(kT/q)\ln[(b+i)(d+i)^{1/2}/(a-i)(c-i)^{1/2}].$$

The form that we derived for the $V(i)$ expression is different from the expressions that can be seen in the literature [62-64, 66, 70-74]. Usually, the Nernst equation is used for deriving the contribution of concentration polarization where typically the partial pressure will appear. These partial pressure terms are related to the gas concentration terms in our expression for attempt current densities by the ideal gas law. The factors that are not related to gas concentrations are omitted in the usual literature expressions, but their effect shows up in a combined entropy and enthalpy term when proceeding to the logarithmic term. In our expression, *U/q* is the total enthalpy release by the reaction $H_2+\frac{1}{2}O_2\rightarrow H_2O$. The released enthalpy is independent of cell construction and operating parameters, whereas the entropy depends on such parameters. By taking the factors unrelated to gas concentration into account, we include entropy in the prediction of $V(i)$. Therefore, the good agreement between the experimental data and model prediction provides evidence that our model is close to the H-SOFC physical picture.

The parametric analyses were also performed to identify the key sources for improving H-SOFC performance. The reducing of ohmic polarization is found to be the major possible improvement of the cell. Other than ohmic loss, the performance of H-SOFC is mostly restricted by the attempt current density *f*, which means the cathode material of the H-SOFC controls the performance of the whole cell. The expression of *f*

suggests that increasing of TPB at the cathode-electrolyte interface, having higher proton concentration in the electrolyte and having more available O^{2-} ions in the cathode improve the performance of H-SOFC. Therefore, using a cathode interlayer, looking for a cathode material, which conducts protons, oxygen ions and electrons and having a material with higher oxygen dissociation property are the ways to increase H-SOFC performance.

CHAPTER 6

CONCLUSIONS

6.1 Summary of Results

Single phase $Ba(Zr_{0.8-x}Ce_xY_{0.2})O_{3-\delta}$ ($0 \leq x \leq 0.4$) powders were synthesized by the Glycine-Nitrate Process and Solid State Reaction. The sintering temperature and dwell time of the BZCYs were significantly reduced by introducing LiF sintering additive. We concluded that the liquid phase of LiF, melting point at 847 ^{o}C, helps the diffusion mechanism between BZCY particles and results in the availability of high density BZCY ceramics at much lower temperature. Nuclear reaction studies show there is no lithium and only a small amount of fluorine remaining inside the $Ba(Zr_{0.6}Ce_{0.2}Y_{0.2})O_{3-\delta}$/LiF samples, which indicates the non-concomitant departure of lithium and fluorine. The low concentration of LiF related product in the material suggests that any negative consequence of the impact of using LiF should be trivial. FE-SEM images show the bimodal grain size distributions in all BZCYs/LiF sintered pellets. Conductivity measurements show that the introduction of LiF increases the total conductivity, which is likely the result of LiF causing a slight barium deficiency in the structure.

Electrolyte-supported H-SOFCs using $Ba(Zr_{0.8-x}Ce_xY_{0.2})O_{3-\delta}$ ($0 \leq x \leq 0.4$) and LiF additive were fabricated. The power densities of the cells were relatively low due to the thick electrolyte and the low proton conductivity. Among the tested cathode materials, Pt electrodes had much higher power output, indicating that the polarizations between

ceramic cathodes and electrolytes are much larger than Pt. Compatible cathode should be further developed for improving the H-SOFC performance.

Both $Ba(Zr_{0.6}Ce_{0.2}Y_{0.2})O_{3-\delta}$ and $Ba(Ce_{0.8}Y_{0.2})O_{3-\delta}$ were used for anode-supported H-SOFC. The power densities of $Ba(Zr_{0.6}Ce_{0.2}Y_{0.2})O_{3-\delta}$ anode-supported H-SOFC are limited by ohmic polarization, which is a result of relative low proton conductivity of $Ba(Zr_{0.6}Ce_{0.2}Y_{0.2})O_{3-\delta}$. Although $Ba(Zr_{0.6}Ce_{0.2}Y_{0.2})O_{3-\delta}$ is chemically stable in a CO_2 containing atmosphere, the low proton conductivity makes it unsuitable for commercial use in H-SOFC.

$Ba(Ce_{0.8}Y_{0.2})O_{3-\delta}$ anode-supported H-SOFCs using LSM as cathode show excellent power output. H_2 partial pressure affects the power output dramatically when it is low, while high concentration H_2 gives a saturated power output. When the cells run with low H_2 partial pressure, a mechanism other than gas diffusion causes a "tail" in the observed I-V curves. This mechanism is not clear but can result from H_2 molecules diffusing along the nickel surface to the reaction area.

By changing the thickness of the supporting anode, saturated current density due to concentration polarization can be obtained. Using the dusty-gas model, which includes Stefan-Maxwell equation and Knudsen terms, the calculation gave a tortuosity of our supporting anode of 1.95 ± 0.1. This value is similar to the number which we obtained previously from analyzing the report from Jiang-Virkar [60]. It also agrees with Williford *et al.* that the tortuosity of the supporting anode with porosity higher than 30% should not be as high as 10 to 17 [61]. The pressure changes of different gases were also calculated by knowing the tortuosity of the supporting anode.

An electrochemical model was developed to study the I-V performance of H-SOFC. The excellent agreement between our model and experimental data implies our model should be a tool to arrive closer to the true physical picture of H-SOFC operation. In our derivation for the activation polarization, our expression, Eq (6.3.5), provides a more accurate prediction of physical pictures than the Butler-Volmer equation. The predictions from our expression are valid for both the SOFC and SOEC modes and also provide a replacement for using the Butler-Volmer equation in SOFC modeling.

In the parametric analyses, our model shows that the reduction of ohmic polarization is found to be the major possible means of improvement of the H-SOFC. Other than ohmic loss, the performance of H-SOFC is mostly restricted by the cathode forward attempt current density *f*, which means the cathode material of the H-SOFC limits the performance of the whole cell. The expression for *f* suggests that increasing of TPB at cathode-electrolyte interface, having higher proton concentration in the electrolyte and having a cathode with better catalytic property for dissociating O_2 molecule would improve the performance of H-SOFC.

6.2 Considerations for Future Work

Proton conducting solid oxide fuel cells and hydrogen separation membranes (HSMs) have several related basic science and technical issues. HSMs can be fabricated by mixing protonic and electronic conductors, which only allow hydrogen (protons) molecules to penetrate it, thereby separating other impurities such as CO, CO_2 and hydrocarbons from hydrogen. Based on this idea, we fabricated high density HSMs on

the top of porous support using cermet materials, which are mixtures of nickel and $Ba(Zr_{0.6}Ce_{0.2}Y_{0.2})O_{3-\delta}$, $Ba(Zr_{0.4}Ce_{0.4}Y_{0.2})O_{3-\delta}$ and $Ba(Ce_{0.8}Y_{0.2})O_{3-\delta}$, respectively. Fig. 6.2.1 shows the SEM image of a porous supported HSM made of Ni-$Ba(Zr_{0.6}Ce_{0.2}Y_{0.2})O_{3-\delta}$ cermet. One can easily see the good adhesion of the membrane to the support and the differences between highly dense membrane and porous support.

HSMs were tested at temperatures between 450 ^{o}C and 850 ^{o}C using 4% H_2/96% Ar as feed gas with flow rate 80 sccm through a water bubbler to pick up ~3% water vapor. Sweep gas was high purity N_2 with 100 sccm flow rate. Fig. 6.2.2 (a) shows the gas chromatography (GC) data of $Ba(Zr_{0.4}Ce_{0.4}Y_{0.2})O_{3-\delta}$ SHM at 700 ^{o}C. There was only a hydrogen peak, which shows there was no leak through the sample

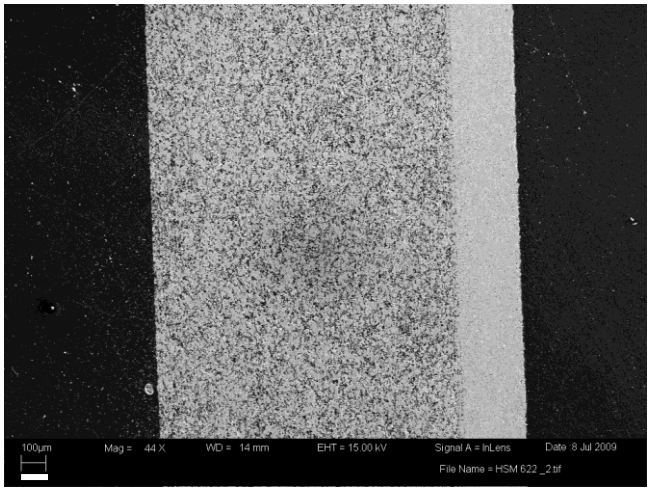

100 μm

Figure 6.2.1 SEM image of porous support hydrogen separation membrane using a mixture of nickel and $Ba(Zr_{0.6}Ce_{0.2}Y_{0.2})O_{3-\delta}$

itself or the sealant. This means that a high density HSM was formed and was able to separate H_2 from the Ar. Fig. 6.2.2 (b) shows the temperature dependent hydrogen permeation flux of an HSM from 450 to 850 ^oC. The flux obviously increases with increasing Ce content in the proton conducting oxide. The permeation flux dropped quickly to the range below GC's detection limit below 450 ^oC.

The demonstration of the idea of HSM was achieved. However, one might be concerned more about the chemical stability of the proton conducting material under the working environment; usually such as hydrocarbon gases, CO, CO_2 and high steam partial pressure can be expected. A long-term test with the different gases mentioned previously should be conducted. Other than chemical stability, the thickness of dense

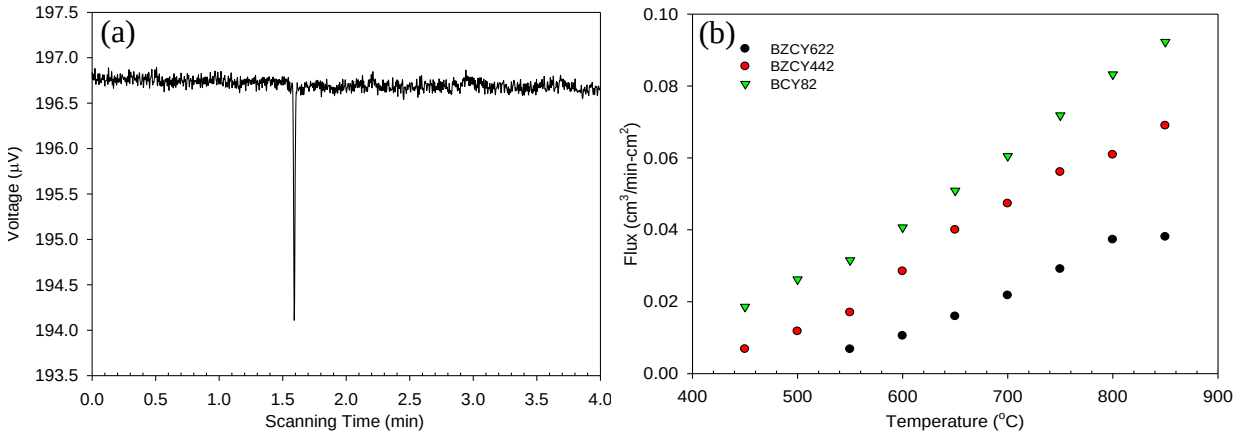

Figure 6.2.2 (a) GC data of Ni- $Ba(Zr_{0.4}Ce_{0.4}Y_{0.2})O_{3-\delta}$ cermet HSM at 700 ^oC and (b) temperature dependent hydrogen permeation flux of Ni-$Ba(Zr_{0.4}Ce_{0.4}Y_{0.2})O_{3-\delta}$, Ni-$Ba(Zr_{0.6}Ce_{0.2}Y_{0.2})O_{3-\delta}$ and Ni- $Ba(Ce_{0.8}Y_{0.2})O_{3-\delta}$ HSMs.

membrane can be further reduced to increase H_2 permeation flux by available conventional methods or new technology.

With the developed promising ceramic and cell fabrication processes, it is possible to obtain proton-electronic mixed conductivity and high chemical stability ceramic within one phase by doping multivalent metals such as Mn, Co, Ti, Mo, Pr, Tb or Bi. The use of single phase ceramic instead of cermet can mitigate the possible cracking or formation of pinholes due to the difference of thermal expansion coefficients over the thermal cycles. Furthermore, the same material can also be used as cathode material for H-SOFC to extend its reaction area. So far, we have synthesized $BaCe_{0.4}Pr_{0.4}Y_{0.2}O_{3-\delta}$ for use as an SOFC cathode and investigated the electrochemical properties of $BaCe_{0.8-x}Tb_xY_{0.15}O_{3-\delta}$ with x from 0.01 to 0.1. Further research on this type of material is worth continuing.

According to our model prediction, reducing ohmic polarization is the major possibility for improving the H-SOFC performance. Looking for other materials with high proton conductivity is then important for the H-SOFC development. It is possible to get higher conductivity material of perovskite structure oxides (A site = Ca, Sr and Ba, and B site=Ti, Zr, Ce and Pr) by doping with lanthanides. Other than finding new material, Y-doped $BaZrO_3$ has been proved to have the highest bulk proton conductivity among the oxide ion conductors [23]. However, the inevitable structure distortions in the grain boundary region enormously reduce the overall proton conductivity. Attacking this problem with some sintering additive like Li_2CO_3 or K_2CO_3 may be able to reduce distortions along the grain boundary [76].

For the modeling of H-SOFC, efforts to obtain information at the cathode side such as tortuosity and porosity, thereby obtaining the oxygen concentration across the cathode, are important to accomplishing this model. When doing the modeling, we assume the O^{2-} vacancies in the cathode are about 10% and calculation shows the available O^{2-} ions for reactions at cathode are about 0.03%. Yasumoto *et al.* showed experimentally that due to a buffer effect, for our x=0.2 Sr concentration in the LSM cathode, the value of δ in the LSM formula $La_{1-x}Sr_xO_{3-\delta}$ is almost independent of x and is within the range 0 ± 0.01 for log[$P(O_2)$Pa] between -5 and +4 [77]. They state that "At the oxygen excess region, $\delta > 0$, there are metal-site defects and the oxide ion lattice is filled with oxide ions." This is not exactly true, because, for instance, if $\delta = 0$, statistical mechanics requires that there be equal and nonzero concentrations of oxygen ion interstitials and vacancies. However, the experimental data show the O^{2-} vacancy concentration in LSM is small, i.e. not as high as 10%. Therefore, a careful experiment for measuring the O^{2-} ion and vacancy concentration in LSM is necessary.

REFERENCES CITED

1. G. Ma, T. Shimura, H. Iwahara, *Solid State Ionics,* 110 (1998) 103.
2. W. Suksamai, I. S. Metcalfe, *Solid State Ionics*, 178 (2007) 627.
3. B. R. Sneha, V. Thangadurai, *J. Solid State Chem*., 180 (2007) 2661.
4. S. V. Bhide, A. V. Virkar, *J. Electrochem. Soc*., 146 (1999) 2038.
5. H. Iwahara. H. Uchida, K Ogki, *J. Electrochem. Soc*., 135 (1988) 529.
6. S. M. Haile, G. Staneff, K. H. Ryu, *J. Mater. Scien*., 36 (2001) 1149.
7. A. Magrez, T. Schober, *Solid State Ionics,* 175 (2004)585.
8. H. G. Bohn, T. Schober, *J. Am. Ceram. Soc*., 84 (2000) 768.
9. T. Schober, H. G. Bohn, *Solid State Ionics*, 127 (2000) 351.
10. K. Nomura, H. Kageyama, *Solid State Ionics*, 178 (2007) 661.
11. C.-S. Tu, R. R. Chien, V. H. Schmidt, S-C. Lee, C.-C. Huang, C-L. Tsai, *J. Appl. Phys*. 105 (2009) 103504.
12. K. Katahira, Y. Kohchi, T. Shimura, H. Iwahara, *Solid State Ionics*, 138 (2000) 91.
13. J. M. Haussonne, G. Desgardin, *Dielectric ceramics*, (1992) 155.
14. T. Takahashi, H. Iwahara, *Rev. Chim. Miner., t17,* (1980) 243.
15. H. Iwahara, T. Esaka, H. Uchida, N. Maeda, *Solid State Ionics,* 3/4 (1981) 359.
16. H. Iwahara, T. Yajima, T. Hibino, H. Ushida. *J. Electrochem. Soc*., 140 (1993) 1687.
17. M.J. Scholten, J. Schoonman, J.C. van Miltenburg, H.A.J. Oonk, *Solid State Ionics* 61 (1993) 83.
18. S. Gopalan, A.V. Virkar, *J. Electrochem. Soc.* 140 (1993) 1060.

19. N. Taniguchi, T. Gamo, *Denki Kagaku* 62 (1994) 326.

20. N. Bonanos, K.S. Knight, B. Ellis, *Solid State Ionics*, 79 (1995) 161.

21. C.W. Tanner, A.V. Virkar, *J. Electrochem. Soc.*, 143 (1996) 1386.

22. T. Yajima, H. Suzuki, T. Yogo, H. Iwahara, Solid State Ionics 51 (1992) 101.

23. K.D. Kreuer, *Annu. Rev. Mater. Res.*, 33 (2003) 333.

24. H. Iwahara, *Solid State Ionics* 28–30 (1988) 573.

25. R. Glo¨ckner, M.S. Islam, T. Norby, *Solid State Ionics*, 122 (1999) 145.

26. M.S. Islam, *J. Mater. Chem*., 10 (2000) 1027.

27. R. A. Davies, M. S. Islam, J. D. Gale, *Solid State Ionics*, 126 (1999) 323.

28. K. D. Kreuer, E. Schonherr, J. Maier, *Solid State Ionics*, 70/71 (1994) 278.

29. R. Hempelmann, M. Soetramo, O. Hartmann, R. Wappling., *Solid State Ionics*,107 (1998)269.

30. B Viswanathan, M. Aulice Scibioh, *Fuel Cells: Principles and Application*, Universities Press 2007

31. J. Larminie, A. Dicks, *Fuel Cell Systems Explained*, 2nd Edition, Wiley 2003.

32. E. Subhash, C. Singhal, K. Kendall, *High-temperature Solid Oxide Fuel Cells: Fundamentals, Design and Applications,* Elsevier, 2003.

33. H.-H. Mobius, *J. Solid State Electrochem*. 1 (1997) 2.

34. SPS Badwal, K. Foger, *Mater. Forum*, 21 (1997) 183.

35. SPS Badwal, F. T. Ciacchi, V. Zelizko, *Ionics*, 4 (1998) 25.

36. A. Demin, P. Tsiakaras, *Int. J. Hydrogen Energy,* 26 (2001)1103.

37. S. Assabumrungrat, W. Sangtongkitcharoen, N. Laosiripojana,A. Arpornwichanop, S. Charojrochkul, P. Praserthdam, *J. Power Sources*, 148 (2005) 18.

38. W. Jamsak, S. Assabumrungrat, P. L. Douglas, N. Laosiripojana, S. Charojrochkul, *Chem. Eng. J.*, 119 (2005) 11.

39. A. K. Demin, P. E. Tsiakaras, V. A. Sobyanin, S. Y. Hramova, *Solid State Ionics*, 152–153 (2002) 555.

40. T. Hibino, A. Hashimoto, M. Suzuki, M. Sano, *J. Electrochem. Soc*. 149 (2002) A1503.

41. K. Yamahara, C. P. Jacobson, S. J. Visco, X.-F. Zhang, L. C. De Jonghe, *Solid State Ionics*176 (2005) 269.

42. B. Lin, Y. Dong, R. Yan, S. Zhang, M. Hu, Y. Zhou, G. Meng, *J. Power Sources*, 186 (2009) 446.

43. K. Katahira, Y. Kohchi, T. Shimura, H. Iwahara, *Solid State Ionics*, 138 (2000) 91.

44. A. D'Epifanio, E. Fabbri, E. Di Bartolomeo, S. Licoccia, E. Traversa, *Fuel Cell 08*, No. 1 (2008) 69.

45. S. Tao, T. S. Irvine, *Adv. Mater*. 18 (2006) 1581.

46. P. Babilo, S. M. Haile, *J. Am. Ceram. Soc*. 88 (2005) 2362

47. M. Pollet, S. Marine, *J. Europ. Ceram. Soc*. 23 (2003) 1925.

48. J. M. Haussonne, G. Desgardin, *Dielectric ceramics*, (1992) 155.

49. L.-H. Cao, X. Y. Yao, Z. Xu, Z-R Li, *Integrated Ferroelectrics*, 74 (2005) 13.

50. A. A. Ferreira, J. A. Labrincha, J. R. Frade, *Solid State Ionics*, 77 (1995) 210.

51. L. Yang, C. Zuo, S. Wang, Z. Cheng, M. Liu, *Adv. Mater*, 20 (2008) 3280.

52. N. Bonanos, K. S. Knight, B. Ellis, *Solid State Ionics*, 79 (1995) 161.

53. S. Gopalan, A. V. Virkar, *J. Electrochem. Soc.*, 140 (1993) 1060.

54. U. Balachandran, *Proton-Conducting Membranes*; Annual Report for FY2001; Argonne National Laboratory: Argonne, IL, 2001.

55. M. R. Pillai, Y. Jiang, N. Mansourian, I. Kim, D. M. Bierschenk, H. Zhu, R. J. Kee, S. A. Barnett, *Electrochemical and Solid-state Letters*, 11 (2008) B174.

56. J. W. Kim, A. V. Virkar, K. Z. Fung, K. Mehta, S. C. Singhal, *J. Electrochem. Soc.,* 146 (1999) 69.

57. P. Costamagna, K. Honegger, *J. Electrochem. Soc.*, 145 (1998) 3995.

58. E. L. Cussler, *Diffusion-Mass Transfer in Fluid Systems*, Cambridge University Press, Cambridge, MA (1984)

59. Y. Jiang, A. V. Virkar, *J. Electrochem. Soc.*, 150 (2003) A942.

60. V. H. Schmidt, C.-L. Tsai, *J. Power Sources* 180 (2008) 253.

61. R. E. Williford, L. A. Chick, G. D. Maupin, S. P. Simmer, J. W. Stevenson, *J. Electrochem. Soc.*, 150 (2003) A1067.

62. M. Ni, M. K. H. Leung, D. Y. C. Leung, *Fuel Cell* 07, No. 4 (2007) 269.

63. M. Ni, M. K. H. Leung, D. Y. C. Leung, *J. Power Sources*, 177 (2008) 369.

64. M. Ni, M. K. H. Leung, D. Y. C. Leung, *Int. J.Energy Res.*, 33 (2009) 943.

65. V. H. Schmidt, private communication.

66. M. Ni, M. K. H. Leung, D. Y. C. Leung, *Energy Conversion and Mnagement,* 48 (2007) 1525.

67. C. Y. Jones, J. Wu, L. Li, S. M. Haile, *J. Appl. Phys*., 97 (2005) 114908.

68. L. S. Marks, *Mechanical Engineers' Handbook*, McGraw-Hill, New York (1941), p. 107.

69. R. O'Hayre, S-W Cha, W. Colella, F. B. Prinz, *Fuel Cell Fundamentals*, Wiley, New York (2006).

70. H. Zhu, R. Kee, *J. Power Sources*, 117 (2003) 61.

71. V.H. Schmidt, *Design of Electrode Structures*, ECS Transactions, vol. 6, issue 21, (2008) pp. 11-24.

72. A. K. Demin, P. E. Tsiakaras, V. A. Sobyanin, S. Y. Hramova, *Solid State Ionics*, 152-153 (2002) 555.

73. S. Assabumrungrat, W. Sangtongkitcharoen, N. Laosiripojana, A. Arpornwichanop, S. Charojrochkul, P. Praserthdam, *J. Power Sources*, 148 (2005) 18.

74. A. Demin, P Tsiakaras, *International Journal of Hydrogen Energy*, 26 (2001) 1103.

75. J. R. Wilson, M. Gameiro, K. Mischaikow, W. Kalies, P. W. Voorhees, S. A. Barnett, *Microsc. Microanal*. 15 (2009) 71.

76. T. Schober, *Electrochemical and Solid-State Letters*, 8 (4) (2005) A199.

77. K. Yasumoto, N. Mori, J. Mizusaki, H. Tagawa, M. Dokiya, *J. Electrochem. Soc.*, 148 (1) (2001) A105.

78. K. D. Kreuer, *Solid State Ionics*, 97 (1997) 1.